Strojniški vestnik
Journal of Mechanical Engineering

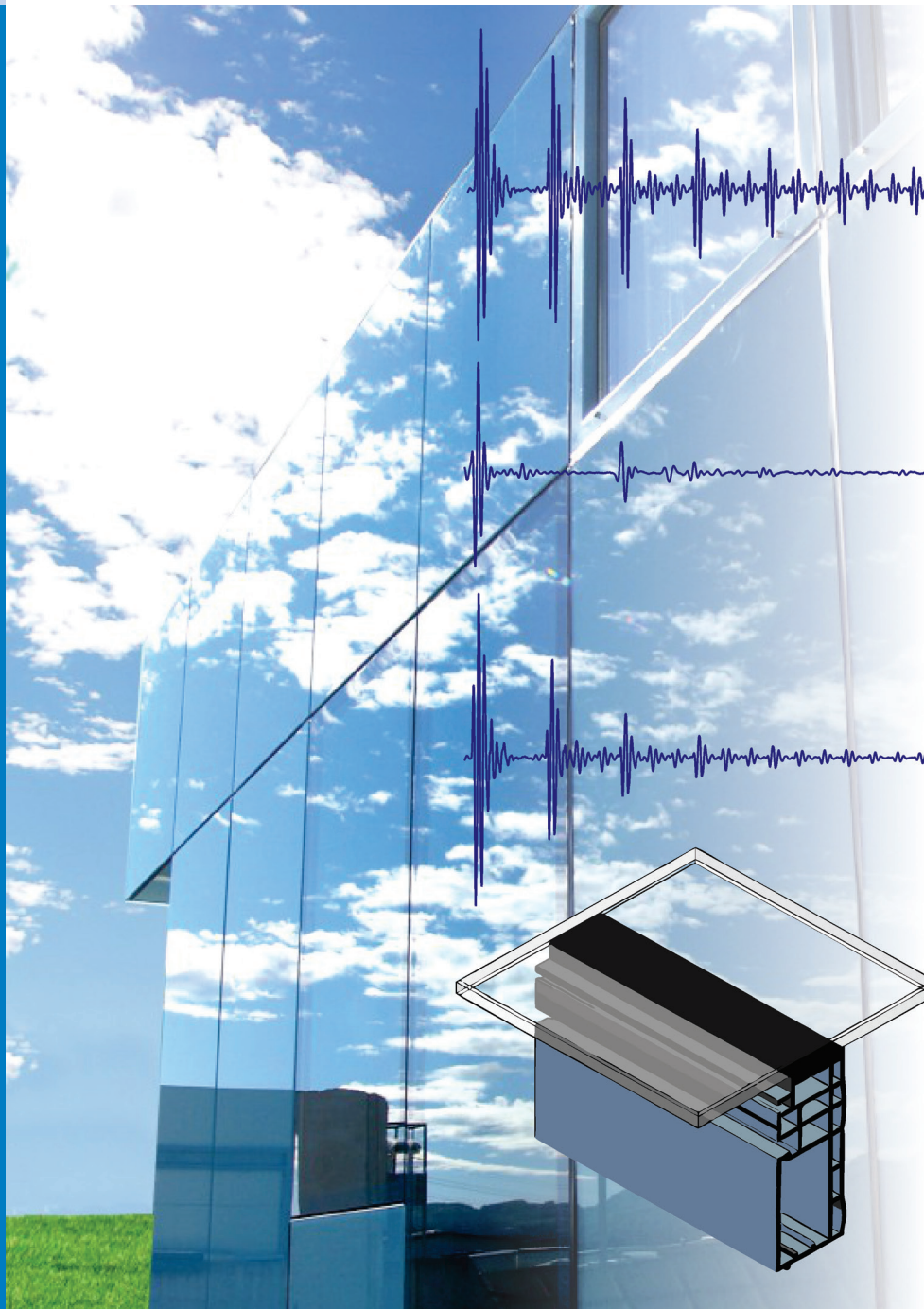

no. 3
year 2016
volume 62

Strojniški vestnik – Journal of Mechanical Engineering (SV-JME)

Aim and Scope
The international journal publishes original and (mini)review articles covering the concepts of materials science, mechanics, kinematics, thermodynamics, energy and environment, mechatronics and robotics, fluid mechanics, tribology, cybernetics, industrial engineering and structural analysis.
The journal follows new trends and progress proven practice in the mechanical engineering and also in the closely related sciences as are electrical, civil and process engineering, medicine, microbiology, ecology, agriculture, transport systems, aviation, and others, thus creating a unique forum for interdisciplinary or multidisciplinary dialogue.
The international conferences selected papers are welcome for publishing as a special issue of SV-JME with invited co-editor(s).

Editor in Chief
Vincenc Butala
University of Ljubljana, Faculty of Mechanical Engineering, Slovenia

Technical Editor
Pika Škraba
University of Ljubljana, Faculty of Mechanical Engineering, Slovenia

Founding Editor
Bojan Kraut
University of Ljubljana, Faculty of Mechanical Engineering, Slovenia

Editorial Office
University of Ljubljana, Faculty of Mechanical Engineering
SV-JME, Aškerčeva 6, SI-1000 Ljubljana, Slovenia
Phone: 386 (0)1 4771 137
Fax: 386 (0)1 2518 567
info@sv-jme.eu, http://www.sv-jme.eu

Print: Grafex, d.o.o., printed in 310 copies

Founders and Publishers
University of Ljubljana, Faculty of Mechanical Engineering, Slovenia
University of Maribor, Faculty of Mechanical Engineering, Slovenia
Association of Mechanical Engineers of Slovenia
Chamber of Commerce and Industry of Slovenia, Metal Processing Industry Association

President of Publishing Council
Branko Širok
University of Ljubljana, Faculty of Mechanical Engineering, Slovenia

Vice-President of Publishing Council
Jože Balič
University of Maribor, Faculty of Mechanical Engineering, Slovenia

Cover: The cover image shows the unique Qbiss Air glass façade system. The façade has a number of adhesively bonded joints, which consist of hardened glass, polysulfide or silicone adhesive and a polymer profile. Adhesive bond quality was evaluated using the non-destructive pulse-echo ultrasonic technique.

Image Courtesy:

Trimo, d.d., Slovenia
www.trimo.si, www.qbiss.eu

Bor Mojškerc, University of Ljubljana, Faculty of Mechanical Engineering, Slovenia

ISSN 0039-2480

International Editorial Board
Kamil Arslan, Karabuk University, Turkey
Hafiz Muhammad Ali, University of Engineering and Technology, Pakistan
Josep M. Bergada, Politechnical University of Catalonia, Spain
Anton Bergant, Litostroj Power, Slovenia
Miha Boltežar, UL, Faculty of Mechanical Engineering, Slovenia
Franci Čuš, UM, Faculty of Mechanical Engineering, Slovenia
Anselmo Eduardo Diniz, State University of Campinas, Brazil
Igor Emri, UL, Faculty of Mechanical Engineering, Slovenia
Imre Felde, Obuda University, Faculty of Informatics, Hungary
Janez Grum, UL, Faculty of Mechanical Engineering, Slovenia
Imre Horvath, Delft University of Technology, The Netherlands
Aleš Hribernik, UM, Faculty of Mechanical Engineering, Slovenia
Soichi Ibaraki, Kyoto University, Department of Micro Eng., Japan
Julius Kaplunov, Brunel University, West London, UK
Iyas Khader, Fraunhofer Institute for Mechanics of Materials, Germany
Jernej Klemenc, UL, Faculty of Mechanical Engineering, Slovenia
Milan Kljajin, J.J. Strossmayer University of Osijek, Croatia
Peter Krajnik, Chalmers University of Technology, Sweden
Janez Kušar, UL, Faculty of Mechanical Engineering, Slovenia
Gorazd Lojen, UM, Faculty of Mechanical Engineering, Slovenia
Thomas Lübben, University of Bremen, Germany
Janez Možina, UL, Faculty of Mechanical Engineering, Slovenia
George K. Nikas, KADMOS Engineering, UK
José L. Ocaña, Technical University of Madrid, Spain
Miroslav Plančak, University of Novi Sad, Serbia
Vladimir Popović, University of Belgrade, Faculty of Mech. Eng., Serbia
Franci Pušavec, UL, Faculty of Mechanical Engineering, Slovenia
Bernd Sauer, University of Kaiserlautern, Germany
Rudolph J. Scavuzzo, University of Akron, USA
Arkady Voloshin, Lehigh University, Bethlehem, USA

General information
Strojniški vestnik – Journal of Mechanical Engineering is published in 11 issues per year (July and August is a double issue).

Institutional prices include print & online access: institutional subscription price and foreign subscription €100,00 (the price of a single issue is €10,00); general public subscription and student subscription €50,00 (the price of a single issue is €5,00). Prices are exclusive of tax. Delivery is included in the price. The recipient is responsible for paying any import duties or taxes. Legal title passes to the customer on dispatch by our distributor.

Single issues from current and recent volumes are available at the current single-issue price. To order the journal, please complete the form on our website. For submissions, subscriptions and all other information please visit: *http://en.sv-jme.eu/.*

You can advertise on the inner and outer side of the back cover of the journal. The authors of the published papers are invited to send photos or pictures with short explanation for cover content.

We would like to thank the reviewers who have taken part in the peer-review process.

© 2015 Strojniški vestnik - Journal of Mechanical Engineering. All rights reserved. SV-JME is indexed / abstracted in: SCI-Expanded, Compendex, Inspec, ProQuest-CSA, SCOPUS, TEMA. The list of the remaining bases, in which SV-JME is indexed, is available on the website.

The journal is subsidized by Slovenian Research Agency.

Strojniški vestnik - Journal of Mechanical Engineering is available on http://www.sv-jme.eu, where you access also to papers' supplements, such as simulations, etc.

Contents

Strojniški vestnik - Journal of Mechanical Engineering
volume 62, (2016), number 3
Ljubljana, March 2016
ISSN 0039-2480

Published monthly

Papers

Strojniški vestnik - Journal of Mechanical Engineering 62(2016)3, 147-153
DOI:10.5545/sv-jme.2015.2988
Original Scientific Paper
Received for review: 2015-08-31
Received revised form: 2015-11-06
Accepted for publication: 2016-01-08
© 2016 Journal of Mechanical Engineering. All rights reserved.

Pulse-Echo Ultrasonic Testing of Adhesively Bonded Joints in Glass Façades

Bor Mojškerc - Tomaž Kek – Janez Grum*
University of Ljubljana, Faculty of Mechanical Engineering, Slovenia

This article presents a pulse-echo ultrasonic method of evaluation of adhesively bonded joints in glass façades by means of the amplitudes of reflected ultrasonic signals. Glass façade specimens consist of three basic components: hardened glass, polysulfide or silicone adhesive and a polymer profile. Each component has its own specific acoustic impedance, which relates to a difference in the ultrasound reflection and transmission coefficients. Several glass façade specimens containing defects like air pockets, grease and duct tape are analysed. Measurements are carried out using a normal incidence piezoelectric transducer. Experiments are performed on several adhesively bonded joints in order to detect the defects in the glass-adhesive and adhesive-polymer profile interfaces. Most of the defects, except smaller areas of grease, can be successfully detected. The experimental results suggest that pulse-echo ultrasonic testing is a reasonable way of evaluating of adhesively bonded joints in glass façades.
Keywords: ultrasonic testing, pulse-echo method, adhesively bonded joints, glass façades

Highlights
- *Presentation of adhesively bonded joints in glass façades.*
- *Choice of a quality evaluation parameter.*
- *Use of pulse-echo ultrasonic method for evaluation of adhesively bonded joints.*
- *Successful detection of contaminants like air pockets, grease and duct tape.*

0 INTRODUCTION

The development of civil engineering and materials science have paved the way for the use of glass façades in an array of different structures. Glass façades are commonly made with hardened glass and polymer profiles, joined together by polysulfide or silicone adhesive. These adhesively bonded joints are required to perform according to predetermined specifications. Joints with low mechanical strength present a flaw in the integrity of the structure and pose a danger in the case of joint failure. In order to prevent low quality bonding, joints have to be evaluated during production and lifecycle. Therefore, a reasonable quality control method is needed.

Adhesively bonded joints can be evaluated using different destructive and non-destructive methods: tensile failure tests, mechanical impedance analysis, as well as thermography and ultrasonic methods. A relationship between a lower bond strength threshold due to contaminants and non-destructive test results can be established [1]. Ultrasonic methods offer an opportunity to evaluate adhesively bonded joints without their mechanical failure. Joint strength cannot be directly measured, but can be indirectly evaluated using the chosen ultrasonic parameters in relation to destructive test results.

The through transmission ultrasonic method of ultrasonic inspection can be used to monitor crosslinking of the adhesive during the curing process [2]. Changes in the transmission spectrum are related to adhesive properties and optimal curing time can be determined. The through transmission method can also be used to evaluate fatigue damage, which generates ultrasonic harmonics in the adhesive layer [3]. An increase in fatigue cycles is related to an increase in the acoustic nonlinearity parameter and early damage can be detected. The high frequency through transmission technique can also be used to evaluate nonlinear behaviour of kissing bonds in adhesively bonded joints [4]. Kissing bonds are a special case, where the adherend and adhesive are in intimate contact, but joint strength is minimal or non-existent. The authors suggest that the measured nonlinearity is highly dependent on the ratio between adhesive layer thickness and ultrasonic wavelength.

The pulse-echo ultrasonic method can be used to detect void disbonds at the front and rear interfaces of adhesively bonded joints in automotive assemblies [5]. Absence of disbonding at the front metal-adhesive interface can be indicated by large deviations in the ultrasonic waveform. At the rear interface, the phenomena of phase inversion can be used as an indication of bond quality. Another application of the pulse-echo method is evaluation of adhesion quality using amplitude ratios of multiple successive reflections [6].

*Corr. Author's Address: University of Ljubljana, Faculty of Mechanical Engineering, Aškerčeva 6, SI-1000 Ljubljana, Slovenia, janez.grum@fs.uni-lj.si

Oblique incidence pitch-catch ultrasonic inspection can be used to evaluate the degradation of adhesively bonded joints of carbon fiber reinforced plastics (CFRP) [7]. Degraded joints exhibit decreased stiffness, a higher reflected signal amplitude and a shift in the frequency minimum towards lower frequencies. A correlation can be established with adhesive bond strength and an assessment can be made regarding the bond quality using this method.

Another example of ultrasonic testing of adhesively bonded joints is the use of shear-horizontally (SH) polarized guided waves [8]. These can be used to quantify the adhesive shear modulus and interfacial shear stiffness as indicators of adhesive bond quality.

The aim of this article is to develop a way of evaluating of adhesively bonded joints in glass façades. For this purpose, pulse-echo ultrasonic tests are performed on various adhesive bond specimens with different flaws and contaminants like air pockets, grease and duct tape. The amplitudes of the reflected ultrasonic signals are used as a quality evaluation parameter and the applicability of the presented method is determined.

1 METHODS AND EXPERIMENTAL

The standard pulse-echo ultrasonic method is based on the emission and reception of sound by an ultrasonic transducer, which is commonly piezoelectric. Generated ultrasonic sound waves travel through a chosen substance and are reflected back at boundary interfaces due to a difference in specific acoustic impedance, which is given by Eq. (1):

$$Z = \rho c, \tag{1}$$

where Z is the specific acoustic impedance [Ns/m^3], ρ density [kg/m^3] and c the sound velocity [m/s]. A greater difference relates to a greater percentage of reflection. This indicates the possibility of differentiation of substances based on their specific acoustic impedance and the reflected signal amplitude. The quality of adhesively bonded joints in glass façades can therefore be evaluated via comparison of test results with a predetermined acceptable reflected signal amplitude.

The coefficients of reflection and the transmission of sound can be determined via the specific acoustic impedance of substances sharing an interface. They are given by Eqs. (2) and (3):

$$R = \frac{Z_2 - Z_1}{Z_2 + Z_1}, \tag{2}$$

$$T = \frac{2Z_2}{Z_2 + Z_1}, \tag{3}$$

where R is the coefficient of reflection [%], T the coefficient of transmission [%] and Z_1, Z_2 the specific acoustic impedance of the first and second given substance, respectively [Ns/m^3].

1.1 Equipment and Parameters

Experiments were performed using a Eurosonic UTC-110 ultrasonic device with attached software. A normal incidence Eurosonic T0506 piezoelectric transducer with a 6 mm diameter and a 4.75 MHz pulse frequency was used. A summary of the testing parameters is provided in Table 1.

Table 1. *Testing parameters*

Parameter	Value
Pulse frequency	4.75 MHz
Voltage	50.15 V
Pulse width	210 ns
Frequency of pulses	1 kHz
Sampling rate	100 MHz
Amplification	13.6 dB to 16 dB

1.2 Specimens

A model of the glass façade specimen is presented in Fig. 1. Dimensions of the specimen are 300 mm × 200 mm × 109 mm. Width of the adhesively bonded joint is 30 mm. A schematic view of the joint is presented in Fig 2. The joint has three basic components with various thicknesses: hardened glass with a thickness of 8 mm, polysulfide or silicone adhesive with a thickness of 3.2 mm and a polyamide PA6.6 polymer profile with a thickness of 2 mm.

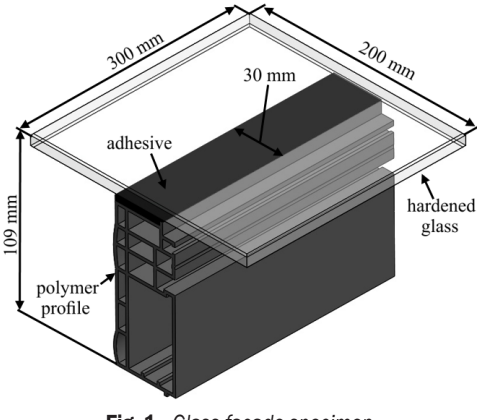

Fig. 1. *Glass façade specimen*

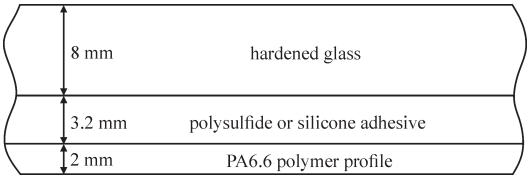

Fig. 2. *Schematic view of the adhesively bonded joint*

2 RESULTS AND DISCUSSION

In this section, several tests of adhesively bonded joints in glass façades are presented. Flaws in glass façades can occur on both interfaces between the glass-adhesive and adhesive-polymer profile. In order to properly evaluate the joint, testing of both interfaces is required. Experiments were performed separately on each interface. The effect of the coupling quality between the ultrasonic transducer and a given material was taken into account. In the case of the glass-adhesive interface, the reflected signal amplitude was amplified for each measurement in order to match the amplitude of the first reflection. This was however not possible in the case of the adhesive-polymer profile interface, as the amplitude of the first reflection was later used as a quality evaluation parameter. Test results on both interfaces are presented in A-scan figures of amplitude over time or length of the joint.

2.1 Interface Glass-Adhesive

The specimen for the glass-adhesive interface test was produced using a polysulfide adhesive. The normal incidence ultrasonic transducer was positioned on the upper side of the glass. Several measurements were taken in different areas of the joint with or without adhesive. The reflected signal amplitude for a bond with adhesive present is presented in Fig. 3. The reflected signal amplitude for an area with no adhesive is presented in Fig. 4. The reflected echo signal decay is greater in cases where adhesive is present, due to a greater part of the sound pressure passing through the adhesive than through air, as the specific acoustic impedance of air is lower than that of the adhesive. The coefficient of reflection is therefore lower in the case where adhesive is present. A comparison of echo decay for both cases is presented in Fig. 5. The amplitude of the main ultrasonic echoes, marked as A_i, was determined using the absolute value of the main ultrasonic echoes. The index i indicates the number of the main echo.

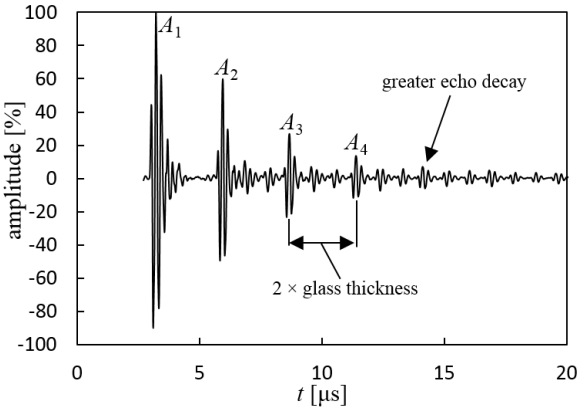

Fig. 3. *Reflected signal amplitude at the glass-adhesive interface, with adhesive present*

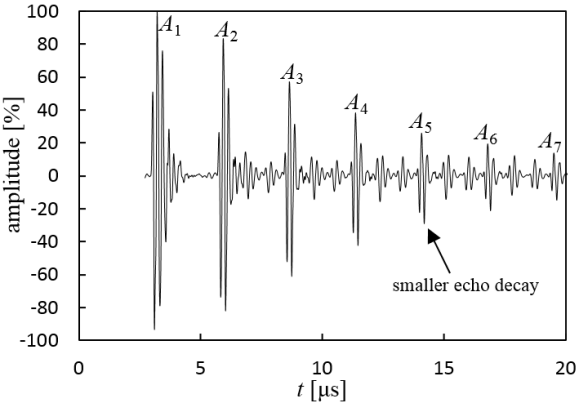

Fig. 4. *Reflected signal amplitude at the glass-adhesive interface, with adhesive absent*

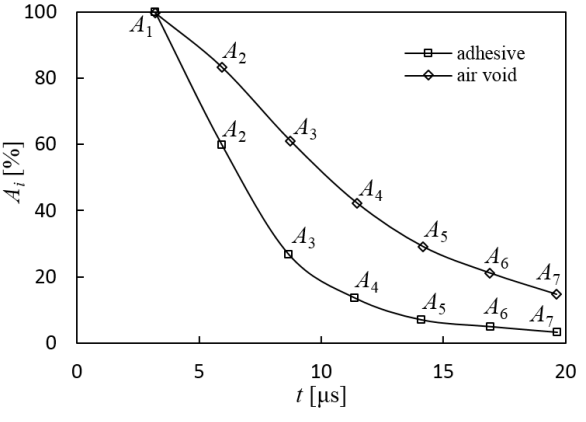

Fig. 5. *Comparison of echo amplitude decay at the glass-adhesive interface*

2.2 Interface Adhesive-Polymer Profile

In the test of the adhesive-polymer profile interface, the specimen was produced using a silicone adhesive. In order to position the ultrasonic transducer on the

lower side of the polymer profile, the profile had to be partially cut. As before, measurements were taken in separate areas with adhesive either present or absent. The echo amplitude in the adhesive-polymer profile interface with adhesive present is presented in Fig. 6. The echo amplitude in adhesive-polymer profile interface with adhesive absent is presented in Fig. 7. The acoustic impedance match of the adhesive-polymer profile interface is greater than that of the glass-adhesive interface, therefore the echo amplitudes are smaller and only one main echo A_1 can be clearly seen in the case where adhesive is present. The echo A_x is reflected from the glass-adhesive interface and is not visible in the case where adhesive is absent, as the ultrasonic waves reflect at the interface where adhesive is absent and do not reach the glass-adhesive interface.

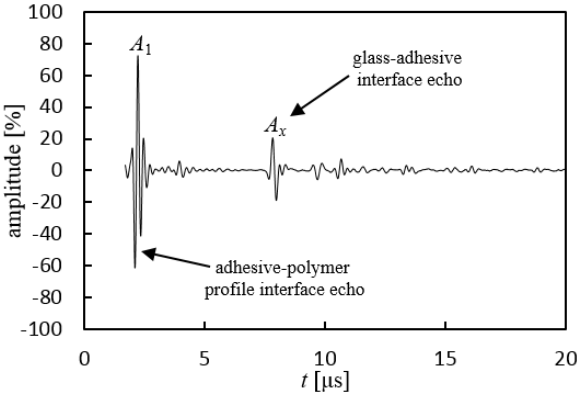

Fig. 6. *Reflected signal amplitude at the adhesive-polymer profile interface, with adhesive present*

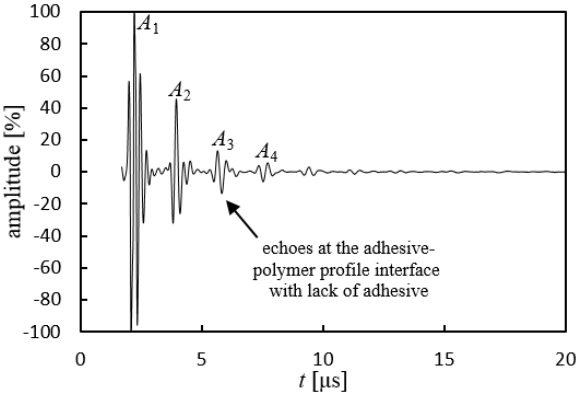

Fig. 7. *Reflected signal amplitude at the adhesive-polymer profile interface, with adhesive absent*

2.3 Quality Evaluation Parameter

In order to evaluate the quality of adhesively bonded joints in glass façades, a parameter from the measured ultrasonic echoes had to be chosen. For the evaluation of the glass-adhesive interface, second, third and fourth reflected echo amplitudes were chosen along with attenuation coefficient α [dB/mm], which is given by Eq. (4):

$$\alpha = \frac{20}{2s} log \frac{A_1}{A_2}, \tag{4}$$

where s is specimen thickness [mm], A_1 first echo amplitude [%] and A_2 second echo amplitude [%]. A comparison was made for bonds with and without adhesive. Ten measurements were taken. The average values are presented in Table 2. Single factor analysis of variance (ANOVA) was used to identify the greatest difference in the measured mean values, as presented in Tables 3 to 6. A standard ANOVA alpha level of 0.05 was used. The critical F value was 4.41 for all cases, based on the degrees of freedom, *df*. The term *SS* abbreviates the sum of squares and *MS* abbreviates mean squares. The null hypothesis suggests that the mean values of the chosen quality evaluation parameters do not significantly differ in the case of a bond with present or absent adhesive. The null hypothesis was rejected for all cases. The third echo amplitude A_3 was chosen as a final quality evaluation parameter for the glass-adhesive interface, as it had the greatest mean value difference of reflected signals between bonds. In order to evaluate the adhesive-polymer profile interface, the first echo amplitude A_1 was chosen, as it was the only clearly present echo in both cases of a bond with or without adhesive.

Table 2. *Average values of amplitude and attenuation*

Joint type	A_2 [%]	A_3 [%]	A_4 [%]	α [dB/mm]
Adhesive	60.46	26.42	14.13	0.28
Air void	84.31	60.83	42.02	0.09

Table 3. *Analysis of variance for echo amplitude A_2*

Variance source	SS [%²]	*df*	MS [%²]	F_0
Between groups	2843.79	1	2843.79	486.67
Within group	105.18	18	5.84	
Total	2948.97	19	P_{value} =1.76E-14	

Table 4. *Analysis of variance for echo amplitude A_3*

Variance source	SS [%²]	*df*	MS [%²]	F_0
Between groups	5920.37	1	5920.37	2199.26
Within group	48.46	18	2.69	
Total	5968.82	19	P_{value} =2.85E-20	

Table 5. *Analysis of variance for echo amplitude* A_4

Variance source	SS [%²]	*df*	MS [%²]	F_0
Between group	3889.43	1	3889.43	1046.09
Within group	66.93	18	3.72	
Total	3956.36	19	P_{value} =2.12E-17	

Table 6. *Analysis of variance for attenuation α*

Variance source	SS [dB²/mm²]	*df*	MS [dB²/mm²]	F_0
Between group	0.1830	1	0.1830	151.82
Within group	0.0217	18	0.0012	
Total	0.2047	19	P_{value} =3.29E-10	

The area of quality was determined by the average value of the measured echo amplitude, A_1 and A_3, each at its own respective interface. Adhesive bond quality was acceptable if the value of the chosen quality evaluation parameter was inside the area of quality. A sample standard deviation of the echo amplitude was calculated from twenty measurements over an area with adhesive present and no defects. Amplitude limits of the area of quality were determined with Eqs. (5) and (6). Eq. (5) was used to assess the area of quality at the glass-adhesive interface, Eq. (6) was used to assess the area of quality at the adhesive-polymer profile interface:

$$Q_{g\text{-}a} = A_{3avg} \pm 2s_3, \tag{5}$$

$$Q_{a\text{-}pp} = A_{1avg} \pm 2s_1, \tag{6}$$

where $Q_{g\text{-}a}$ is the area of quality for the glass-adhesive interface [%], $Q_{a\text{-}pp}$ the area of quality for the adhesive-polymer profile interface [%], A_{iavg} the average echo amplitude [%] and s_i the sample standard deviation [%]. Each area of quality is specific to a given specimen and interface. Different types of glass façades cannot use the same amplitude limits. They have to be determined separately for each type, if this method of quality evaluation is to be applied.

2.4 Testing Joint Quality

In order to test the applicability of the presented method and the quality evaluation parameters, several adhesively bonded joints were evaluated along the length of the glass façade. A specimen was produced with a purposefully wavy deposit of polysulfide adhesive in order to clearly present the difference between a bond with and without adhesive at the glass-adhesive interface. A top view of the specimen is presented in Fig. 8 together with the test results. Measurements were taken every 5 mm in a straight line. The third echo amplitude A_3 was recorded and plotted against joint length. The quality of the joint was unacceptable if the third echo amplitude left the predetermined area of quality. Air voids were easily detected, as they were outside the area of quality. The amplitude difference between a good bond and a bond with a lack of adhesive was as large as 35 %. Small air pockets were also detected and confirmed by visual inspection. The transducer diameter was 6 mm, so only a part of the actual joint width was tested. A matrix array ultrasonic transducer is recommended in order to evaluate the quality of the entire joint.

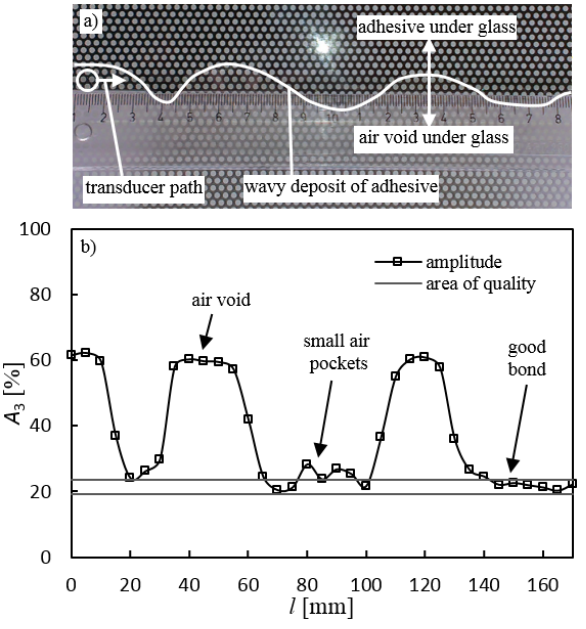

Fig. 8. *Test of the glass-adhesive interface: a) top view of the specimen and b) third echo amplitude along the joint length*

The next specimen was made with silicone adhesive together with interrupted areas of contaminants on the glass-adhesive interface. Contaminants consisted of two areas of grease and an area of duct tape. The tested area of the specimen is presented in Fig. 9 together with the contaminants and the recorded third echo amplitude A_3. Measurements were taken every 3 mm in a straight line. The results show the limits of contaminant detection at the glass-adhesive interface. The second area of grease was detected, while the first area of grease remained undetected. The duct tape area was successfully detected, as shown by a more than a 27 % increase in the third echo amplitude. Contaminant detection in the glass-adhesive interface was therefore dependent on

contaminant type and its arrangement. Very thin areas of grease were difficult to detect.

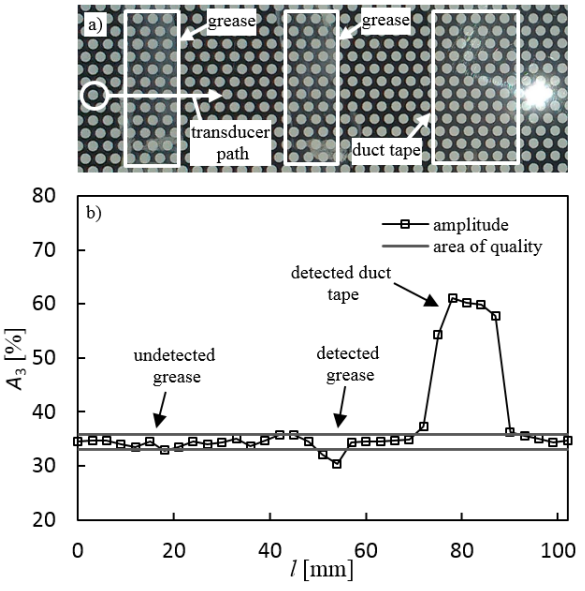

Fig. 9. *Test of the glass-adhesive interface with contaminants: a) top view of the specimen and b) third echo amplitude along the joint length*

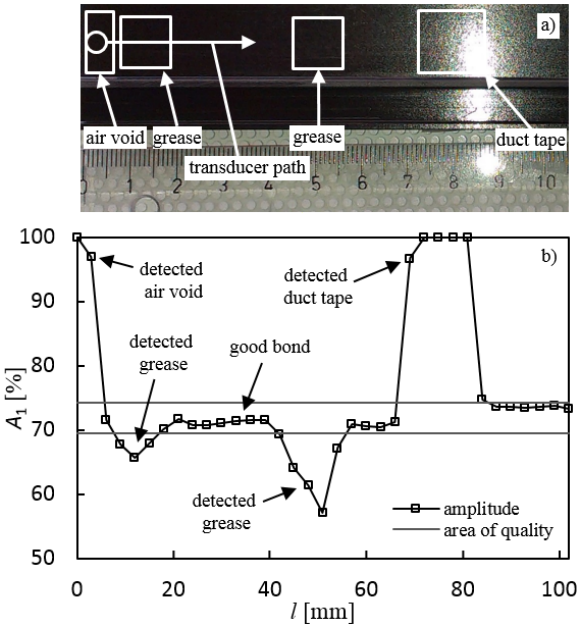

Fig. 10. *Test of the adhesive-polymer profile interface with contaminants: a) top view of the specimen and b) first echo amplitude along the joint length*

As mentioned before, both glass-adhesive and adhesive-polymer profile interfaces have to be evaluated. The next specimen was made with a deposit of silicone adhesive together with contaminants on the adhesive-polymer profile interface. A top view of the specimen is presented in Fig. 10 together with the contaminants and test results. Measurements were taken every 3 mm in a straight line. As per the choice of the quality evaluation parameter, the first echo amplitude A_1 was recorded and plotted against the length of the glass façade. As before, the contaminants consisted of two areas of grease and an area of duct tape. There was also an air void present at the beginning of the joint. The polymer profile is opaque, therefore the contaminants cannot be seen clearly. All contaminants were successfully detected, even the thin areas of grease. Contaminant detection was more successful in the adhesive-polymer profile interface than in the glass-adhesive interface.

3 CONCLUSIONS

This paper presented a non-destructive way of evaluating the quality of adhesively bonded joints in glass façades using the pulse-echo ultrasonic method. Adhesive bond quality can be evaluated via the amplitude of reflected echo signals, which differ in relation to the specific acoustic impedance of a given material's interface. Two quality evaluation parameters were chosen. For evaluating the glass-adhesive interface, the third echo amplitude A_3 was chosen on the basis of a single factor analysis of variance. For evaluating the adhesive-polymer profile interface, the first echo amplitude A_1 was chosen, as it was the only echo present in both cases of a bond with and without adhesive. Acceptable areas of quality bonding were determined for each specific type of adhesive and interface separately, using the same applied theory. This method of quality evaluation can be used to detect air voids and contaminants like grease and duct tape on both bond interfaces, although very thin areas of grease are hard to detect on the glass-adhesive interface. It is important to note that only flaws at the interfaces can be detected. For the detection of flaws inside the adhesive layer, other methods are required, e.g. through thickness resonance method. For testing adhesively bonded joints in glass façades, the pulse-echo ultrasonic method should be used in conjunction with matrix array transducers in order to cover larger areas and to produce easily understandable C-scan figures.

4 REFERENCES

[1] Roach, D., Rackow, K., Duvall, R. (2010). Innovative use of adhesive interface characteristics to nondestructively quantify

the strength of bonded joints. *10th ECNDT Moscow Conference Proceedings*.

[2] Budzik, M.K., Mascaro, B., Jumel, J., Castaings, M., Shanahan, M.E.R. (2012). Monitoring of crosslinking of a DGEBA-PAMAM adhesive in composite/aluminium bonded joint using mechanical and ultra-sound techniques. *International Journal of Adhesion and Adhesives*, vol. 35, p. 120-128, **DOI:10.1016/j.ijadhadh.2012.02.009**.

[3] Shui, G., Wang, Y.S., Huang, P., Qu, J. (2015). Nonlinear ultrasonic evaluation of the fatigue damage of adhesive joints. *NDT & E International*, vol. 70, p. 9-15, **DOI:10.1016/j.ndteint.2014.11.002**.

[4] Yan, D., Neild, S.A., Drinkwater, B.W. (2012). Modelling and measurement of the nonlinear behaviour of kissing bonds in adhesive joints. *NDT & E International*, vol. 47, p. 18-25, **DOI:10.1016/j.ndteint.2011.12.003**.

[5] Titov, S.A., Maev, R.G., Bogachenkov, A.N. (2008). Pulse-echo NDT of adhesively bonded joints in automotive assemblies. *Ultrasonics*, vol. 48, no. 6-7, p. 537-546, **DOI:10.1016/j.ultras.2008.07.001**.

[6] Korzeniowski, M., Piwowarczyk, T., Maev, R.G. (2014). Application of ultrasonic method for quality evaluation of adhesive layers. *Archives of Civil and Mechanical Engineering*, vol. 14, no. 4, p. 661-670, **DOI:10.1016/j.acme.2013.10.013**.

[7] Kumar, R.L.V., Bhat, M.R., Murthy, C.R.L. (2013). Some studies on evaluation of degradation in composite adhesive joints using ultrasonic techniques. *Ultrasonics*, vol. 53, no. 6, p. 1150-1162, **DOI:10.1016/j.ultras.2013.01.014**.

[8] Castaings, M. (2014). SH ultrasonic guided waves for the evaluation of interfacial adhesion. *Ultrasonics*, vol. 54, no. 7, p. 1760-1775, **DOI:10.1016/j.ultras.2014.03.002**.

Strojniški vestnik - Journal of Mechanical Engineering 62(2016)3, 154-162
© 2016 Journal of Mechanical Engineering. All rights reserved.
DOI:10.5545/sv-jme.2015.2663 Original Scientific Paper
Received for review: 2015-05-07
Received revised form: 2015-09-16
Accepted for publication: 2015-12-01

Experimental Study Regarding the Cavitation and Corrosion Resistance of Stellite 6 and Self-Fluxing Remelted Coatings

Costel-Relu Ciubotariu[1,*] – Evelina Secosan[1] – Gabriela Marginean[2] – Doina Frunzaverde[1] – Viorel Constantin Campian[1]

[1] University Eftimie-Murgu, Faculty of Engineering and Management, Romania
[2] Westfälische Hochschule Gelsenkirchen, Germany

This paper aims to compare cobalt-based (type Stellite 6) and nickel-based self-fluxing alloys (type NiCrBSiMo) regarding both their cavitation erosion resistance and corrosion resistance. The two types of protective layers were thermally sprayed onto a substrate of martensitic stainless steel. In order to improve the layers' characteristics and their metallurgical bonding to the substrate, the Stellite 6 coating was laser remelted, while the NiCrBSiMo coating was treated by flame fusion. The cavitation erosion resistance of the two materials was evaluated by measurements of the mean depth of erosion developed during a testing period of 165 minutes, using a 20 kHz ultrasonic vibrator at a peak-to-peak amplitude of 50 μm. In addition, the corrosion resistance of the layers was assessed by potentiodynamic corrosion tests carried out in H_2SO_4 + NaCl solution at room temperature, using calomel as reference electrode. In order to highlight the differences regarding the behaviour of the two protective materials, the authors also carried out microstructural investigations of the layers before and after exposure to cavitation and corrosion. The investigations showed that both types of layers can provide improved protection of the martensitic stainless steel substrate against cavitation, whilst the NiCrBSiMo coating additionally confers significantly increased resistance to corrosion.

Keywords: cavitation, self-fluxing alloys, Stellite 6, corrosion, laser remelting

Highlights

- *With the aim to develop new techniques for the improvement of the hydropower components' lifetime, the authors of this paper carried out a comparative study regarding the resistance of Stellite 6 and NiCrBSiMo coatings against both cavitation and corrosion;*
- *In order to have a clear image of the evolution of the cavitation erosion, the results obtained in the laboratory tests have been processed statistically by carrying out dispersion strips;*
- *The investigations showed that both types of layers can provide for the martensitic stainless steel, usually used for manufacturing turbine components, improved protection against cavitation, whilst the NiCrBSiMo coating supplementary confers also significant increased resistance to corrosion.*

0 INTRODUCTION

Hydropower is a renewable source of energy, non-polluting and probably the oldest source, which transforms the potential energy of water into mechanical energy by means of hydraulic turbines [1]. Hydropower quality is dependent on the durability and reliability of the hydraulic machinery. Surface damages caused by fatigue, corrosion and wear, in particular cavitation erosion, are among the main causes that lead to the failure of hydropower plant components.

Cavitation is a phenomenon caused by the formation of vapour bubbles in low-pressure regions, followed by their collapse in high-pressure regions [2]. As a result, the metallic surfaces in the vicinity are subjected to erosive wear [3] and [4]. In some cases, cavitation pitting is also accompanied by corrosion damage. Usually, hydraulic components are cast from soft martensitic stainless steels, which contain a small amount of ferrite, assuring an excellent resistance to cavitation erosion. Nevertheless, cavitation erosion cannot be completely avoided and improper material quality or inadequate repair techniques applied in situ sometimes lead to significant material loss and even failure of the hydraulic components due to cavitation [5].

Cavitation in hydro turbines is difficult to avoid completely, but it can be reduced to an economically acceptable level. Several experimental research [6] to [8] and analytical studies [9] to [11] investigate the process of cavitation and its consequences in hydro turbines.

In spite of design changes of the turbine components and the use of high quality stainless steels [12] and [13] or protective coatings [14] to [16], in the case of some applications, the level of cavitation erosion remains unacceptable; consequently, specialists continue to search for solutions. Some studies regarding the investigation of these protective coatings in environments containing a mixture of sulfuric acid with different oxidizing or reducing

*Corr. Author's Address: University Eftimie-Murgu, Faculty of Engineering and Management, Traian Vuia Square, no. 1-4, Resita, Romania, r.ciubotariu@uem.ro

impurities, such as chlorides, have been reported by some authors [17] and [18]. Therefore, the corrosion resistance of the present coatings was considered as well for this work. In this study, two types of thermally sprayed and subsequently remelted protective coatings were investigated regarding their microstructure and cavitation and corrosion resistance.

The results were compared to those obtained on the martensitic stainless steel (type 13-4) commonly used as base material for manufacturing of hydraulic turbine components.

1 EXPERIMENTAL PROCEDURE

1.1 Materials and Processes

The two protective coatings investigated in this study were deposited on martensitic stainless steel type 1.4313 (0.03 % C, 12.6 % Cr, 3.63 % Ni, 0.46 % Si and 0.71 % Mn) using a DJH 2700 high-velocity oxy-fuel (HVOF) spraying equipment. Table 1 presents the chemical composition and the particle size of the powders used, the thickness of the deposited cobalt-based alloy (Stellite 6) and the nickel-based self-fluxing (NiCrBSiMo) coating.

Prior to spraying, a sand-blasting machine was used to roughen the working surface of the stainless steel substrate to enhance the coating/substrate adhesion. The coatings deposited by thermal spraying usually present a mixture of lamellar-melted and half-melted or non-melted particles, a certain content of oxides and/or internal porosity. In order to refine the structure and to improve the layers' adhesion to the substrate, the Stellite 6 (St6) coating was remelted by laser treatment [19], whereas the self-fluxing alloy (SF) was subsequently fused using an oxy-fuel torch.

After spraying and remelting, the coatings were examined in cross-section with a scanning electron microscope (SEM/Philips XL30 ESEM), combined with energy dispersive X-ray analysis (EDX/Company) at magnifications between 80× and 500×, in order to characterize the microstructure, the quality of the interface coating/substrate and the thickness of the deposited layers. In addition, the phase composition was determined by means of X-ray diffractometry (Philipy X'Pert). The cavitation erosion and corrosion resistance of these coatings was evaluated in comparison with that of the martensitic substrate.

1.2 Cavitation Erosion Test

The cavitation erosion resistance of the samples was determined in deionized water under laboratory conditions using the vibratory method standardized by ASTM G-32 [20]. The vibration-induced pressure fluctuations were adapted to induce cavitation erosion. The vibration is transmitted by a booster (mechanical transformer of vibration) and a horn to the test specimen, which is immersed in liquid.

The cavitation equipment used in the Center for Research in Hydraulics, Automation and Thermal Processes of the Eftimie Murgu University of Resita uses an ultrasonic device and a piezoelectric converter to generate vibrations at the frequency of 20 kHz and the peak-to-peak amplitude of 50 μm. The testing period was 165 minutes; the water temperature was maintained at a constant value (25±2 ºC) with a circulatory system, and the mass loss was measured with an electronic balance at a resolution of 10^{-5} g. In order to compare materials with different densities, a volume parameter, the mean depth of erosion (MDE), has been used. In the case of the direct method, the vibratory device generates oscillations on a test specimen that is attached at the horn (by a thread) and submerged in liquid at a certain depth.

The unit consists of the following components: ultrasonic generator and cavitation stand with piezoelectric converter, booster, sonotrode with the specimen, and cooling bath. Fig. 1 shows the stand of cavitation erosion testing.

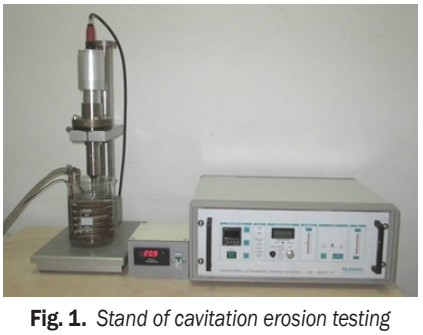

Fig. 1. *Stand of cavitation erosion testing*

Table 1. *Chemical composition and particle size of the feedstock powders, thickness of the sprayed layers*

Powder	Composition [%]								Particle size [μm]	Layer thickness
	Ni	Cr	W	C	Fe	Si	B	Mo		
Stellite 6 (Co alloy)	3.26	27 to 32	4 to 6	0.9 to 1.4	2.26	-	-	4 to 6	–45 / 15	468 μm
Self-fluxing (NiCrBSiMo)	base	16.5	-	0.55	3	4.5	3.8	5	–106 / 45	1.04 mm

1.3 Corrosion test

The corrosion behaviour was evaluated using potentiodynamic polarization tests that were conducted with a potentiostat/galvanostat and a three-electrode cell (Voltalab) in the presence of $0.5\,M\,H_2SO_4 + 3.5\,\%\,NaCl$ solution at room temperature. A platinum wire, a saturated calomel electrode (SCE), and polished specimens were used as the counter electrode, reference electrode, and working electrode respectively.

Potentiodynamic polarization curves were measured from –1000 mV to 1500 mV at a sweep rate of 5 mV/min and a room temperature of approximately 20 °C.

2 RESULTS AND DISCUSSIONS

2.1 Microstructure

The SEM micrographs of the HVOF-sprayed St6 coating presented in Fig. 2 show a relatively homogeneous structure at lower magnitude (Fig. 2a). A further investigation of this coating at higher magnitude (500×) reveals the presence of some dark grey inhomogeneities with irregular shapes. EDX analysis performed on these dark grey formations revealed (beside Co) a high amount of Cr, Si, and O (see Fig. 3). Moreover, even though the degree of adhesion seems to exhibit a good quality for the HVOF-sprayed coating, there are still many impurities along the interface coating/substrate (see Fig. 2b).

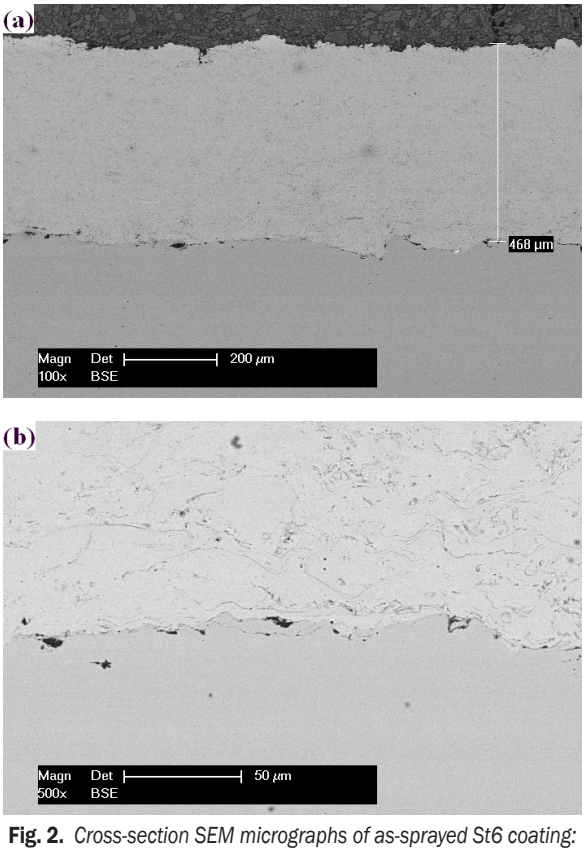

Fig. 2. *Cross-section SEM micrographs of as-sprayed St6 coating: a) 100x; b) 500x*

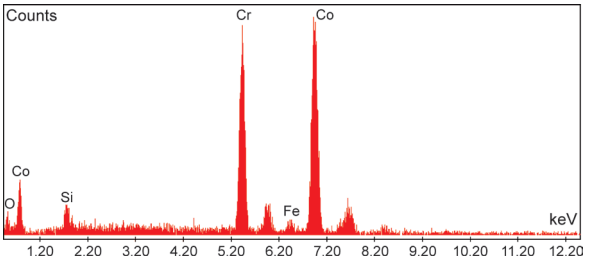

Fig. 3. *EDX-spectrum of the dark grey strings visible in the as-sprayed St6 coating*

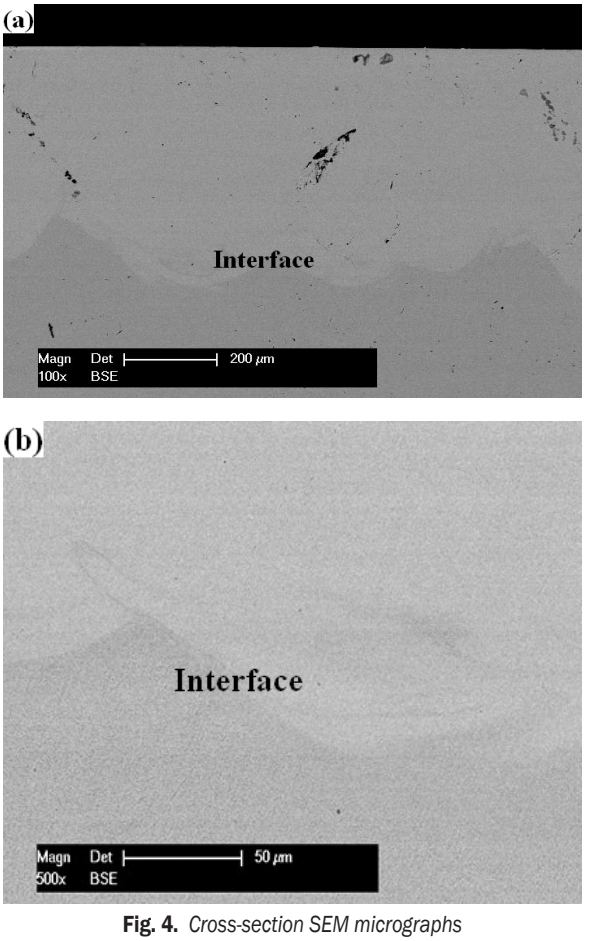

Fig. 4. *Cross-section SEM micrographs of laser remelted St6 coating/substrate interface; a) lower magnitude and b) higher magnitude*

Remelting the St6 coating via laser treatment led to a refinement of the microstructure. Cross-section SEM-micrographs of the remelted coating show a very high degree of homogeneity and purity. The internal porosity was eliminated, and the coating/substrate interface exhibited a clean structure without cracks or inclusions as can be seen in Fig. 4.

XRD investigations of the laser remelted coating revealed (beside Cr and Co phases) a high amount of intermetallic compound with a quite low W content (type $Co_{0.9}W_{0.1}$; see Fig. 5). Moreover, a small amount of another Co/W phase was detected, with another ratio between the elements (Co_3W). The XRD data for St6 matches with the ICDD reference patterns: $Co_{0.9}W_{0.1}$ (03-065-9928); Co_3W (01-071-7505); Co (00-001-1277); Cr (00-019-0323).

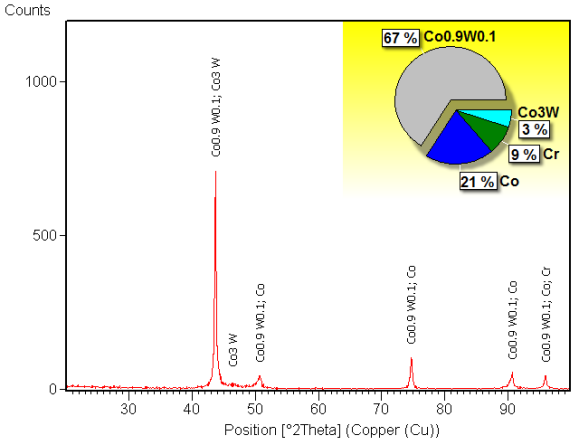

Fig. 5. *X-ray diffraction pattern of the laser remelted St6 coating*

The cross-section SEM-micrographs of the flame sprayed NiCrBSiMo coating presented in Fig. 6 exhibit a poor adhesion to the substrate with many oxides and micro cracks. At higher magnitude, there is obviously that the degree of interconnection respectively adhesion between two adjacent particles is very low. Much porosity and even some non-melted particles are clearly observed (Fig. 6b). The microstructure of this coating was substantially refined after the fusing process. The degree of internal porosity was considerably reduced, and the adhesion to the substrate was improved as well (see Fig. 7). In order to identify various structural constituents to emphasize the microstructure of the fused coating some EDX measurements were performed along the coating in cross-section.

The results obtained from the EDX analysis, which were compared with the XRD-pattern of this coating, lead to the conclusion that the light grey constituent with a dendritic structure is composed of a

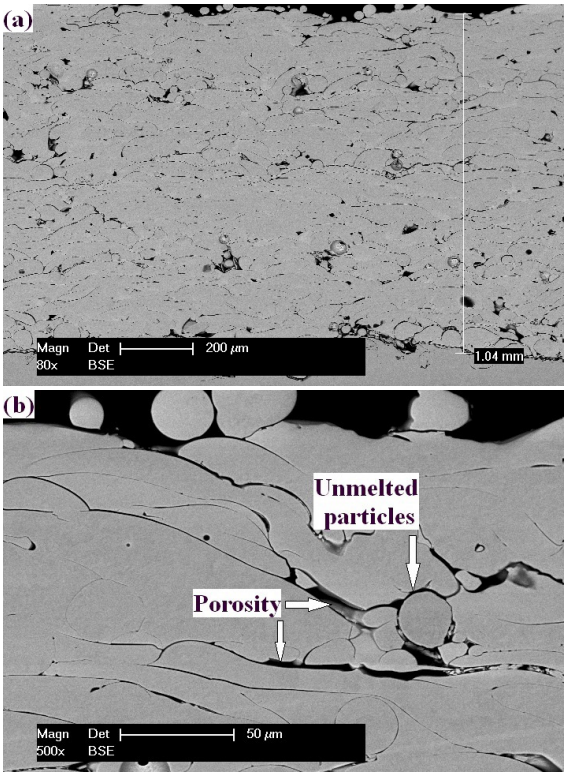

Fig. 6. *SEM micrographs of the as-sprayed NiCrBSiMo coating in cross-section; a) lower magnitude and b) higher magnitude*

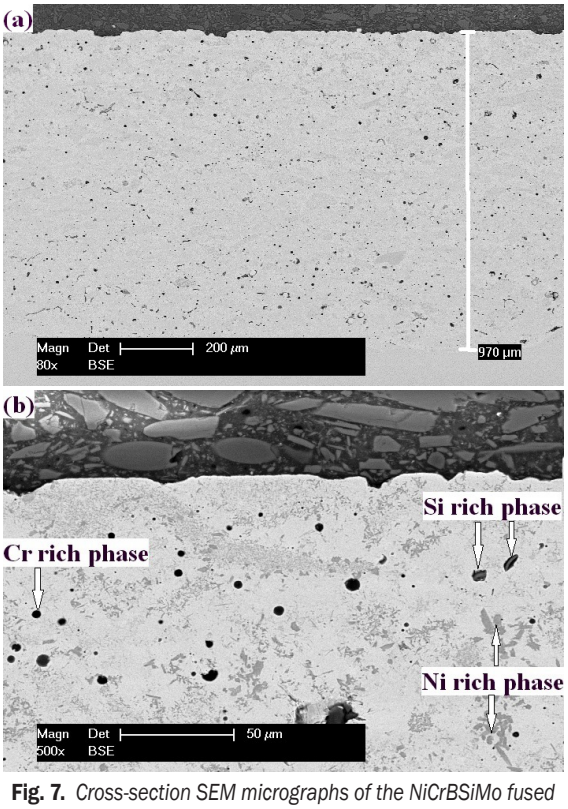

Fig. 7. *Cross-section SEM micrographs of the NiCrBSiMo fused coating; a) magnitude 80x and b) magnitude 500x*

nickel-rich phase, probably Ni_3B (see Fig. 8a). In Fig. 8c, the black globular formations in the layer consist of a Cr-rich phase (Cr_2O_3 or CrB). Some constituents with irregular shapes, which exhibit a combination of dark grey to light grey, comprise a Si-rich phase, possibly surrounded by oxides (see Fig. 8b). The XRD-pattern of the fused NiCrBSiMo coating (Fig. 9) shows (beside the $Ni/CrNi_3$ signal γ'-$CrNi_3$ phase fine dispersed into the γ-Ni matrix) also Ni and Cr borides as well as iron silicide's. The ICDD reference patterns for the self-fluxing alloy are: $CrNi_3$ (01-071-7595); Fe (00-050-1275); $Fe5Si_3$ (01-074-4744); Ni_3B (01-082-1699); CrB (01-075-1159).

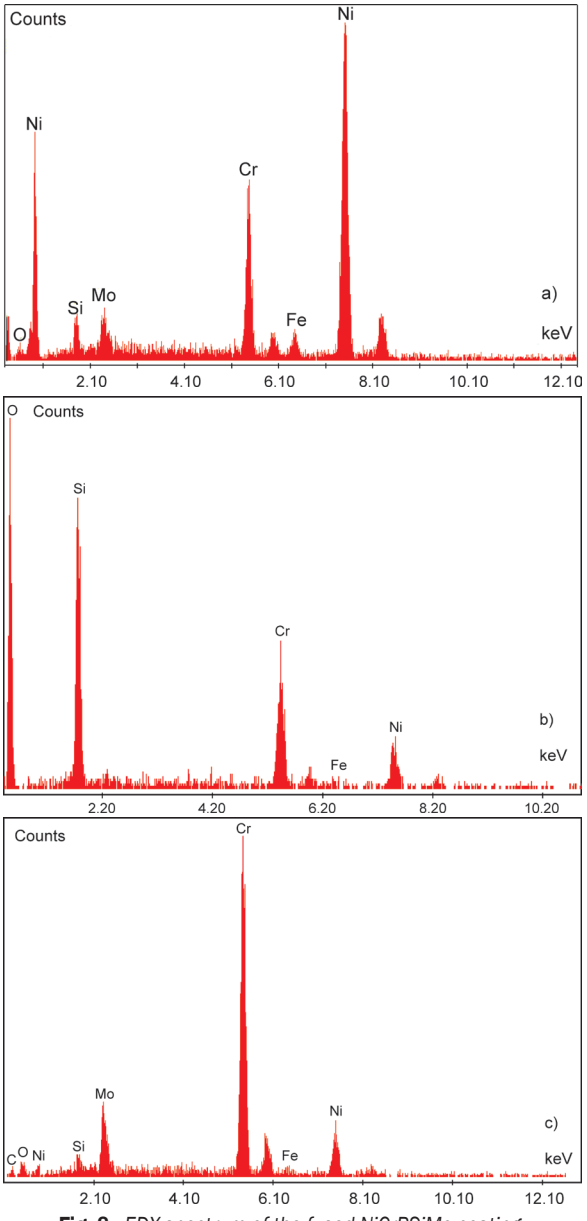

Fig. 8. *EDX-spectrum of the fused NiCrBSiMo coating; a) nickel phase, b) silicon phase, and c) chromium phase*

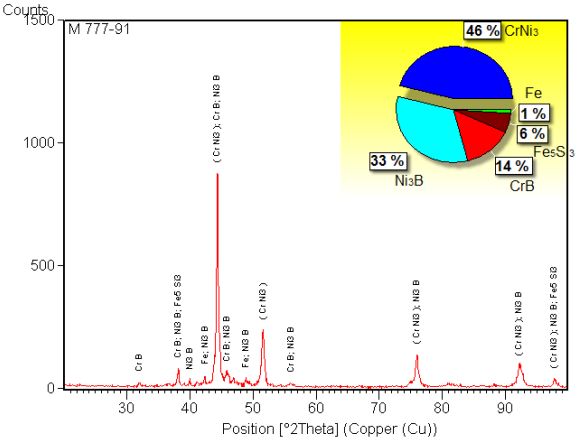

Fig. 9. *X-ray diffraction pattern of the fused NiCrBSiMo coating*

2.2 Cavitation Erosion Resistance

The primary result of an erosion test is the cumulative mass loss. Although, in terms of mass loss versus time, the raw data are for analysis and reporting purposes, this should be converted to a "mean depth of erosion" (MDE) versus time curve, since a volumetric loss is more significant than a mass loss when materials of different densities are compared. Calculate the mean depth of erosion, for the purpose of this test method in conformity with ASTM G-32 [20], with Eq. (1):

$$MDE = \frac{10^6 \cdot \Delta m}{\rho \cdot A_e}, \qquad (1)$$

where the following abbreviations have been used: Δm [mg] mass variation; A_e [mm²] area of the eroded surface; ρ [kg/m³] density of the coating exposed to erosion.

Characteristic curves of the mean depth of erosion for the investigated coatings are presented in comparison with that of the martensitic stainless steel substrate, which were tested in the same system (see Fig. 10).

It is noted that both coatings exhibited lower values of the MDE in comparison with the base material. Furthermore, the stabilization rate (Vs) of the cavitation erosion of the two protective layers is lower (values for the MDE and Vs of the tested samples are presented in Table 2). The incubation period for all surfaces tested was: Martensitic stainless steel to 30 minutes; Co base alloy to 70 minutes and Self-fluxing alloy to 45 minutes.

In order to have a clear image of the evolution of the cavitation erosion, the results obtained in the laboratory tests have been processed statistically by carrying out dispersion strips (see Fig. 11) which result from the estimated error and the polynomial regression curve of the 2nd degree. These bands resulted from using the average values of the cumulative mass losses (CML) for the three samples.

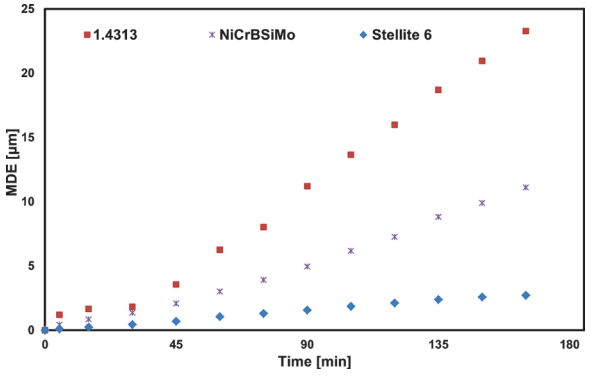

Fig. 10. *Mean depth of erosion against time of cavitation attack for the tested materials (Martensitic stainless steel, self-fluxing alloy, and Co-based alloy)*

Table 2. *Values for mean depth of erosion to 165 minutes and stabilization rate (V_s) for all tested surfaces*

Measurements	1.4313	NiCrBSiMo	St6
MDE [μm]	23.27	11.10	2.70
V_s [mm³/min] × 10⁻²	3.12	1.62	0.18

The approximated values for the curves shown in Figs. 11a to 11c were obtained based on the experimental measurements for each material type. The values for the tested materials fall within the error ranges specific for each material. The maximum value of the estimated error and the cumulated mass loss value for all surfaces tested are shown in Table 3.

Table 3. *Time evolution of the cavitation erosion and experimental values versus statistical values*

Samples	1.4313	NiCrBSiMo	St6
Experimental cumulative mass losses [mg]	36.01	15.17	4.46
Maximum value of the estimate error [mg]	37.18	15.39	4.62

Analysing the results presented in Tables 2 and 3 and in Fig. 10 reveals that in the case of testing by the direct ultrasonic method, the Co-based alloy has the highest resistance to cavitation erosion followed closely by the self-fluxing alloy. In the case of the Co-based alloy sample, the lowest value for cumulated mass losses (4.46 mg) was registered at a mean depth of erosion of 2.7 µm. Compared with the martensitic stainless steel used as the substrate, the St6 showed a stabilization rate of erosion of approximately 17 times lower. Good resistance to cavitation was alse seen in case of the self-fluxing alloy with the cumulated mass loss of 15.17 mg, MDE of 11.10 µm and stabilization rate of approximately two times lower than that of the base material.

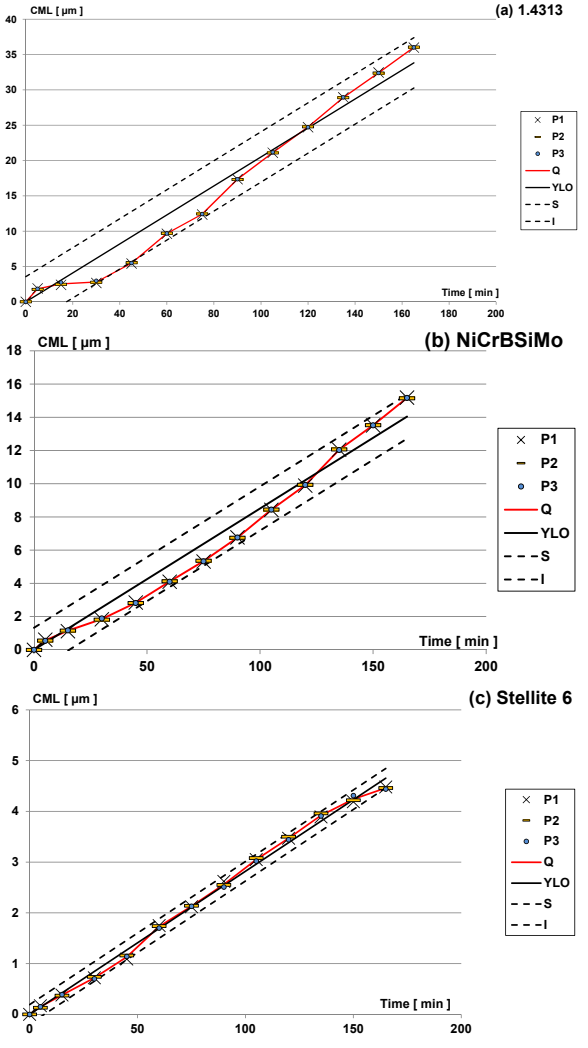

Fig. 11. *The error ranges for all samples tested to cavitation erosion for a) martensitic stainless steel, b) self-fluxing alloy and c) Co-based alloy; P1, P2 and P3 are all three samples tested; Q the average cumulative to mass losses; YLO polynomial regression curve; S upper range value of tolerance and I lower range value of tolerance*

Fig. 12 presents SEM-micrographs of the samples before and after the cavitation tests. It can be observed that at the end of the total period of exposure to cavitation the Co-based alloy and the martensitic

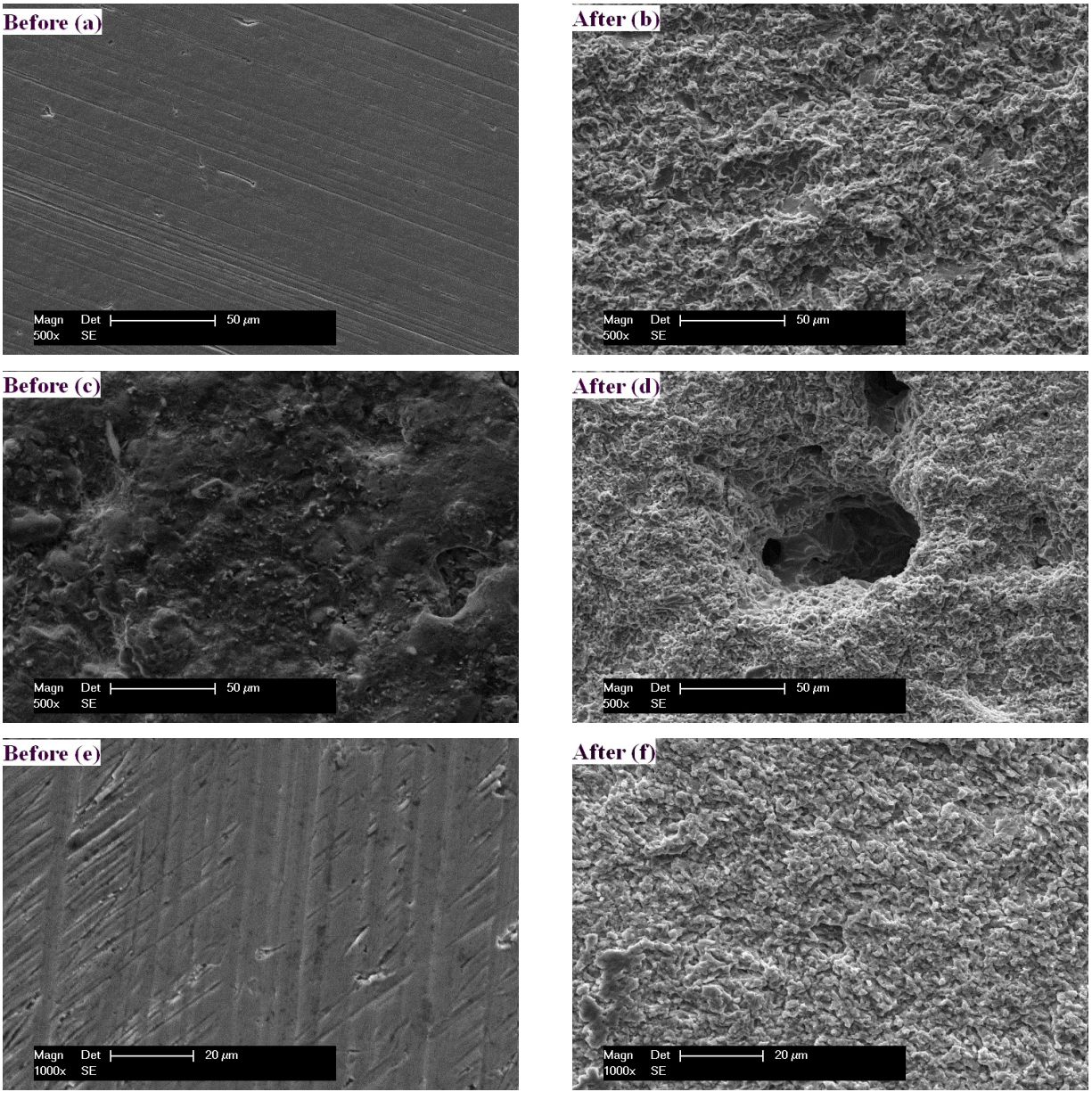

Fig. 12. *SEM micrographs of the samples surface before and after cavitation erosion; a) and b) martensitic stainless steel; c) and d) self-fluxing alloy; e) and f) Co-based alloy*

stainless steel show a uniform degradation of the entire surface, whereas the surface of the self-fluxing alloy exhibited material spallation in the form of crippling caverns specific for cavitation erosion.

2.3 Corrosion Resistance

From the polarization curves of the tested materials, it can be seen that significant modification in the corrosion resistance of the sample surfaces occurred. This can be observed by comparing the values for the corrosion potential (U_{corr}) respectively for the corrosion current density (i_{corr}) of the three samples. The i_{corr} values for the investigated coatings are clearly lower than that of the base material. Low values for i_{corr} as well as more cathodic potentials for E_{corr} are indicators for a good corrosion resistance.

This theoretical affirmation leads to the conclusion that the best corrosion resistance was exhibited from the NiCrBSiMo coating followed by

St6. Although the values for the icorr are quite similar for the tested coatings (see Fig. 13), based on the fact that the corrosion potential of St6 is more anodic, one may conclude that the corrosion resistance of this material is lower than that of the fused self-fluxing alloy.

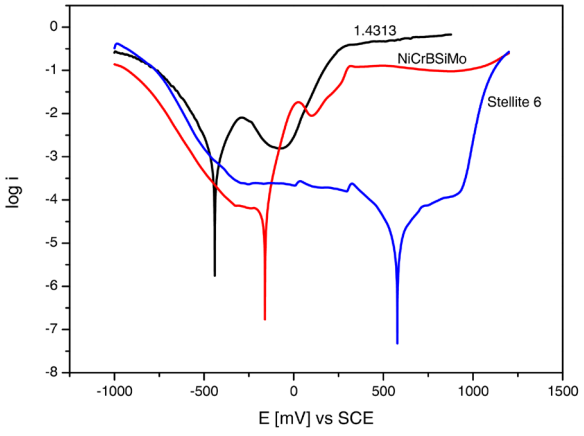

Fig. 13. *Polarization curves of the samples tested in a 0.5M H_2SO_4 + 3.5% NaCl solution at room temperature*

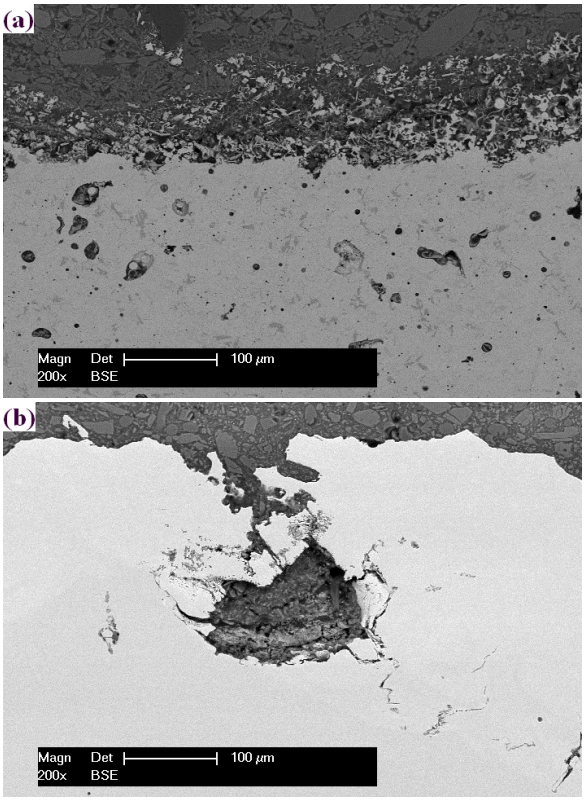

Fig. 14. *Cross-section SEM micrographs of the corroded samples; a) NiCrBSiMo coating and b) St6 coating*

This observation is confirmed by the SEM micrographs of the corroded coatings in the cross-section that reveal a homogeneous corrosion attack over the entire sample surface in the case of the self-fluxing alloy (Fig. 14a), whereas in the case of the St6 coating, a certain degree of localized corrosion attack occurs (pitting attack due to the presence of chlorine ions (Fig. 14b).

3 CONCLUSIONS

The results of the performed investigations revealed that the two types of protective layers (St6 and NiCrBSiMo) assure a considerable improvement of the resistance to cavitation erosion and corrosion compared to that of the soft martensitic stainless steel substrate.

The Co-based alloy exhibited the highest resistance to cavitation erosion during testing by the direct ultrasonic method, while the corrosion resistance, although better than that of the martensitic substrate, should be treated with caution because of the undesirable pitting attack.

In contrast, the NiCrBSiMo coating exhibited excellent corrosion resistance, especially due to the corrosion mechanism, which leads to the uniform corrosion of the surface, combined with an improved cavitation resistance in comparison to that of the martensitic substrate.

Based on the obtained results, it may be concluded that the investigations carried out by the authors show that both types of layers can provide proper protection of the martensitic stainless steel substrate against cavitation, whilst the nickel-based self-fluxing alloy supplementary also confers significantly increased resistance to corrosion.

4 ACKNOWLEDGMENTS

The work has been funded by the Sectorial Operational Programme Human Resources Development 2007-2013 of the Ministry of European Funds through the Financial Agreement POSDRU/159/1.5/S/132395.

5 REFERENCES

[1] Tong, D. (1981). Cavitation and wear on hydraulic machines. *International Water Power and Dam Construction*.

[2] Biluš, I., Bombek, G., Hočevar, M., Širok, B., Cenčič, T., Petkovšek, M. (2014). The experimental analysis of cavitating structure fluctuations and pressure pulsations in the cavitation station. *Strojniški vestnik – Journal of Mechanical Engineering*, vol. 60, no. 3, p. 147-157, **DOI:10.5545/sv-jme.2013.1462**.

[3] Haosheng, C., Jiang, L., Darong, C., Jiadao, W. (2008). Damages on steel surface at the incubation stage of the

vibration cavitation erosion in water. *Wear*, vol. 265, no. 5-6, p. 692-698, **DOI:10.1016/j.wear.2007.12.011**.

[4] Laguna-Camacho, J.R., Lewis, R., Vite-Torres, M., Mendez-Mendez, J.V. (2013). A study of cavitation erosion on engineering materials. *Wear*, vol. 301, no. 1-2, p. 467-476, **DOI:10.1016/j.wear.2012.11.026**.

[5] Frunzaverde, D., Câmpian, C.V., Mărginean, G. (2006). Metallographic investigations on anti-cavitation lips of kaplan blades. *Symposium on Hydraulic Machinery and Systems*, International Association of Hydraulic Research, Yokohama.

[6] Dular, M., Širok, B., Stoffel, B. (2005). The influence of the gas content of water and the flow velocity on cavitation erosion aggressiveness. *Strojniški vestnik – Journal of Mechanical Engineering*, vol. 51, no. 3, p. 132-145.

[7] Hattori, S., Takinami, M. (2010). Comparison of cavitation erosion rate with liquid impingement erosion rate. *Wear*, Vol. 269, no. 3-4, p. 310-316, **DOI:10.1016/j.wear.2010.04.020**.

[8] Santa, J.F., Blanco, J.A., Giraldo, J.E., Toro, A. (2011). Cavitation erosion of martensitic and austenitic stainless steel welded coatings. *Wear*, vol. 271, no. 9-10 p. 1445-1453, **DOI:10.1016/j.wear.2010.12.081**.

[9] Cojocaru, V., Campian, C.V. Miclosina, C.O. (2011). Experimental analysis of residual stresses in samples of austenitic stainless steel welded on martensitic stainless steel used for Kaplan blades repairs. *Annals of „Eftimie Murgu" University*, vol. 18, no. 1, p. 161-166.

[10] Mostafa, N.H., Mohamed A. (2012). Unsteady numerical simulation of cavitation in axial turbine. *CFD Letters*, vol. 4, no. 3, p. 140-149.

[11] Muntean, S., Susan-Resiga, R.F., Bernad, S., Ioan, A. (2004). Analysis of the GAMM Francis turbine distributor 3D flow for the operating range and optimization of the guide vane axis location. *The 6th International Conference on Hydraulic Machinery and Hydrodynamics*, Timisoara, p. 131-136.

[12] Park, M.C., Shin, G.S., Yun, J.Y., Heo, J.H., Kim, D.I., Kim, S.J. (2014). Damage mechanism of cavitation erosion in austenite-martensite phase transformable Fe–Cr–C–Mn/Ni alloys. *Wear*, vol. 310, no. 2, p. 27-32, **DOI:10.1016/j.wear.2013.12.015**.

[13] Espitia, L.A., Toro, A. (2010). Cavitation resistance, microstructure and surface topography of materials used for hydraulic components. *Tribology International*, vol. 43, no. 11, p. 2037-2045, **DOI:10.1016/j.triboint.2010.05.009**.

[14] Cojocaru, V., Frunzaverde, D., Campian, C.V., Marginean, G., Ciubotariu, R., Pittner, A.M. (2010). Cavitation erosion investigations on thermal spray coatings. *International Conference Proceedings on Engineering Mechanics, Structures, Engineering Geology,* p. 177-180.

[15] Secosan, E.R., Ciubotariu, C.R., Cojocaru, V., Frunzaverde, D., Campian, C.V. (2014). Study regarding the cavitation erosion behavior and residual stresses of impact resistant hardfacing materials. *Advanced Materials Research*, vol. 1029, p. 146-151, **DOI:10.4028/www.scientific.net/AMR.1029.146**.

[16] Romo, S.A., Santa, J.F., Giraldo, J.E., Toro, A. (2012). Cavitation and high-velocity slurry erosion resistance of welded Stellite 6 alloy. *Tribology International*, vol. 47, p. 16-24, **DOI:10.1016/j.triboint.2011.10.003**.

[17] Nickelinstitute (2015). From *http://www.nickelinstitute.org/~/Media/Files/TechnicalLiterature/TheCorrosionResistanceofNickel_ContainingAlloysinSulphuricAcidandRelatedCompounds_1318_.pdf*, accessed on 2015-10-28.

[18] High-Performance Alloys for Resistance to Aqueous Corrosion (2000). From *http://www.google.de/url?sa=t&rct=j&q=&esrc=s&source=web&cd=10&ved=0CFIQFjAJahUKEwiP8YKv4c3HAhXCXiwKHRRIBrk&url=http%3A%2F%2Fwww.parrinst.com%2Fde%2Ffiles%2FParr_Inconel-Incoloy-Monel-Nickel-Corrosion-Info.pdf&ei=FV7hVc-SM8K9sQGUypnICw&usg=AFQjCNFqeLWaGWyTvn5WUA1FHiRNKNDmHQ*, accesed on 2015-10-28.

[19] Ciubotariu, C.R., Frunzaverde, D., Marginean, G., Serban, V.A., Birdeanu, A.V. (2016). Optimization of the laser remelting process for HVOF-sprayed Stellite6 wear resistant coatings. Optics & Laser Technology, vol. 77, p. 98-103, **DOI:10.1016/j.optlastec.2015.09.005**.

[20] ASTM G32 (2010). *Standard Test Method for Cavitation Erosion Using Vibratory Apparatus.* ASTM International, West Conshohocken.

Strojniški vestnik - Journal of Mechanical Engineering 62(2016)3, 163-170
© 2016 Journal of Mechanical Engineering. All rights reserved.
DOI:10.5545/sv-jme.2015.2921 Original Scientific Paper
Received for review: 2015-07-31
Received revised form: 2015-11-03
Accepted for publication: 2016-01-07

Design of Lyapunov Based Nonlinear Position Control of Electrohydraulic Servo Systems

Edvard Detiček* – Mitja Kastrevc
University of Maribor, Faculty of Mechanical Engineering, Slovenia

This paper studies the nonlinear closed loop control of an electrohydraulic servo system. The control strategy is developed based on Lyapunov theory of nonlinear systems using integrator backstepping approach. Highly nonlinear nature of electrohydraulic servo system is well known. Main reasons for nonlinear and non-differentiable mathematical description of systems dynamics are the fluid compressibility, leakage flows, friction forces and nonlinear fluid flow through servo valve orifices. These nonlinear terms influence also the dynamic errors of the control system.

Two different nonlinear design procedures are employed feedback linearization and integrator backstepping. Backstepping is used here because it is a powerful and robust nonlinear strategy. These techniques are used for construction of nonlinear control algorithm. The effectiveness of it, to stabilize any operating point of the system is proved by computer simulation. The systems error dynamics significantly depends on tuning parameters of the controller. The wrong selection of these parameters may lead to saturation or chattering of control signals. All derived results are validated by computer simulation of a nonlinear mathematical model of the system. The results are also compared to these obtained with a conventional P controller to prove that classic linear controllers fail to achieve a good tracking of the desired output, especially, when the hydraulic actuator operates at the maximum load.

The research studies represented in the paper shows big potential of Lyapunov based nonlinear controller design procedures, to obtain desired control objectives.

Keywords: nonlinear control, Lyapunov methods, integrator backstepping, position control, electrohydraulic servo system, computer simulation

Highlights

- *The nonlinear mathematical model of electrohydraulic position servo system was considered.*
- *Simplifications of mathematical model according to specifications of real components.*
- *Lyapunov based position control is developed.*
- *The results of computer simulation compare the dynamic behavior obtained by conventional PID (P) controller and Lyapunov based nonlinear controller.*

0 INTRODUCTION

Electrohydraulic servo systems take important place in modern industrial automation. It has been used in many kinds of mechanizations, including robots, computer numerical control (CNC) press brakes, computer controlled testing machines, etc.

Electro hydraulic actuator system has become one of the most important actuators in the recent decades. It offers many advantages such as good capability in positioning, fast and smooth response characteristics and high power density. Due to its capability in positioning it has given a significant impact in modern equipment for position control applications [1] and [2]. The applications in position control can be found in production assembly lines, robotics, aircrafts and testing equipment [3] and [4]. However, excellent positioning in these applications requires an accurate electro hydraulic actuator. Therefore, the development of suitable controller which could reflect such characteristics is very significant, although the dynamics of electro hydraulic servo system is highly nonlinear [5] and [6].

In ordinary feedback systems the method of feedback linearization is used to eliminate nonlinearities. Feedback linearization employs changes of coordinates to transform a given nonlinear system into equivalent linear one. A major advantage of feedback linearization approach is related to the cancelations of systems nonlinear dynamics that are introduced in design process. On the other hand some kinds of nonlinearities can have positive effects on system stability, therefore their cancellation can lead to instability in the presence of modelling uncertainties. As a solution to this problem the integrator backstepping approached is proposed. The fundamental concept of backstepping method is introduced by Krstic et.al. in their book [7].

The approach focusing on the stabilization problem in stochastic nonlinear systems is developed in the extension of this book. The backstepping control method is also presented in [8] to [10] where

*Corr. Author's Address: University of Maribor, Faculty of Mechanical Engineering, Smetanova 17, Maribor, Slovenia, edvard.deticek@um.si

this technique is explained in detail for regulating and tracking problem.

There are numerous of applications in industry, where the backstepping approach was used to obtained successful control of electric machines, wind turbines, based power production, robotic production systems and flight trajectory control.

Integrator backstepping control method allows also finding a solution for optimal control problems [11], estimating parameters and adaptive control design, as well as, development of robust nonlinear controllers. The observer based backtepping technique has been designed for force control of electrohydraulic actuator system [12]. The developed control system combine backstepping observer with adaptive and sliding mode controller. Electrohydraulic active suspension control system is also designed by backstepping approach [13]. To obtained best value for its tuning parameters the paricle swarm optimization tool is proposed in [14].

It is proved that the technique improve the transient stability and damping presented in the system. The performance of backstepping controller also depends on its gains or controller parameters. In this paper, the controller is developed on the basis of simplified mathematical model, while the parameters are tuned manually to prevent the control signal chattering.

1 ANALYSIS AND MATHEMATICAL MODELLING OF THE ELECTROHYDRAULIC SERVO SYSTEM

A typical electrohydraulic positioning servo system consists of a hydraulic power supply e.g. constant pressure hydraulic pump with relief valve and accumulator, a flow control servo valve (SV), a hydraulic cylinder, a position sensor and an electronic controller unit (Fig. 1).

Before of closed loop controller design for electrohydraulic servo system, the analysis of the system dynamics is required, as well as, mathematical modelling and computer simulation of dynamic behaviour [15] and [16]. The complete mathematical model of the system is based on physical laws that expresses dynamic behaviour and are described through differential equations. However, this task is troublesome due to the multidisciplinary nature of the electrohydraulic system that requires electric, magnetic, mechanical and hydraulic knowledge. Meanwhile, the nonlinearities of this type of system, such as fluid nonlinear properties, nonlinear servovalve dynamics and flow rate characteristics, as well as, nonlinearities associated with hydraulic actuator by converting hydraulic power into mechanical power, increase a model complexity. The methodology in this work is that a theoretical model is presented first, where each individual component is expressed in a phenomenological description context e.-g. basic physical law.

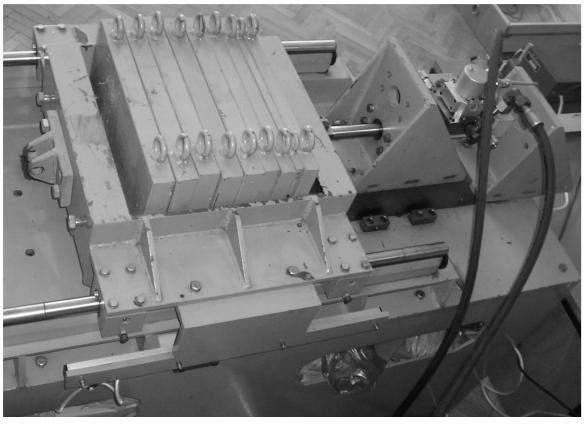

Fig. 1. *A one degree of freedom electro-hydraulic servo system with load*

1.1 Description of the SV Dynamics

Two stages SV consist of three main parts: the electrical torque motor, the hydraulic amplifier and the valve spool assembly (Fig. 2). In these SVs, the motor torque is commanded by an electrical current resulting in the flapper plate movement from its central position. The first stage is the so called flapper-nozzle system which allows the spool motion by adjusting the flapper via a low power electrical signal. The second stage relates the small spool motions ([μm]) into a large fluid flow through the spool ports.

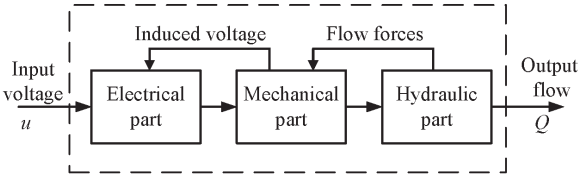

Fig. 2. *Two stage SV consist of three main parts: the electrical torque motor, the hydraulic amplifier and the valve spool assembly*

The flows in the SV concerns two parts: one is involved in the pilot stage and the other in the second stage.

In the first stage, the flapper deflects due to the torque generated by the torque motor. This force is the result of the current through the two coils fixed around the armature, which is connected to the flapper. As a

result of this displacement, the cross sections of the orifices associated with the nozzles change. Schematic of SV cross section is shown in Fig. 3.

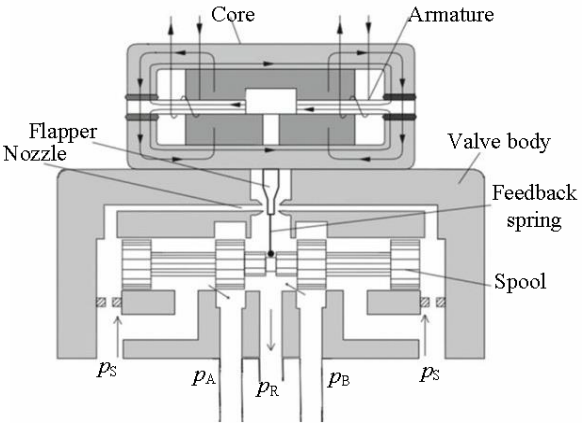

Fig. 3. *Schematic of SV;*
(p_S is supply pressure, p_R return pressure,
p_A pressure in chamber A, and p_B-pressure in chamber B)

Dynamic behaviour of valves involves a large number of parameters. An accurate analytical description would be time consuming and extremely difficult to validate for details. Therefore it is useful to use manufacturer's catalogue information which provides the well-known step responses and frequency responses for various sizes and types of valves. The inspection of step responses and frequency diagrams suggests an approximation of the SV by a second order model of the form [17].

$$\frac{1}{\omega_v^2}\ddot{x}_v + \frac{2\xi_v}{\omega_v}\dot{x}_v + x_v + f_{HS}\,\mathrm{sgn}\left(\dot{x}_v\right) = k_v \cdot u, \qquad (1)$$

where ω_v is a valve natural frequency, ξ_v damping coefficient, x_v valve spool displacement, f_{HS} takes into account the valve hysteresis and response sensitivity, k_v valve flow gain, and u valve input signal.

1.2 Hydraulic Actuator Dynamics

Hydraulic actuator (cylinder) converts hydraulic power into mechanical power. Hydraulic cylinder consists mainly of hollow cylindrical body and a piston. The chamber pressure dynamics is a well-known expression proposed by [5] and can be obtained by applying the conversation principle to each individual chamber, as follows:

$$\dot{p}_A = \frac{\beta_{Aeff}}{V_A}\left[Q_A - A_p\dot{x}_p + Q_{Li} - Q_{LeA}\right], \qquad (2)$$

$$\dot{p}_B = \frac{\beta_{Beff}}{V_B}\left[Q_B + \alpha A_p\dot{x}_p - Q_{Li} - Q_{LeB}\right]. \qquad (3)$$

The effective bulk modulus essentially depends on pressure, entrained air and mechanical compliance. The commonly used empirical equation for calculation of the effective bulk modulus for hydraulic cylinders is expressed as [17]:

$$\beta_{Aeff} = a_1\beta_{\max}\cdot\log\left(a_2\frac{p_A}{p_{\max}} + a_3\right), \qquad (4)$$

$$\beta_{Beff} = a_1\beta_{\max}\cdot\log\left(a_2\frac{p_B}{p_{\max}} + a_3\right), \qquad (5)$$

with the parameters $a_1=0.5$, $a_2=90$, $a_3=3$, $\beta_{\max}=18000$ [bar], $p_{\max}=280$ [bar].

The cylinder chambers volumes are given by:

$$V_A = V_{A0} + \left[A_p\left(x_0 + x_p\right)\right], \qquad (6)$$

$$V_B = V_{B0} + \left[\alpha A_p\left(x_0 - x_p\right)\right], \qquad (7)$$

where x_0 is initial piston position, x_p actual piston position and V_{A0}, V_{B0} are the initial chamber volumes which consist of an efficient part (the volume required to fill only the chambers) and inefficient part (volume of the pipelines between the valve and actuator) for the side A and B respectively. $A_A=A_p$ is a piston surface area and the $A_B=\alpha A_p$ rode side area where $\alpha=A_B/A_A$ is a ratio of cylinder bore area and the annulus effective area at the rod side.

Q_{Li} and Q_{Le} denote the internal leakage flow and the external leakage flow respectively. Leakage from one cylinder chamber to another, known as internal leakage flow, by assumption of laminal flow can be calculated:

$$Q_{Li} = k_L\left(p_B - p_A\right), \qquad (8)$$

where k_L is internal leakage flow coefficient, while the external leakage can be neglected.

The mechanical subsystem dynamics of the piston and the moving mass is described by dynamic equations:

$$m_t\cdot\ddot{x}_p + F_f\left(\dot{x}_p\right) = \left(p_A - \alpha\cdot p_B\right)A_p - F_{ext}, \qquad (9)$$

where m_t is total mass, F_f friction force and F_{ext} external load force.

The total mass m_t consists of the piston mass and the mass of hydraulic fluid in the cylinder chambers

and the pipelines. However, mass of fluid can usually be neglected with the piston mass.

An important part of above equation is a friction force. Friction is a complex natural phenomenon. It occurs at the physical interface of two surfaces in contact and tangential reaction between them. It can lead to tracking errors, limit cycle oscillations and undesirable stick-slip motion. Friction is commonly modelled as a discontinuous static mapping between the velocity and the friction force:

$$F_f(\dot{x}_p) = F_v(\dot{x}_p) + F_c(\dot{x}_p) + F_s(\dot{x}_p) =$$

$$= \sigma_{vf} \cdot \dot{x}_p + F_{co} \cdot sgn\left(\dot{x}_p\right) + sgn\left(\dot{x}_p\right) \cdot F_{so} \cdot e^{-\frac{|\dot{x}_p|}{c_s}}, \quad (10)$$

with σ_{vf} is the parameter for viscus friction, F_{co} static friction force, F_{so} Stribeck friction force, c_s Stribeck velocity. This friction force depends on the velocity sign and is restricted to viscous friction and Coloumb friction with Stribeck effect. Moreover, the friction force must be considered in order to obtain acceptable tracking accuracy.

Natural frequency can be also calculated based on the system design parameters. The natural frequency for the overall system equals the natural frequency of the hydro-mechanical part. Therefore, an electro-hydraulic control system natural frequency will be:

$$\omega_H = \sqrt{\frac{C_H}{m}}. \quad (11)$$

In order to calculate the natural frequency of hydraulic cylinder, the hydraulic cylinder stiffness must be found in advance. The total stiffness of differential cylinder is defined with equation **[16]**:

$$C_H = \frac{\beta_{Aeff} \cdot A_A^2}{V_A} + \frac{\beta_{Beff} \cdot A_B^2}{V_B}. \quad (12)$$

In case of synchronous cylinder (double rod of equal area) A_A is equal A_B. For performance calculation, only the minimum stiffness will be considered since it has the worst effect on the system dynamics.

1.3 Model Simplification

For the purpose of design of a closed loop controller the complete mathematical model of the system which consists of the hydraulic actuator dynamics, including the load and SV dynamics can be simplified according to manufacturers data of real system components. Usually a simplification can be obtain when the dynamic of the servo valve with control electronics is much higher than the dynamic of the cylinder and load.

For hydraulic system with $A_p = 6.4 \cdot 10^{-4}\,\mathrm{m}^2$, $V_t = 131.85 \cdot 10^{-6}\,\mathrm{m}^3$ and $m = 200\,\mathrm{kg}$ the minimum natural frequency is:

$$\omega_{H\min} = \sqrt{\frac{2\beta \cdot A_p^2}{m \cdot V_t}} = 215.866\left[\frac{\mathrm{rad}}{\mathrm{s}}\right] \Rightarrow 34.35\,[\mathrm{Hz}]. \quad (13)$$

Natural frequency can be read out, from the manufacturers data sheet for SV MOOG 769 **[18]** we can read out $f_{Hsv} = 325\mathrm{Hz}$.

Because of very high natural frequency of servo valve with comparison to hydraulic cylinder ($\omega_{Hsv} >> \omega_{Hmin}$), taking in to account also dynamic effect of manifold which decreases hydraulic natural frequency, the dynamic of SV can be neglected. The servo valve can be described only by static relationship between spool position and the valve current input. Moreover the combined assembly of servovalve and electronic amplifier can be described by the equation:

$$x_v = k_v \cdot u, \quad (14)$$

where k_v [mV^{-1}] is combined SV and electronic amplifier gain. Therefore the simplified system equations have the following form:

$$\begin{aligned}
&\dot{x}_p = v_p, \\
&\dot{v}_p = \frac{A_p}{m} p_L - \frac{F_{ext}}{m} - \\
&-\frac{1}{m}\left[\sigma_{vf} \cdot \dot{x}_p + F_{co} \cdot sgn\left(\dot{x}_p\right) + sgn\left(\dot{x}_p\right) \cdot F_{so} \cdot e^{-\frac{|\dot{x}_p|}{c_s}}\right], \\
&\dot{p}_L = \frac{4\beta}{V_t} \cdot C_d \cdot k_v \sqrt{\frac{p_s - sgn(u)\, p_L}{\rho}} \cdot u - \frac{4\beta}{V_t} \cdot \\
&\cdot A_p \cdot \dot{x}_p - \frac{4\beta}{V_t} \cdot k_L \cdot p_L.
\end{aligned} \quad (15)$$

where x_p is actual piston position, v_p piston velocity and p_L load pressure.

2 CONTROLLER DESIGN

For a spatial class of nonlinear dynamical systems, the backstepping control has emerged us successful control strategy. Some of nonlinear systems can be observed as a systems constructed from subsystems. The number of subsystems depends of dynamic model order. Because of this recursive structure, the designer can start the design process at the known-stable system and design,"back out", new controllers

that progressively stabilize each outer subsystem. The process is finished when the final external control is reached.

The mathematical description of nonlinear system in new set of coordinates allows us to use the backstepping approach to force it to behave like a linear one [7]. Backstepping has the availability to avoid cancellations of useful nonlinearities and pursue the objectives of stabilization and tracking rather than that of linearization method. Besides, backstepping approaches relaxes the matching conditions on perturbations which means that the perturbation doesn't have to appear in the equation that contains the input of the system. This controller can be used for tracking and regulation problem. For tracking problem, backstepping always use the error between the actual and desired input in order to start the design process.

The system state equations can be represented in "strict feedback form":

$$\begin{aligned}\dot{x}_1 &= x_2,\\ \dot{x}_2 &= a_1 x_3 - a_2 x_2 - a_3 sgn(x_2) - a_4,\\ \dot{x}_3 &= a_5\sqrt{p_s - sgn(u)x_3}\,u - a_6 x_2 - a_7 x_3,\end{aligned} \quad (16)$$

where $x_1 = x_p$, $x_2 = v_p$ and $x_3 = p_L$, with:

$$a_1 = \frac{A_p}{m}, \quad a_2 = \frac{\sigma_{vf}}{m}, \quad a_3 = \frac{F_{co}}{m}, \quad a_4 = \frac{F_{ext}}{m},$$
$$a_5 = \frac{4\beta}{V_t\sqrt{\rho}} \cdot C_d \cdot k_v, \quad a_6 = \frac{4\beta}{V_t} \cdot A_p \quad a_7 = \frac{4\beta}{V_t} \cdot k_L.$$

In the procedure of design a backstepping controller it is preferable to replace nonlinear terms with differentiable mathematical functions. An essential factor of its validity is the continuous dependence of its solutions on the data of the problem that can be stated by the Lipschitz inequality given by:

$$\|f(x) - f(y)\| \le L\|x - y\|. \quad (17)$$

To satisfy condition in Eq. (17) we estimated the "*sgn*" function with continuously differentiable function "*tanh = th*" (hyperbolic tangent) except in last equation.

$$\dot{x}_1 = x_2, \quad (18a)$$

$$\dot{x}_2 = a_1 x_3 - a_2 x_2 - a_3 th(\lambda x_2) - a_4, \quad (18b)$$

$$\dot{x}_3 = a_5 u\sqrt{p_s - sgn(u)x_3} - a_6 x_2 - a_7 x_3 \quad (18c)$$

where λ is free coefficient (λ=2)

The control objectives were to stabilize the plant and to track the given reference signal asymptotically. The detailed derivations of finding backstepping control input are covered in next three steps [9].

Step 1

We want the x_1 is position variable to track a reference signal, say, $r(t)$. So we have the first error variable:

$$z_1 = x_1 - r, \quad (19)$$

and its derivative:

$$\dot{z}_1 = \dot{x}_1 - \dot{r}, \quad (20)$$

where $r(t)$ is the reference input.

For equation (18a) we can define a virtual control α_1. Virtual state variable z_2 represents the difference between the actual and virtual control of (18a), i.e.

$$z_2 = x_2 - \alpha_1 \quad \rightarrow \quad x_2 = z_2 + \alpha_1. \quad (21)$$

Define a candidate control Lyapunov functional for this equation:

$$V_1 = \frac{\rho_1}{2} \cdot z_1^2. \quad (22)$$

The derivative of V yields:

$$\dot{V}_1 = \rho_1 \cdot \left[(x_1 - r) \cdot z_2 + (x_1 - r)(\alpha_1 - \dot{r})\right]. \quad (23)$$

Select a virtual control for the first order system:

$$\alpha_1 = \dot{r} - K_1 z_1 = -K_1 x_1 + K_1 r + \dot{r}, \quad (24)$$

where $K_1 > 0$. Hence, $\dot{V}$ can be rewritten as:

$$\dot{V}_1 = -\rho_1 K_1 z_1^2 + \rho_1 z_1 z_2. \quad (25)$$

Step 2

Define a second virtual state

$$z_3 = x_3 - \alpha_2 \quad \rightarrow \quad x_3 = z_3 + \alpha_2, \quad (26)$$

thus:

$$\dot{z}_2 = \dot{x}_2 - \dot{\alpha}_1. \quad (27)$$

Define a candidate control Lyapunov functional for this equation:

$$V_2 = V_1 + \frac{\rho_2}{2} \cdot z_2^2. \quad (28)$$

The derivative of V_2 is:

$$\dot{V}_2 = \dot{V}_1 + \rho_2 \cdot z_2 \cdot \dot{z}_2. \quad (29)$$

Select a virtual control for this system to remove any potentially undesired z_2, x_1 and x_2 terms:

$$\alpha_2 = \frac{1}{a_1}\left(a_2 x_2 + a_3 th(\lambda x_2) + a_4 + \dot{\alpha}_1 - \frac{\rho_1}{\rho_2} z_1 - \frac{K_2}{\rho_2} z_2 \right), \quad (30)$$

where $K_2 > 0$, therefore:

$$\dot{V}_2 = -K_1 \cdot \rho_1 \cdot z_1^2 - K_2 \cdot z_2^2 + \rho_2 \cdot a_1 \cdot z_2 \cdot z_3, \quad (31)$$

Step 3

Let's recall $z_3 = x_3 - \alpha_2$. The derivative of z_3 is:

$$\dot{z}_3 = \dot{x}_3 - \dot{\alpha}_2. \quad (32)$$

With augmentation of the initial control Lyapunov functional to reflect the presence of the new state variable:

$$V_3 = V_2 + \frac{\rho_3}{2} \cdot z_3. \quad (33)$$

The derivative yields:

$$\dot{V}_3 = \dot{V}_2 + \rho_3 \cdot z_3 \cdot \dot{z}_3. \quad (34)$$

Select an actual control for this system:

$$u = \frac{1}{\rho_3 a_5} \frac{1}{\sqrt{p_s - x_3}} \cdot$$
$$\cdot \left[-\rho_2 a_1 z_2 + \rho_3 a_6 x_2 + \rho_3 a_7 x_3 + \rho_3 \dot{\alpha}_2 - K_3 z_3 \right], \quad (35)$$

where $K_3 > 0$. Then we get:

$$\dot{V}_3 = -K_1 \cdot \rho_1 \cdot z_1^2 - K_2 \cdot z_2^2 - K_3 z_3^2, \quad (36)$$

where K_1, K_2, $K_3 > 0$. Note that Eq.(28) is the Lyapunov function of the system defined by Eqs.(18a) to (18c) and that the control law given by Eqs. (24), (30) and (35) renders its derivative negative semidefinite.

3 RESULTS AND DISCUSIONS

In order to verify the effectiveness of the proposed backstepping control algorithm, simulation experiments have been done on the electrohydraulic servo system. Main parameters of the system are given in Table1.

For position control systems dynamically aperiodic response is demanded. The final position accuracy is tested at small steps of reference value.

In Fig. 4 the comparison of systems dynamic response between P-controller and backstepping controller to 1mm desired position step is shown. The corresponding tracking errors are shown on Fig. 5. The system state variables are shown on Fig. 6, while corresponding virtual control variables and final real control of the backstepping controller are shown on Fig. 7.

Table 1. *Main parameters of the EHS system*

Par.	Value	Par.	Value
A_p	6.4·10–4 m2	m	200 kg
σ_{vf}	70 Ns/m	V_t	131.85·10–6 m3
F_{co}	19.62 N	β	1.5·109 Pa
F_{ext}	[N]	p_s	210 bar
k_L	3·10–13 m5/Ns	ρ	850 kg/m3
C_d	0.63	k_V	5.53·10–7 m2/V

In Fig. 8 the comparison of systems dynamic response to sinusoidal reference input is shown. The corresponding tracking errors are shown on Fig. 9. The system state variables are shown on Fig. 10,

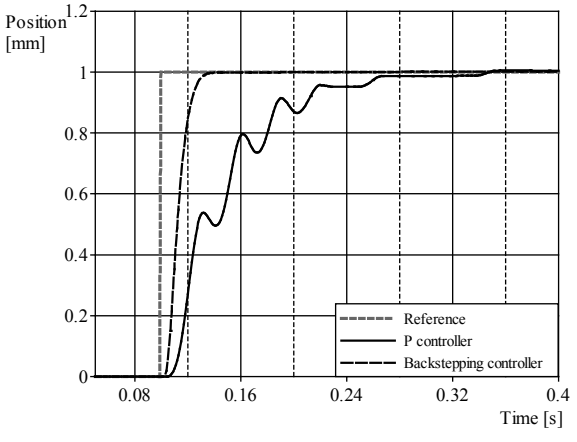

Fig. 4. *Simulation results of the system step response*

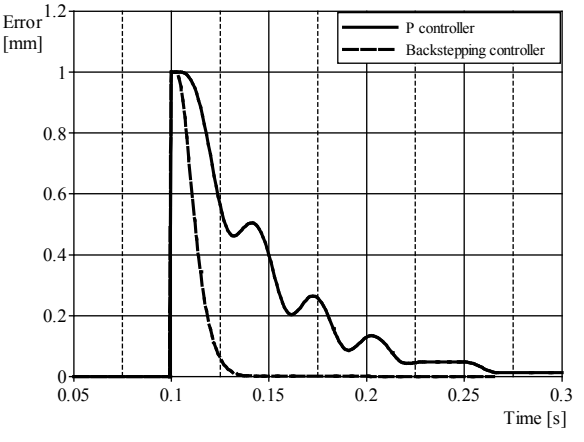

Fig. 5. *Tracking error of the system step response*

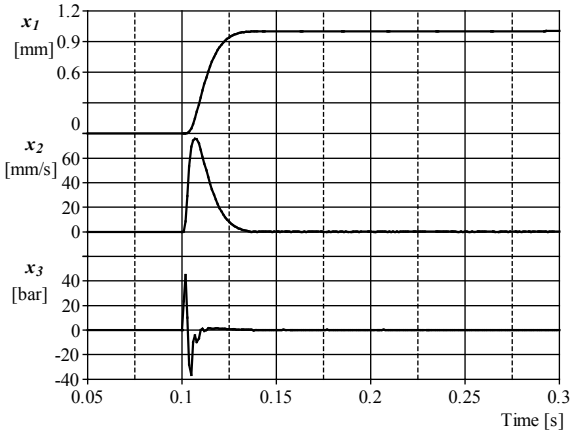

Fig. 6. *Dynamic behaviour of the systems variables by step response*

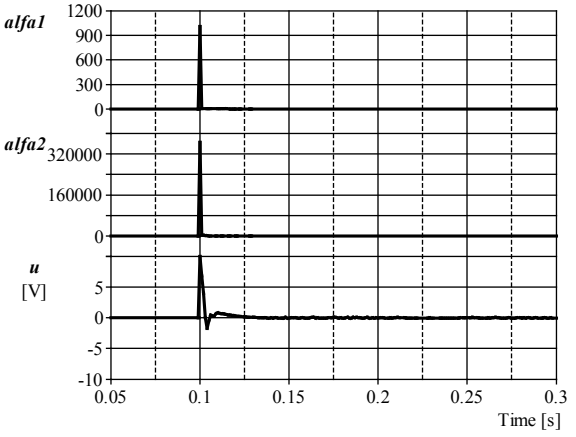

Fig. 7. *Virtual control variables and final real control variable of backstepping controller*

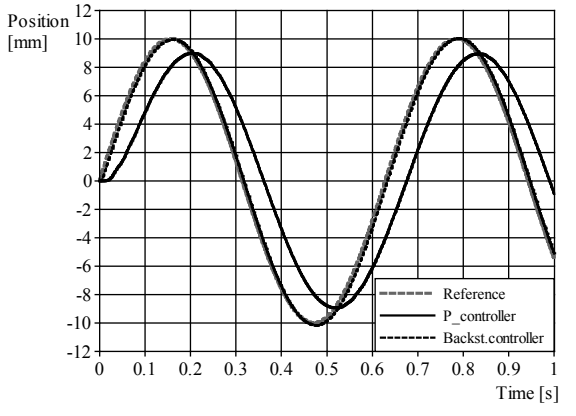

Fig. 8. *Simulation results of the system response on sinusoidal reference input*

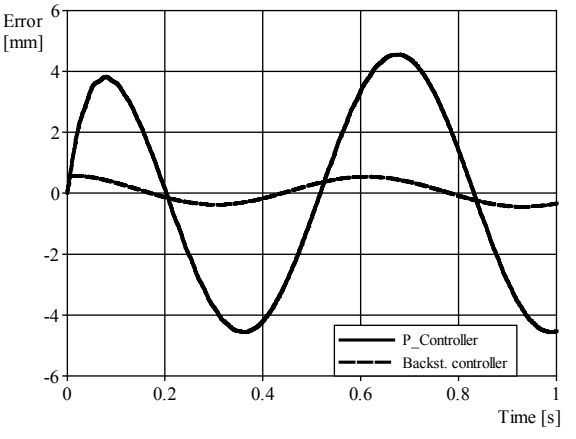

Fig. 9. *Tracking error of the system response on sinusoidal reference input*

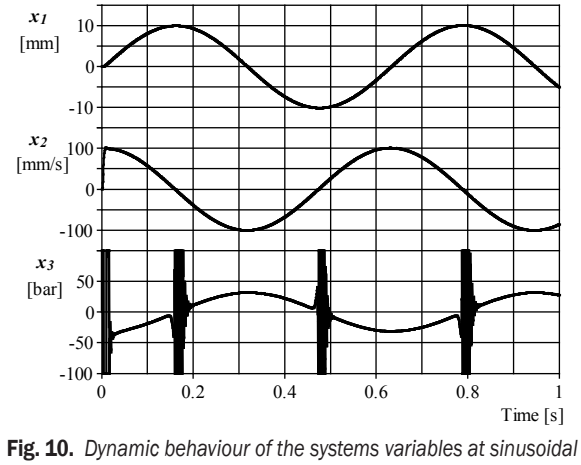

Fig. 10. *Dynamic behaviour of the systems variables at sinusoidal reference input*

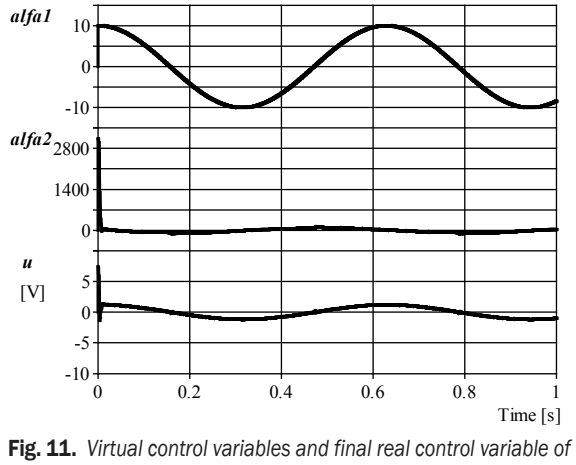

Fig. 11. *Virtual control variables and final real control variable of backstepping controller*

while corresponding virtual control variables and final real control of the backstepping controller are shown on Fig. 11.

The results are obtained with P-controller gain $K_P=2.3$, while the backstepping controller parameters are $K_1=50$, $K_2=600$, $K_3=600$, $\rho_1=6500$, $\rho_2=0.65$, $\rho_3=1$.

4 CONCLUSIONS

In this paper, a controller design procedure is presented in order to control the position of the electro-hydraulic servo system. Comprehensive investigation was carried out on the mathematical modelling and computer simulation of dynamic behaviour of whole system, based on real laboratory experimental data.

Because of very fast SV in combination with large moving mass and relatively long hydraulic cylinder, the mathematical model was reduced to third order, neglecting SV first stage dynamics. Such simplified mathematical model was used as a basis to design the closed loop controller. The developed control strategy is based on Lyapunov stability theory of nonlinear systems. We proposed a robust nonlinear controller, using integrator backstepping approach. The validity of the proposed new feedback law has been tested and compared with P-controller in various computer simulations. In all cases the nonlinear controller shows best tracking performance, with very small position tracking error. Excellent tracking capability of the proposed new controller is also recognized by sinusoidal reference input. Furthermore the tracking errors converge to zero quickly in contrast to the non-zero tracking error of the P-controller. The new controller also shows a certain measure of robustness to small parameter changes. Finally, the controller guaranties a prescribed transient performance and final tracking accuracy. Our future work will look towards the development of nonlinear adaptive controller which would be able to work in the presence of parametric uncertainties and environmental changes.

5 REFERENCES

[1] Khalil, H.K. (2009). Interactive analysis of closed loop electro-hydraulic control systems, *13th International Conference on Aerospace Scienties & Aviation Technology*, ASAT-13-HC-01.

[2] Kovari, A. (2015). Effect of Leakage i Electrohydraulic Servo Systems Based on Complex Nonlinear Mathematical Model and Experimental Results. *Acta Polytechnica Hungarica*, vol. 12, no. 3, p. 129-146, **DOI:10.12700/APH.12.3.2015.3.8**.

[3] Gubeljak, N., Predan, J., Senčič, B., Chapetti, M.D. (2014). Effect of residual stresses and inclusion size on fatigue resistance of parabolic steel springs. *Materials Testing*, vol. 56, no. 4, p. 312-317, **DOI:10.3139/120.110567**.

[4] Veg, E., Veg, A., Sinkovic, G., Andrejevic, R., Gubeljak, N. (2015). Design of coupled slider crank mechanism for orbiting motion, *International Journal of Simulation Modelling*, vol. 14, no. 2, p. 189-200, **DOI:10.2507/IJSIMM14(2)1.283**.

[5] Merritt, H.E. (1967). *Hydraulic Control Systems*. Wiley, NewYork.

[6] Lovrec, D., Tic, V., Tasner, T. (2015). Simulation-aided determination of an efficiency field as a basis for maximum efficiency controller design. *International Journal of Simulation Modelling*, vol. 14, no. 4, p. 669-682, **DOI:10.2507/IJSIMM10(3)3.184**.

[7] Kristic, M., Kanellakopouls, I., Kokotovic, P.V. (1995). *Nonlinear and Adaptive Control Design*, John Wiley and Sons, Hoboken.

[8] Khalil, H. K. (2002). *Nonlinear Systems*, 3rd ed., Prentice Hall, Upper Saddle River.

[9] Lee, S. J., Tsao, T.-C. (2002). Nonlinear backstepping control of an electrohydraulic material testing system, *Proceedings of the American Control Conference*, vol 6. p. 4852-4830, **DOI:10.1109/ACC.2002.1025422**.

[10] Ursu, I., Ursu, F., Popescu, F. (2006). Backstepping design for controlling electrohydraulic servos. *Journal of the Franklin Institute*, vol. 343, no. 1, p. 94-110, **DOI:10.1016/j.jfranklin.2005.09.003**.

[11] Bonchis, A., Corke, P.I., Rye, D.C., Ha, Q.P. (2001) Variable structure methods in hydraulic servo systems control. *Automatica*, vol.37, no. 4, p. 589–95, **DOI:10.1016/S0005-1098(00)00192-8**.

[12] Nakkarat, P., Kuntanapreeda, S. (2009). Observer-based backstepping force control of an electrohydraulic actuator. *Control Engineering Practice*, vol. 17, no. 8, p. 895-902, **DOI:10.1016/j.conengprac.2009.02.011**.

[13] Sun,W., Gao, H., Kaynak, O. (2013). Adaptive Backstepping Control for Active Suspension Systems With Hard Constraints, *IEEE/ASME Transactions on Mechatronics*, vol. 18, no. 3, p. 1072-1079, **DOI:10.1109/TMECH.2012.2204765**.

[14] Wonohadidjojo, D.M., Kothapalli, G., Hassan, M.Y. (2013). Position Control of Electro-hydraulic Actuator System Using Fuzzy Logic Controller Optimized by Particle Swarm Optimization. *International Journal of Automation and Computing*, vol. 10, no. 3, p.181-193, **DOI:10.1007/s11633-013-0711-3**.

[15] Lovrec, D., Kastrevc, M. (2011). Modelling and simulating a controlled press-brake suplay system. *International Journal of Simulation Modelling*, vol. 10, no. 3, p. 133-144, **DOI:10.2507/IJSIMM10(3)3.184**.

[16] Wright, H., Alleyne, A., Liu, R. (1997). On the stability and performance of two-state hydraulic servovalves. *Proceedings of the ASME Dynamic Systems and Control Division*, vol. 63, p. 215-222.

[17] Jelali, M., Kroll, A. (2003). *Hydraulic Servo-systems:modelling, identification and control*. Springer–Verlag, London, Berlin, Heidelberg, **DOI:10.1007/978-1-4471-0099-7**.

[18] *MOOG. Servovalves with Integrated Electronics D769 Series*. Rapport technique, MOOG Inc., *from http:/www.moog.com/literature/ICD/D769seriesvalves.pdf,* accessed on 2015-06-03.

Strojniški vestnik - Journal of Mechanical Engineering 62(2016)3, 171-178
© 2016 Journal of Mechanical Engineering. All rights reserved.
DOI:10.5545/sv-jme.2015.2901 Original Scientific Paper
Received for review: 2015-07-20
Received revised form: 2015-10-22
Accepted for publication: 2015-12-17

Analysis of the Effect of Process Parameters on Part Wall Thickness Variation in Conventional Metal Spinning of Cr-Mn Austenitic Stainless Steels

Peter Šugár[1] – Jana Šugárová[1] – Ján Petrovič[2]
[1] Slovak University of Technology, Faculty of Materials Science and Technology, Slovakia
[2] Eiben, Co. Ltd., Slovakia

Metal spinning is one of a number of flexible sheet forming processes which is a cost effective option for the production of parts with a very high strength to weight ratio. Although the wall thickness of the formed part in conventional spinning is generally considered to be nearly constant, a non uniform distribution of wall thickness is in fact observed. In this study, the wall thickness variation of a formed part made of Cr-Mn austenitic stainless steel was analysed. The thickness variation was measured using an optical 3D scanning method and the influence of mandrel speed, feed ratio and tool path profile (convex, concave and linear) on wall thickness variation was studied. A three-level full factorial design of the experiment and ANOVA (Analysis of Variance) were used. The results show that the maximal variation in wall thickness is observed in approximately half of the part wall height (thinning) and on the open end of the part (thickening). Feed ratio and roller path profile are statistically significant factors governing wall thickness variation. There was no obvious effect from the variation in mandrel speed on the thickness distribution.

Keywords: metal spinning, stainless steel, 3D optical scanning, wall thickness, ANOVA

Highlights

- *Experimental study of conventional metal spinning of Cr-Mn austenitic stainless steel part.*
- *Analysis of spun part wall thickness distribution by optical 3D scanning method.*
- *Quantifying the significance of mandrel speed, feed ratio and tool path profile on the wall thickness variation by analysis of variance (ANOVA).*
- *Identification of strong statistical significance of the tool path profile and feed ratio effect on wall thickness variation.*

0 INTRODUCTION

Conventional metal spinning is a technology based on the gradual shaping of a circular sheet over a mandrel through the action of a roller that produces localised pressure and moves axially over the outer surface of the sheet to produce a symmetrical product. This technology incorporates conventional spinning, shear spinning and tube spinning **[1]** and also a group of novel spinning processes, such as non-axisymmetrical spinning, non-circular cross-section spinning and tooth-shaped spinning **[2]** and **[3]**. Due to the development of numerically controlled lathes, spinning is becoming a cost effective option for both medium and high volume production of parts with a very high strength to weight ratio. Moreover, it is possible to spin components with tight geometrical tolerances and to achieve high-quality surface integrity **[4]** to **[6]**. The process has a wide variety of applications including parts for the automotive and aerospace industries, parts such as centrifuges, funnels, tanks, parts for medical and gastronomy equipment, as well as parts for musical instruments and pieces of art.

Wall thickness variation is a major defect found in parts made from sheet metals that influences the intensity of part defects and may cause part failure **[7]**. The wall thickness of the formed part in conventional spinning is, in general, considered to be nearly constant **[8]**. In fact, a non-uniform distribution of wall thickness is observed and therefore the spinning process must be optimized in order to produce components with a minimal variation in wall thickness. Based on experimental studies that have been carried out up to date, the spun part thickness distribution depends mainly on the number of tool passes, the offset of each pass from the other **[9]**, as well as the tool feed ratio **[10]**, shape of produced part **[11]**, roller noise radius **[4]** and **[12]**, friction **[13]** and first toolpass trajectory **[14]** to **[16]**. Low feed rates, large nose radius and multi-pass spinning are recommended to achieve uniform part wall thickness. High offset values tend to reduce wall thickness **[4]** and **[9]** to **[16]**.

A strong research effort has been made to study the effect of tool path profile on thickness variation. Kang et al. **[14]**, Liu et al. **[15]** and Hayama et al. **[16]** reported that the first pass in conventional spinning

*Corr. Author's Address: Slovak University of Technology in Bratislava, Faculty of Materials Science and Technology, Jana Bottu 25, 917 24 Trnava, Slovakia, peter.sugar@stuba.sk

played a decisive role in the final wall thickness variations. They also concluded that the linear tool path profile is less complicated and helps to reveal deformation characteristics. Concave paths are widely used, while convex paths are more suitable for producing convex cone shapes such as container heads.

Wang and Long [17] applied finite element analysis to study the effects of tool paths (linear, concave, convex, and combined curve) on the variation of wall thickness. They suggested that dominant in-plane tensile radial strains may be the main reason for wall thinning. The authors also reported that in a multi-pass conventional spinning process the wall thickness decreased after each forward roller pass (the roller feeds towards the rim of the workpiece) and there are almost no thickness changes during the backward passes. Using a concave roller path tends to greatly reduce wall thickness of the spun part, while using a convex roller path helps to keep the original wall thickness unchanged. A greater curvature of the concave path would result in more thinning of the wall thickness of the part.

Essa and Hartley [18] and [19] applied a finite element model for their study of the thickness distribution of aluminium cylindrical cups produced by conventional spinning. They found that by using a roller path profile of an involute curve in the first pass followed by a linear path profile in the second pass, minimum sheet thinning and a more uniform stress distribution could be obtained.

Polyblank and Alwood in their study [20] showed that toolpath design in spinning involves finding a balance between the need for deformation and the avoidance of failure by wrinkling and thinning. They suggest that in order to reduce thinning during the metal spinning process, a greater number of less aggressive passes should be used.

Although knowledge about the mechanics of spinning, which helps us to understand the final properties of the spun parts, has been developed by systematic investigation of the process using both experimental and theoretical techniques, the possible causes of thinning in part wall thickness during conventional spinning are still not fully understood and a knowledge gap between academic research outcomes and industry requirements exists.

The present paper analyses the results of experimental investigations concerning the wall thickness distribution of spun parts made of Cr-Ni austenitic stainless steel. The influence of mandrel speed, feed ratio and tool path profile on the spun parts wall thickness distribution was determined using statistical analysis.

1 EXPERIMENTAL SETUP AND METHODS

1.1 Experimental Samples and Set-Up

For the production of the experimental samples, whose shape and dimensions are shown in Fig. 1, a circular blank with an outer diameter of $D_0 = 200$ mm, prepared by AWJ machining technology, was used. The sheet used was made of austenitic stainless steel X5CrNi18-10 (DIN 1.4301). The basic mechanical properties that define the material plasticity (ultimate tensile strength (R_m), 0.2 % proof strength ($R_{p0.2}$) and elongation (A_{80})) of the experimental material is shown in Table 1.

Table 1. *Mechanical properties of the experimental material*

R_m [MPa]	$R_{p0.2}$ [MPa]	$R_{p0.2} / R_m$ [-]	A_{80} [%]
604	235	0.39	59.7

The experimental samples were produced on a DENN spinning machine, type Zenn-80 equipped with a Sinumeric 840-D CNC control unit (Fig. 2).

The mandrel made of Cr-Mo alloy steel (X155CrVMo12-1) with a hardness of 56 ± 2 HRC and a forming roller also made of Cr-Mo alloy steel (X155CrVMo12-1) with a hardness of 54 HRC was used.

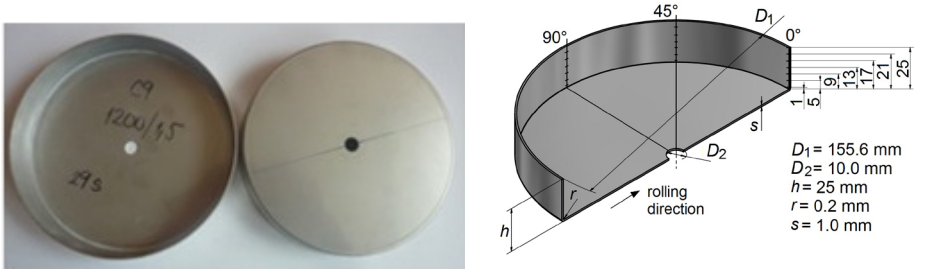

Fig. 1. *Experimental sample*

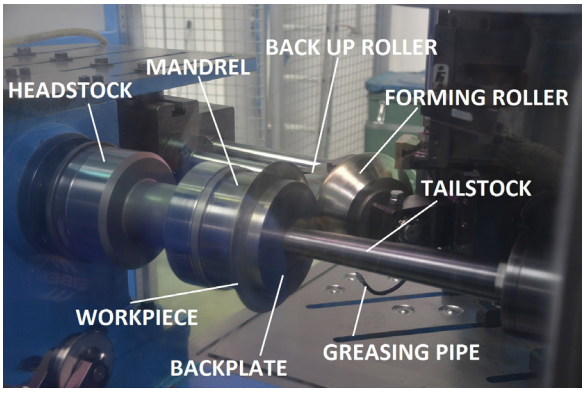

Fig. 2. *Experimental set up*

The roller geometrical parameters were: diameter 170 mm, radius R8 and the angle between the axis of the roller and the axis of the mandrel was 35° (Fig. 3).

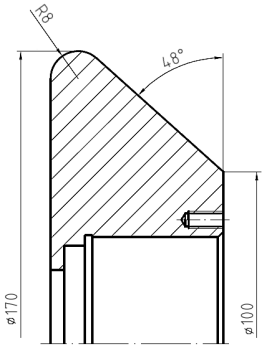

Fig. 3. *Roller geometry*

Three different mandrel speeds and three different levels of feed ratio (feed rate/mandrel speed) combined with the off-line designed linear, convex and concave roller path profiles were applied: nine movements towards the blank edge (forward passes) and one forward calibration pass. The detailed information about the first and last roller path of each path design is given in Fig. 4 and Table 2.

A review of experimental parameters and their levels is shown in Table 3. An experimental layout using full factorial design was used.

Table 2. *Polynomial interpolation of roller path profiles*

Convex	AD: $y = -0.006x^3 + 0.042x^2 - 0.701x + 99.637$
	EG: $y = -0.038x^2 + 1.904x + 58.02$
Concave	AE: $y = 0.004x^4 - 0.136x^3 + 1.846x^2 - 11.709x + 116.999$
	FI: $y = -0.0009x^3 + 0.006x^2 + 0.479x - 79.813$
Linear	AB: $y = -1.49x + 103.879$
	CD: $y = -0.257x + 74.402$

Table 3. *Process parameters and their levels*

Parameter	Level 1	Level 2	Level 3
Mandrel speed n [rpm]	400	800	1200
Feed ratio f [mm/rev]	0.5	1	1.5
Tool path profile tpp [-]	(1) concave	(2) linear	(3) convex

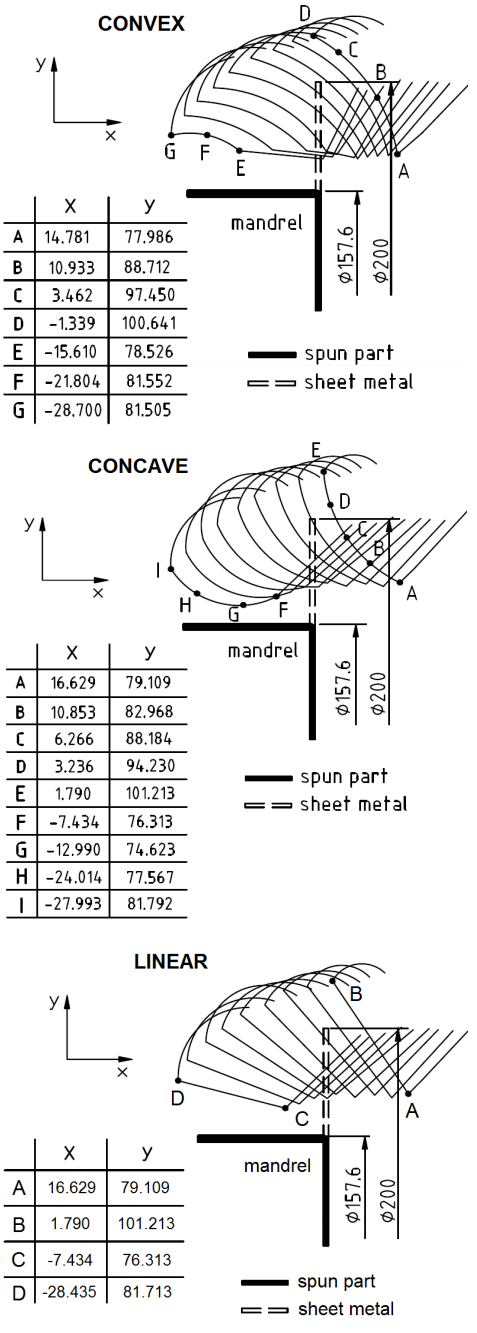

	X	y
A	14.781	77.986
B	10.933	88.712
C	3.462	97.450
D	-1.339	100.641
E	-15.610	78.526
F	-21.804	81.552
G	-28.700	81.505

	X	y
A	16.629	79.109
B	10.853	82.968
C	6.266	88.184
D	3.236	94.230
E	1.790	101.213
F	-7.434	76.313
G	-12.990	74.623
H	-24.014	77.567
I	-27.993	81.792

	X	y
A	16.629	79.109
B	1.790	101.213
C	-7.434	76.313
D	-28.435	81.713

Fig. 4. *Roller path profiles (Zero point [0;0]: intersection of mandrel axis with mandrel – workpiece interface plane)*

1.2 Method of Wall Thickness Measurement

For the experimental measurement of geometrical accuracy, a non-contact data capture method was used. The samples were digitized using the optical 3D system GOM ATOS II TripleScan SO MV 320 controlled by the software application GOM ATOS Professional v.7.4 [21] and [22]. The sample was scanned on a rotary table (10 scans rotated in 36° increments) from both the inside and outside. For a correct evaluation of the specimens with respect to the rolling direction of the blank, a special jig, inserted into a hole at the bottom of the part, was used. The part surface was sprayed with white powder to provide a matt surface, as reflected light negatively influences the measurement accuracy. Next, non-coded reference points with diameters of 3 mm were stuck on the part's surface. The cloud of captured points was polygonized to obtain a triangulated surface model. Then the digital model was exported into an .stl file. The digitized part was compared with the reference CAD model using the software GOM Inspect v.8. The shape deviation between the digitized and CAD (reference) model was visualized using colour deviation plots (Fig. 5) and the thickness of part wall was recorded [23].

Thickness variation in this study means any difference between the part wall thickness and the thickness of the original sheet metal.

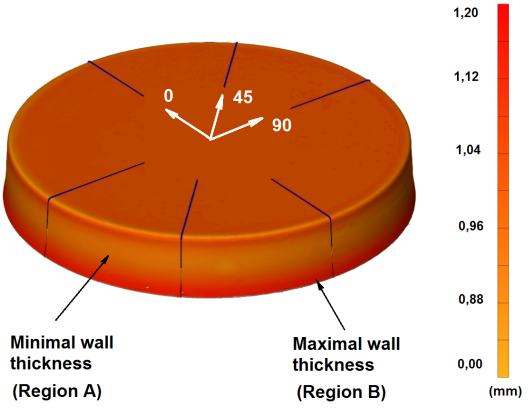

Fig. 5. *Digitized model of the formed part with color map of thickness deviations*

The thickness was measured in 7 places on the wall at distances of (1, 5, 9, 13, 17, 21 and 25) mm from the part bottom, as shown in Fig. 1. The wall thickness measurement was done in three directions related to the rolling direction of the sheet: 0°, 45° and 90°. Due to the negligible differences in the part wall thickness depending on the rolling direction of the sheet, the mean values of the thickness measured in three directions were taken into account for the final evaluation.

The 3D optical measurement method has been validated by the contact measurement method using a digital micrometer with pointed measuring faces and a resolution of 0.001 mm. The plot of deviations of measured data shows good agreement between the results of these measurements (Fig. 6).

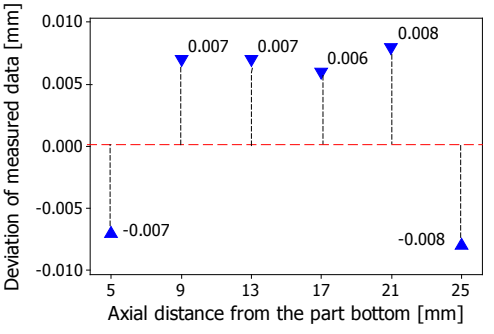

Fig. 6. *The deviations in measured data of wall thickness obtained using a non-contact method (3D optical scanning technology) and a contact method (micrometer)*

2 RESULTS AND DISCUSSION

The results of the experiments were analysed in order to estimate the contribution of individual parameters to part wall thickness variation. It was found that dependent on a combination of process parameters, the part wall thickness varies from 0.81 mm to 1.15 mm. As shown in Figs. 7 to 9, the maximal reduction in thickness was observed approximately half way up the part wall (Region A, situated at a distance of 13 mm from the part bottom) and the maximal increase in thickness was found at the open end of the formed part (Region B, situated at a distance of 25 mm from the part bottom).

In order to quantify the effects of the input factors studied and the interaction between them on wall thickness variation, an analysis of variance (ANOVA) using Minitab v. 17 software was performed. The Fisher's ratio (F-ratio), which is the ratio between the variance due to the effect of a factor and the variance due to an error term, was used to measure the significance of the factor at the desired significance level. If the F-test value is greater than the tabulated F-test value, the process parameter is considered significant.

The results of the ANOVA and F-test for part wall thickness measured in the area with maximal thinning (axial distance of 13 mm from the cup bottom) and

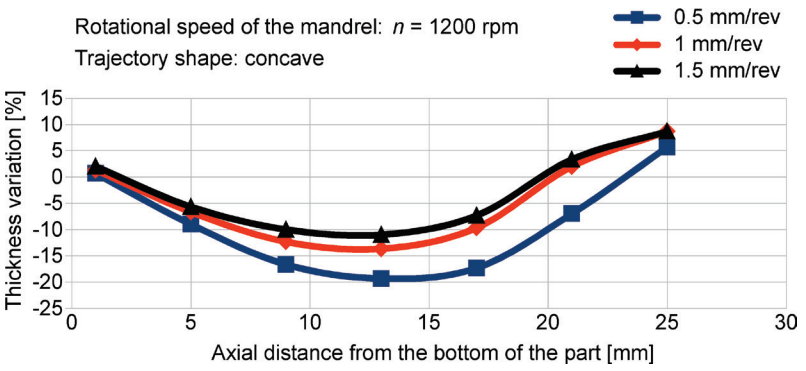

Fig. 7. *Effect of feed ratio on wall thickness variation (Expanded uncertainty of the measure U = 3 μm (k = 2; confidence level 95 %))*

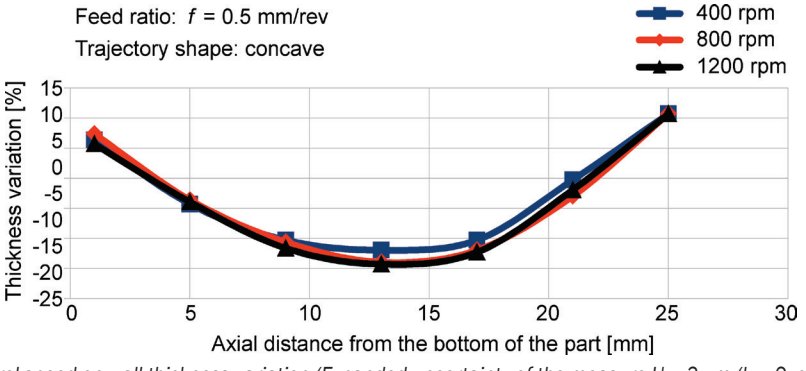

Fig. 8. *Effect of mandrel speed on wall thickness variation (Expanded uncertainty of the measure U = 3 μm (k = 2; confidence level 95 %))*

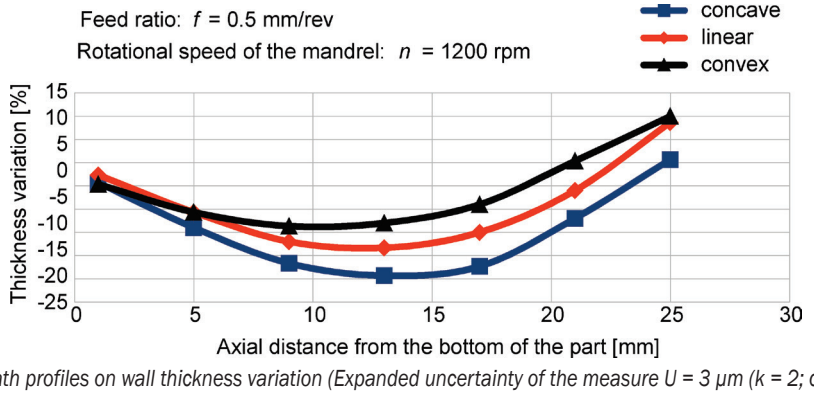

Fig. 9. *Effect of tool path profiles on wall thickness variation (Expanded uncertainty of the measure U = 3 μm (k = 2; confidence level 95 %))*

Table 3. *ANOVA for thickness variation at a distance of 13 mm from cup bottom*

Source	Sum of squares	DF	*F*-ratio	*p*-value
tpp	371.949	2	533.90	0.000
n	4.776	2	6.85	0.018
f	148.296	2	212.86	0.000
tpp×*n*	14.249	4	10.23	0.003
tpp×*f*	7.616	4	5.47	0.020
n×*f*	2.329	4	1.67	0.248
Error	2.787	8		
Total	552.000	26		

Tabulated *F*-test values at 95 % confidence level:
F (0.05; 2.8) = 4.46; F (0.05; 4.8) = 3.84; R^2_{adj} = 94.29 %

Table 4. *ANOVA for thickness variation at a distance of 25 mm from cup bottom*

Source	Sum of squares	DF	*F*-ratio	*p*-value
tpp	211.736	2	196.76	0.000
n	5.909	2	5.49	0.032
f	4.807	2	4.47	0.050
tpp×*n*	0.676	4	0.31	0.861
tpp×*f*	16.484	4	7.66	0.008
n×*f*	1.191	4	0.55	0.703
Error	4.304	8		
Total	245.107	26		

Tabulated F-test values at 95 % confidence level:
F (0.05; 2.8) = 4.46; F (0.05; 4.8) = 3.84; R^2_{adj} = 98.36 %

maximal thickening (axial distance of 25 mm from the cup bottom) are shown in Tables 3 and 4.

The results of ANOVA show that all of the main input factors have statistically significant (p-value: 0.01 to 0.05) or extremely significant (p-value < 0.0001) influence on wall thickness variation. The most significant effect of tool path profile on the wall thickness variation is clearly seen in both measured areas. The thinning of the part wall is also affected by feed rate, mandrel speed has minimal effect. The thickening of the part wall is also influenced not only by the tool path profile, but also by the mandrel speed and feed ratio.

The results further showed that for part wall thinning there is a significant interaction among the input parameters, which is the tool path profile – feed ratio (p-value: 0.01 to 0.05), and a very significant interaction among the input parameters, which is the tool path profile – mandrel speed (p-value: 0.001 to 0.01). For part wall thickening there is only one very significant interactive influence: the tool path profile – feed ratio.

The determination coefficients, R^2_{adj} = 94.29 % for part wall thinning and R^2_{adj} = 98.36 % for part wall thickening, demonstrate that the models are well fitted.

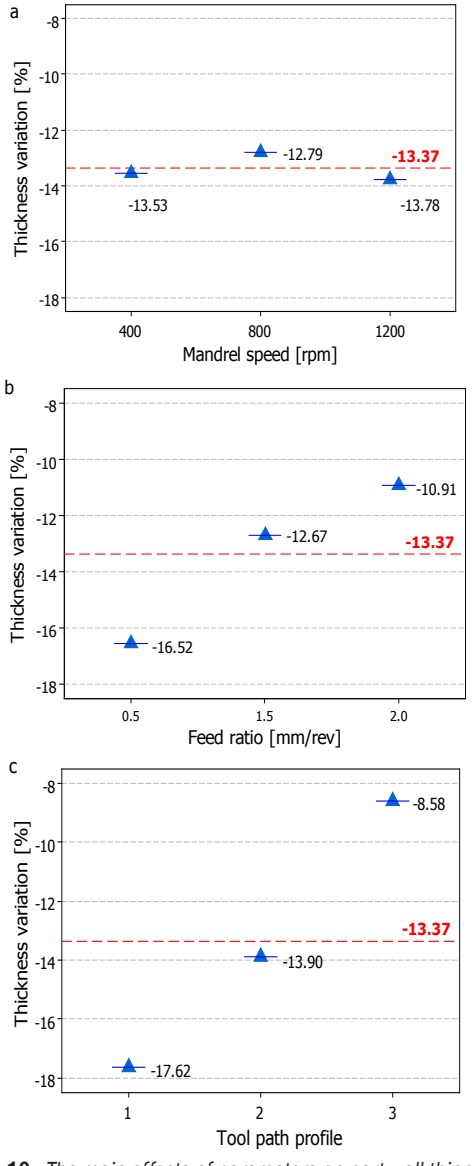

Fig. 10. *The main effects of parameters on part wall thinning: a) mandrel speed, b) feed ratio and c) tool path profile*

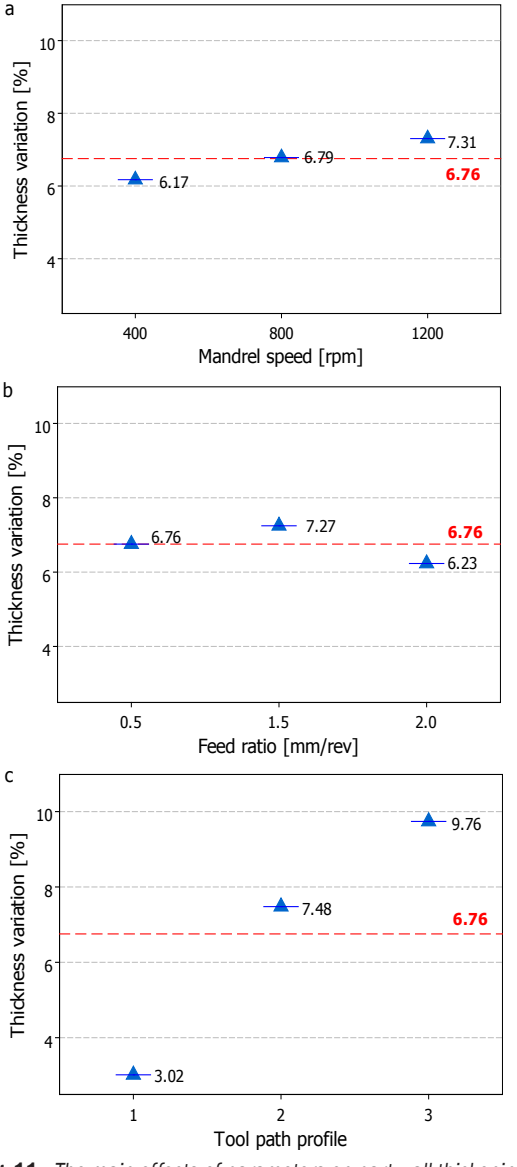

Fig. 11. *The main effects of parameters on part wall thickening: a) mandrel speed, b) feed ratio and c) tool path profile*

Fig. 10 shows graphs of the effects of the input parameters on the part wall thickness in the area of maximal thinning. It is clear that maximal thinning was observed when the concave tool path profile was used. The convex tool path profile leads to minimal thinning. The graphs also show that higher values of feed ratio decrease the part wall thinning. There is a specific situation in the case of mandrel speed. Minimal thinning is reached when the mandrel speed is set to a value of 800 min^{-1}. In both cases, when the mandrel speed value is higher or lower, a higher degree of part wall thinning is observed.

The effects of the main input parameters on part wall thickness in the area of maximal thickening are shown in Fig. 11. It can be seen that dominant thickening has been achieved for the convex tool path profile. The minimum value of thickening was recorded in the case where the concave tool path profile was applied. From the feed ratio point of view, minimal thickening was observed in the case where the maximal value of the feed ratio was applied and the maximal value of thickening was reported for the middle value of the feed ratio.

3 CONCLUSIONS

On the basis of the results obtained from this investigation and the statistical analysis, the following conclusions can be drawn:

1. The study confirms that 3D optical scanning technology can be useful in the evaluation of sheet metal parts thickness variation.
2. Among all the process parameters studied, the tool path profile is statistically the most significant factor and should be accurately controlled.
3. The concave tool path profile leads to a significant wall thickness reduction in Region A, but this roller trajectory gives minimal wall thickening on the open end of the part – Region B, which is accompanied by the higher height of the part. Much higher tensile radial strains are produced if a concave roller path is applied and this is believed to be the main reason for intensive wall thinning.
4. It is clear that a high feed ratio helps to minimise wall thickness variations. It yields minimal thinning in Region A and minimal thickening in Region B. A lower feed ratio means that the tool acts on the workpiece over more revolutions, which in turn leads to higher shearing effects, an intensive flow of material to the open end of the part and an appreciable thinning of the wall.
5. The finding related to the tool path profile and feed ratio influence on wall thickness variation agrees with the results of other authors who have studied this problem experimentally and by applying FE analysis for other types of spun part materials (mild steel, aluminium) **[12]**, **[14]**, **[17]** and **[24]**.
6. The influence of mandrel speed on wall thickness variation in both regions of the part wall is only minimal. The findings can be expressed thus: mandrel speed has negligible influence on axial and radial force components **[10]**, therefore radial and thickness strain is minimal.
7. For minimal variation in spun part wall thickness it is recommended to apply a convex tool path in combination with higher values of the feed ratio.

4 ACKNOWLEDGEMENTS

The authors wish to acknowledge the financial support provided by the Ministry of Education, Science, Research and Sport of the Slovak Republic project VEGA 1/0669/15 and the research project Manunet: FormTool MANUNET-2014-11283. The authors also wish to thank MSc. E. Eiben and MSc. G. Eiben of Eiben Co. Ltd. for their technical assistance.

5 REFERENCES

[1] Music, O., Allwood, J.M., Kawai, K. (2010). A review of the mechanics of metal spinning. *Journal of Materials Processing Technology*, vol. 210, no. 1, p. 3-23, **DOI:10.1016/j.jmatprotec.2009.08.021**.

[2] Xia, Q., Xiao, G., Long, H., Cheng, X., Sheng, X. (2014). A review of process advancement of novel metal spinning. *International Journal of Machine Tools and Manufacture*, vol. 85, p. 100-121, **DOI:10.1016/j.ijmachtools.2014.05.005**.

[3] Härtel, S., Laue, R. (2016). An optimization approach in non-circular spinning. *Journal of Materials Processing Technology*, vol. 229, p. 417-430, **DOI:10.1016/j.matprotec.2015.09.003**.

[4] Wong, C.C., Dean, T.A., Lin, J. (2003). A review of spinning, shear forming and flow forming processes. *International Journal of Machine Tools and Manufacture*, vol. 43, no. 14, p. 1419-1435, **DOI:10.1016/S0890-6955(03)00172-X**.

[5] Tschätsch, H. (2005). *Metal Forming Practise*. Springer, Heidelberg.

[6] Härtel, S., Awiszus, B. (2014). New processing technologies of incremental sheet metal forming. *Procedia Engineering*, vol. 81, p. 2311-2317, **DOI:10.1016/j.proeng.2014.10.326**.

[7] Brabie, G., Chirita, B., Albut, A. (2015) Minimization of sheet thickness variation and other defects of mini drawn parts using a blank holder plate made from concentric rings. *Precision Engineering*, vol. 42, p. 311–320, **DOI:10.1016/j.precisioneng.2015.03.011**.

[8] Quigley, E., Monaghan, J. (2000). Metal forming: an analysis of spinning processes. *Journal of Materials Processing Technology*, vol. 103, no. 1, p. 114-119, **DOI:10.1016/S0924-0136(00)00394-0**.

[9] Kawai, K., Hayama, M. (1987). Roller pass programming in conventional spinning by NC spinning machine. *Advanced Technology of Plasticity*, vol. 2, p. 711-718, **DOI:10.1007/978-3-662-11046-1_4**.

[10] Wang, L., Long, H., Ashley, D., Roberts, M., White, P. (2011). Effects of the roller feed ratio on wrinkling failure in conventional spinning of a cylindrical cup. *Journal of Engineering Manufacture*, vol. 225, no. 11, p. 1991-2006, **DOI:10.1177/0954405410396024**.

[11] Sugar, P., Šugárová, J., Morovič, L., Zemko, P. (2012). Analysis of dimensional accuracy of spun parts by Taguchi approach. *Applied Mechanics and Materials*, vol. 217-219, p. 2423-2426, **DOI:10.4028/www.scientific.net/AMM.217-219.2423**.

[12] El-Khabeery, M.M., Fattouh, M. El-Sheikh, M.N., Hamed, O.A. (1991). On the conventional simple spinning of cylindrical aluminium cups. *International Journal of Machine Tool and Manufacture*, vol. 31, no. 2, p. 203-219, **DOI:10.1016/0890-6955(91)90005-N**.

[13] Gao, C.Y., Fang, Y.T. (2005) Investigation on the factors influencing the thickness distribution of superplastic-formed components. *Journal of Zhejiang University, Science A*, vol. 6, no. 7, p. 711-715, **DOI:10.1631/jzus.2005.A0711**.

[14] Kang, D.-C., Gao, X.-C., Meng, X.-F., Wang, Z.-H. (1999). Study on the deformation mode of conventional spinning of plates. *Journal of Materials Processing Technology*, vol. 91, no. 1-3, p. 226-230, **DOI:10.1016/S0924-0136(98)00447-6**.

[15] Liu, J.H., Yang, H., Li, Y.Q. (2002). A study of the stress and strain distributions of first-pass conventional spinning under different roller-traces. *Journal of Materials Processing Technology*, vol. 129, no. 1-3, p. 326-329, **DOI:10.1016/S0924-0136(02)00682-9**.

[16] Hayama, M., Kudo, H., Shinodura, T. (1970). Study of the pass schedule in conventional simple spinnning. *Bulletin of Japan Society of Mechanical Engineering*, vol. 13, no. 65, p. 1358-1365, **DOI:10.1299/jsme1958.13.1358**.

[17] Wang, L., Long, H. (2011). A study of effects of roller path profiles on tool forces and part wall thickness variation in conventional metal spinning. *Journal of Materials Processing Technology*, vol. 211, no. 12, p. 2140-2151, **DOI:10.1016/j.jmatprotec.2011.07.013**.

[18] Essa, K., Hartley, P. (2009) Numerical investigation on the effect of roller-trace in dual pass cup spinning. *Journal for Technology of Plasticity*, vol. 34, no. 1-2, p. 15-25.

[19] Essa, K., Hartley, P. (2010). Optimization of conventional spinning process parameters by means of numerical simulation and statistical analysis. *Journal of Engineering Manufacture*, vol. 224, no. 11, p. 1691-1705, **DOI:10.1243/09544054JEM1786**.

[20] Polyblank, J.A., Allwood, J.M. (2015) Parametric toolpath design in metal spinning. *CIRP Annals - Manufacturing Technology*, vol. 64, no. 1, p. 301-304, **DOI:10.1016/j.cirp.2015.04.077**.

[21] *ATOS II Rev. 02: User Manual – Hardware*. (2010). GOM GmbH.

[22] Brajlih, T. Tasic, T., Drstvensek, I., Valentan, B. Hadzistevic, M., Pogacar, V., Balic, J., Acko, B. (2011). Possibilities of using three-dimensional optical scanning in complex geometrical inspection. *Strojniški vestnik - Journal of Mechanical Engineering*, vol. 57, no. 11, p. 826-833, **DOI:10.5545/sv-jme.2010.152**.

[23] Šugár, P., Šugárová, J. and Morovič, L. (2008) Application of 3D optical scanning for the shape accuracy analysis of machine parts produces by multi-pass metal spinning. *Annals of DAAAM for 2008 & Proceedings of the 19th International DAAAM Symposium; Intelligent Manufacturing & Automation: Focus on Next Generation of Intelligent Sytems and Solutions*, p. 1331-1332.

[24] Runge, M. (1994). *Spinning and Flow Forming*. (D. H. Pollitt, Trans), Leifield GmbH.

Strojniški vestnik - Journal of Mechanical Engineering 62(2016)3, 179-186
© 2016 Journal of Mechanical Engineering. All rights reserved.
DOI:10.5545/sv-jme.2015.2995 Original Scientific Paper
Received for review: 2015-09-03
Received revised form: 2016-01-11
Accepted for publication: 2016-01-21

Mineral Wool Primary Layer Formation in Collecting Chamber

Benjamin Bizjan* – Marko Peternelj – Branko Širok
University of Ljubljana, Faculty of Mechanical Engineering, Slovenia

The process of the mineral wool primary layer formation was investigated experimentally on a model spinning machine with sucrose as a working medium. The fibers were pneumatically transported from the spinner rotor to the accumulation grid with the aid of the blow-away and the suction airflow. The fiber primary layer formed on the accumulation grid was visualized by a camera for several different operating regimes. Acquired images were post-processed to determine the light absorption in the primary layer, which was then used to calculate the bulk density and the surface density of the layer. Based on the measured process quantities, we were able to form multiple regression models with a relatively good correlation to the experimental data. The models as well as the qualitative image analysis show a significant effect of spinner rotor rotational speed, pneumatic transport velocity and fiber deposit mass on primary layer bulk density and spatial distribution of fibers.

Keywords: mineral wool, fiber, primary layer, spinning machine, collecting chamber, pneumatic transport

Highlights

- *Mineral wool primary layer formation was modeled experimentally using molten sucrose.*
- *Light-absorption visualization approach was used to measure the primary layer density and structure.*
- *Primary layer structure is significantly affected by the spinner rotational speed, blow-away and suction flow velocity, and the mass of accumulated fibers.*
- *Multiple regression models for the primary layer density and its standard deviation are in a good agreement with the measurements.*

0 INTRODUCTION

Mineral wool is a fibrous material commonly used for thermal and acoustic insulation and can be divided into subtypes such as the rock wool and the glass wool. Mineral wool production process is highly complex, consisting of several different production phases. Sufficient understanding and control of each phase is required in order to optimize the properties (e.g. thermal conductivity, homogeneity and mechanical properties) and production costs of the end products.

Production phases which most significantly affect the mineral wool quality are the melt fiberization on the spinning machine, fiber pneumatic transport and primary layer formation in the collecting chamber [1]. Two most commonly used spinner geometries are solid spinning wheels, used mainly for rock wool production, and hollow perforated rotors, used for glass wool production. The melt fiberization process was a subject of several experimental and numerical studies for both solid wheel spinners (Czygany et al. [2], Vad and Morlin [3], Zhao et al. [4]) and perforated rotors (Panda et al. [5], Mukundan and Panda [6], Marheineke and Wegener [7], Marheineke et al. [8], Qin et al. [9] and [10], Kraševec et al. [11]).

Fiber formation phase is followed by pneumatic transport of fibers in the blow-away flow to the collecting chamber where a primary layer of mineral wool is formed [1]. A good quality primary layer is defined by a low degree of spatial fluctuations in thickness and density of the fiber deposit, and is very important for achieving optimal insulation and mechanical properties of the end products. Due to the high complexity and multiphase nature of the flow, experimental investigation of the primary layer formation is difficult and mostly limited to the measurement of aerodynamic characteristics and flow visualization.

The transport of fibers in an axial airflow was modeled numerically by Lin et al. [12] and experimentally by Capone et al. [13] and Qi et al. [14]. In all of these studies, fibers had a relatively low aspect ratio (i.e. length to diameter ratio) and were treated as rigid bodies. On the other hand, mineral wool fibers typically have aspect ratios in excess of 1000 [1], leading to complex 3D flows with mutual intertwining and breakage of fibers. Consequently, the spatial structure of the fiber primary layer deposited on the accumulation grid may show significant inhomogeneities. Also, the newly formed primary layer can be damaged (torn apart and moved) by the flow of the blow-away air onto the accumulation grid. Širok et al. [1] showed that a reduction in air velocity extremes and gradients on the accumulation grid improves the quality of the mineral wool primary layer as the tearing and redistribution of the layer is largely reduced. The measures proposed so far to improve the velocity distribution include the addition of centrifugal

*Corr. Author's Address: University of Ljubljana, Faculty of Mechanical Engineering, Aškerčeva 6, 1000 Ljubljana, Slovenia, benjamin.bizjan@fs.uni-lj.si

rotors to the spinner wheels and modifications to the collecting chamber geometry [1]. However, further optimization and efficient real-time control of the primary layer formation require an accurate model of the process. Due to the process complexity and dependence on many operating parameters, only integral-level models were formed so far [1], proving only partly successful for this purpose.

To overcome the complexity of the industrial mineral wool production environment and the limited range in which the operating parameters can be varied, we have developed a model spinning machine similar to the glass wool spinners. The primary layer was analyzed by a visualization method, and its quality was characterized by multiple regression models.

This paper is organized as follows. The Methods section presents the theoretical background of the mineral wool primary layer formation and the layer visualization method used in our experiments. In the Experimental section, the model spinning machine and the corresponding measurement setup will be introduced whereas the Discussion section will present qualitative and quantitative results of visualization image analysis.

1 THEORETICAL BACKGROUND

The primary layer formation process is an important part of the mineral wool production line (see Fig. 1 for an example of a rock wool production line).

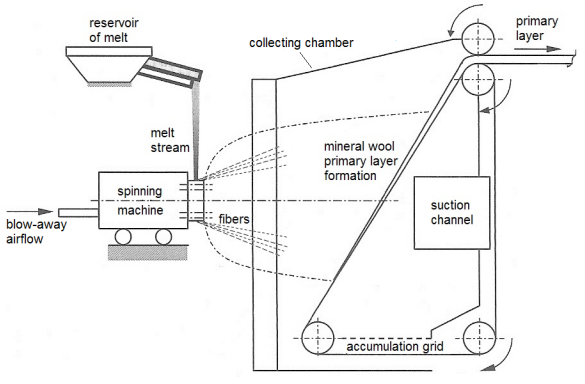

Fig. 1. *Rock wool production line between the melting furnace and the primary layer formation zone*

Mineral melt is prepared in the melting furnace from which it first enters the melt reservoir and is then supplied to the spinning machine in form of a free falling melt stream. In a rock wool production line, the melt typically impinges on a mantle surface of one or more spinning wheels, forming a film which continuously disintegrates into liquid ligaments. In manufacturing of glass wool, the fiberization process is different as the melt stream flows inside a spinning perforated rotor, forming a film on its internal mantle surface. Under the action of centrifugal force, melt film is then extruded through the perforations to form ligaments. Nevertheless, the phase following the ligament formation is similar for both spinner designs. Shortly after formation, melt ligaments solidify to fibers and are impregnated by the binder liquid. The fibers then enter the coaxial blow-away airflow (also known as the primary flow) and detach from the spinning machine, forming complex multiphase flow structures. The blow-away flow with fibers enters the collecting chamber while its velocity is reduced from an initial magnitude in excess of 100 m/s to below 10 m/s. Apart from the blow-away flow, the suction flow (also known as the secondary flow) is also present in the collecting chamber to allow the fibers to settle on the accumulation grid and thus form the primary layer. The layer is then compacted by several mechanical processes and is sent to the curing chamber where binder polymerization occurs.

The exact mechanism of the primary layer formation, including the fiber pneumatic transport, breakage and settling on the accumulation grid, is still largely unknown due its complexity and difficulty in observation on smaller length scales. While the primary layer quality control on industrial production lines is still mostly manual [1], there have been several attempts to quantitatively characterize the primary layer quality for the purpose of process automation. The most commonly used measurement method is the camera visualization of the mineral wool primary layer. A sample primary layer image is shown in Fig. 2. A good quality primary layer is characterized by a homogeneous structure of the fiber deposit (Fig. 2a) whereas an inhomogeneous structure with large variations in thickness and density indicates a poor quality of the primary layer.

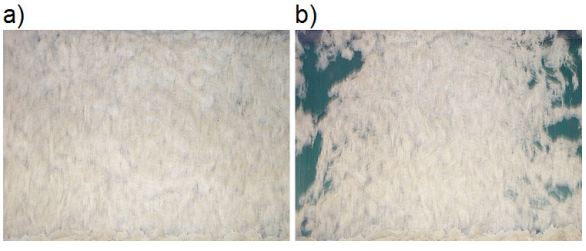

Fig. 2. *Primary layer on the accumulation grid; a) homogeneous structure; b) inhomogeneous structure*

Apart from the qualitative analysis, quantitative formulations based on the image gray level can

be used to analyze the homogeneity and texture of visualization images. Blagojević et al. [15] used a multiple regression model to predict the primary layer homogeneity. The same kind of visualization setup was also used by Bajcar et al. [16] and was followed by a computational fluid dynamics (CFD) analysis of the problem, confirming a significant effect of the local aerodynamic characteristics on the primary layer formation. Apart from the camera visualization, another possible method of primary layer structure analysis is by X-ray scanning, which is used mostly in the glass wool industry [11] and [17], although very little research work has been published so far. The method is based on radiation absorption and allows for the measurement of local primary layer densities, unlike the visualization method used in references [15] and [16], which can only provide information about the layer surface dynamics. To overcome the technical and confidentiality constraints of the industrial environment, a model study using the light absorption method is viable.

Based on the overview of the available literature, the area density μ and the bulk density ρ were determined to be the most representative primary layer properties in our experiments. To measure μ and ρ, a measurement setup with a visible light camera and lighting source was used so that the fibers were illuminated from behind. Similarly to the X-ray measurement method [11] and [17], which is impractical for small-scale lab experiments, the calculations of μ and ρ were performed based on the measured light absorption ratio I/I_0 (Fig. 3).

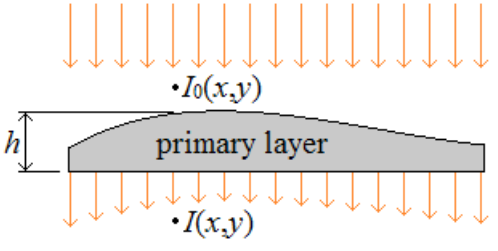

Fig. 3. *Light absorption over the primary layer*

Local primary layer thickness h (Eq. (2)) at position (x,y) can be obtained from the Beer-Lambert absorption law (Eq. (1)).

$$I = I_0 \exp(-\alpha h), \tag{1}$$

$$h = -\frac{1}{\alpha}\ln\left(\frac{I}{I_0}\right). \tag{2}$$

In the next step, the total volume V of the primary layer can be calculated by surface integration of h; Eq. (3).

$$V = \oint_A h dA. \tag{3}$$

For a known primary layer mass m (determined by weighing or other methods), the mean bulk density of the layer ρ can now be calculated as:

$$\rho = \frac{m}{V}. \tag{4}$$

Another characteristic primary layer property is the local area density μ and its normalized standard deviation $\sigma_{\mu n}$:

$$\mu = h\rho, \tag{5}$$

$$\sigma_{\mu n} = \frac{\sigma_\mu}{\overline{\mu}} = \frac{\sigma_\mu}{m/A}. \tag{6}$$

Alternately, the area density can be calculated directly from the Beer-Lambert law using the mass attenuation coefficient α_m (Eq. (7)). However, α_m is significantly more difficult to measure than α, making such calculation approach impractical unless α_m is already known.

$$\mu = \frac{\ln(I_0/I)}{\alpha_m}. \tag{7}$$

Note that listed calculation procedures assume a stationary accumulation grid. In the case of a moving grid, mass and volume would be replaced with their temporal derivatives (i.e. flows).

2 EXPERIMENTAL WORK

Experiments were conducted on a model spinning machine with a hollow perforated rotor and a vertical collecting chamber (Fig. 4a). The spinning machine used was basically a modified version of a cotton candy machine The Breeze 3030EX [18]. The rotor with 70 mm radius (Fig. 4b) had an integrated heater and was supplied with crystalline sucrose prior to each experiment. During the spinner operation, sucrose was melted by the heater at a rate of approximately 0.75 g/s while the rotor rotational speed was regulated by a single-phase variable frequency drive (VFD) in a range between 40 Hz and 50 Hz. Coaxial blow-away airflow was supplied through 45 circular nozzles (1 mm diameter, 5 mm length) evenly distributed around the supply ring on a radius of 80 mm. The blow-away flow was regulated by a valve so that the overpressure in the supply ring Δp was between 0 kPa and 50 kPa.

The spinning machine was placed inside a vertical collecting chamber with a circular cross section (0.63

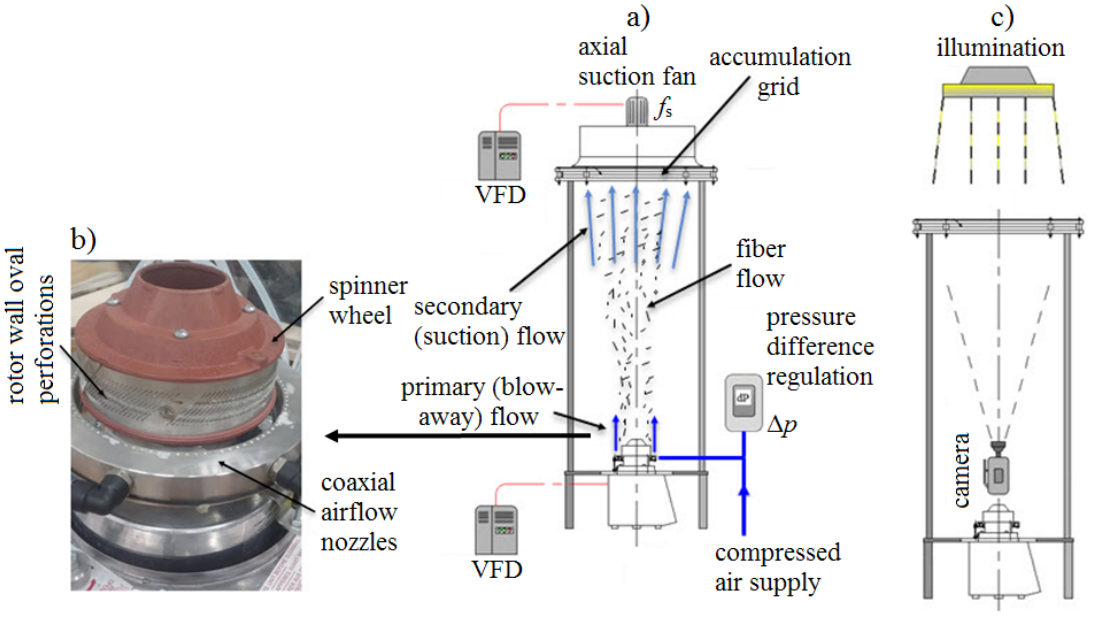

Fig. 4. *Experimental setup; a) spinner operation; b) spinner head (detail); c) primary layer visualization*

m in diameter) and a transparent wall. Secondary (i.e. suction) airflow was generated by a 7-blade axial fan powered by a three-phase VFD. The fan was placed on top of the collecting chamber immediately after the horizontal accumulation grid. VFD power supply frequency was varied between 0 Hz and 40 Hz, which resulted in fan rotational speeds between 0 Hz and 18.4 Hz.

About 40 seconds after the start of the spinner and air supply operation, fibers started to appear on the spinner rotor and were blown to the collecting chamber. After additional 10 s to 30 s, the heater was turned off, and upon the end of fiber formation, rotor and airflows were stopped. Then, the fiber primary layer was photographed, removed from the accumulation grid and weighed, with mass being an additional parameter (range between 7 g and 33 g). A list of operating points is provided in Table 1, along with the layer bulk and area density computed by Eqs. (4) and (5), respectively.

Note that the volume flow rates in Table 1 are given for the mean atmospheric conditions during our measurements: 23 °C temperature, 98.6 kPa absolute pressure and 29 % relative humidity.

In each of the operating points listed in Table 1, primary layer was visualized as follows. After stopping the spinner operation, the suction fan was removed and the primary layer was illuminated from above by diffuse light. A camera (Casio EX-F1) was

Table 1. *Operating points for primary layer visualization*

Op. point No.	f_c [Hz]	Δp [kPa]	f_s [Hz]	m [g]	Q_p [m³/h]	Q_p [m³/h]	ρ [kg/m³]	σ_{un} [%]
1a	50	50	7.0	10.5	27.0	2700	2.36	192
1b	50	50	7.0	14.5	27.0	2700	2.21	192
2a	50	50	9.1	9.5	27.0	3600	2.05	187
2b	50	50	9.1	10.5	27.0	3600	2.32	200
2c	50	50	9.1	12.5	27.0	3600	2.59	213
3a	50	50	11.4	9.5	27.0	4500	2.53	253
3b	50	50	11.4	13.0	27.0	4500	2.57	197
3c	50	50	11.4	30.0	27.0	4500	3.25	123
4	50	20	7.0	10.5	17.8	2700	2.32	171
5	50	20	9.1	11.0	17.8	3600	1.97	203
6	50	20	11.4	11.0	17.8	4500	1.89	189
7	50	0	7.0	11.0	0	2700	2.10	200
8	50	0	9.1	11.2	0	3600	2.48	126
9	50	0	11.4	13.5	0	4500	1.86	147
10	40	50	7.0	12.5	27.0	2700	1.99	177
11	40	50	9.1	13.5	27.0	3600	2.00	171
12	40	50	11.4	11.5	27.0	4500	2.06	196
13	40	20	7.0	9.0	17.8	2700	1.86	241
14	40	20	9.1	10.0	17.8	3600	2.38	312
15a	40	20	11.4	18.0	17.8	4500	2.55	182
15b	40	20	11.4	12.5	17.8	4500	2.29	266
16	40	0	7.0	13.0	0	2700	2.98	167
17	40	0	9.1	11.5	0	3600	2.72	188
18	40	0	11.4	6.0	0	4500	2.18	212
19	40	50	0	11.5	27.0	0	2.63	166
20	40	50	18.4	33	27.0	7200	6.91	117

placed underneath the accumulation grid and an image of the layer was taken (Fig. 5) using manual aperture and shutter time settings (f/7.5 and 0.08 s, respectively). For reference, the background (grid without fibers) was also photographed using the same visualization setup. Images were then processed by the method presented in section 1 so that the bulk and area density (Fig. 5b) was calculated. Also, the maximum thickness of the primary layer was manually measured (Fig. 5c) and used in Eq. (1) to obtain the attenuation coefficient α. The value $\alpha \approx 0.17$ m^{-1} was obtained for all operating points (OP) except OP 20, where $\alpha = 0.35$ m^{-1} was determined. This was most likely due to the more compact primary layer in OP 20 caused by a much higher suction flow rate.

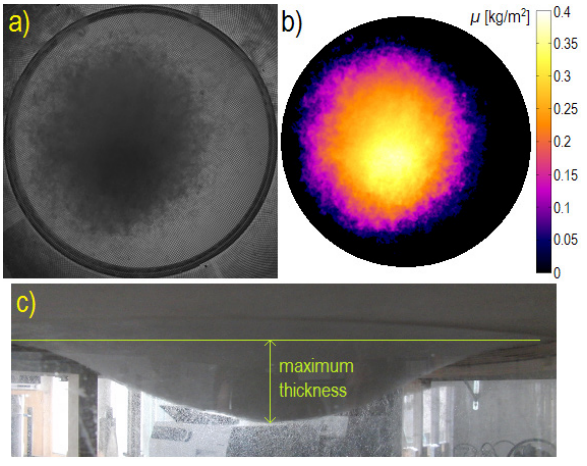

Fig. 5. *Sample visualization images (OP 3c); a) raw image; b) area density field; c) primary layer side view*

3 RESULTS AND DISCUSSION

3.1 Qualitative and Quantitative Properties of the Primary Layer

Spinning machine operating parameters were varied in a wide range (Table 1) and produced distinct forms of the sucrose primary layer (Fig. 6).

Primary layer mass distribution in Fig. 6 shows a significant effect of all operating parameters varied in the experiments. An increase of the spinner rotational speed (OP 13 and 4 represent f_c = 40 Hz and f_c = 50 Hz, respectively) increases the primary layer area due to the larger centrifugal forces which widen the fibrous flow. At the same time, the layer becomes more uniform (note a reduction in $\sigma_{\mu n}$; Table 1).

An even greater effect on the primary layer structure can be seen with regard to the airflow characteristics. In Fig. 6, the effect of the blow-

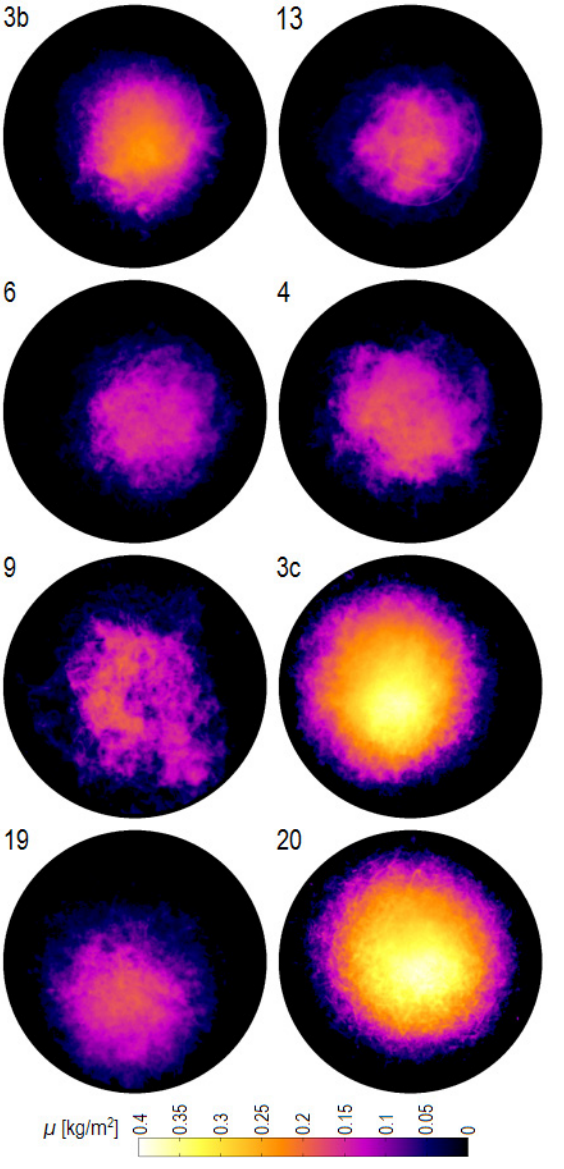

Fig. 6. *Fields of primary layer area density for different operating points; given are the OP numbers*

away pressure (and consequently, flow rate) is seen by comparison of plots for OP 9, 6 and 3b, where Δp was 0 kPa, 20 kPa and 50 kPa, respectively. When the fibers are transported only by the suction flow (OP 9, Δp = 0, Q_p = 0), the primary layer is asymmetrically shaped and scattered across the large portion of the accumulation grid. In this operating mode, large chunks of fiber wool were observed on the grid, leading to an unwanted inhomogeneity in the layer structure. As the blow-away pressure was raised towards 50 kPa (OP 4 and 3b), the primary layer shape became more axissymmetric and with fewer

visible inhomogneities. However, the layer became pile-shaped with a large thickness in the center, and its mean bulk density slightly increased. Such pile formation is unfavorable as the layer thickness should be as uniform as possible, but could largely be avoided by using a moving mesh.

Apart from the primary flow, the secondary (suction) flow also has a large effect on the quality of the primary layer. When the suction flow is not present and pneumatic transport depends entirely on the blow-away flow (OP 19, f_s = 18.4 Hz), the fibers may still reach the accumulation grid, but the flow is unstable and the primary layer can form far from the grid center. An increase in the suction flow rate, as clearly shown by data for the operating points 4 and 6 (f_s = 7.0 Hz and f_s = 11.4 Hz, respectively), causes the primary layer to shrink in area while its bulk density increases. If the suction flow rate is further increased (OP 20, f_s = 18.4 Hz), the layer bulk density rapidly increases while the area density distribution becomes practically axissymmetric. This is partly due to the fact that at larger Q_s, the pressure drop over the primary layer rises, resulting in a more intense layer compression.

Another contributing factor to the large bulk density in OP 20 was a relatively large primary layer mass (m = 33.0 g), which, due to the larger quantity of fibers, reduced the permeability of the accumulation grid and thus further increased the pressure drop over the layer. In OP 3c where the mass of the primary layer is similar (m = 30.0 g), the spatial distribution and maximum of μ is comparable to OP 20, but the bulk density is about 50 % lower, meaning that the layer is much less compact. For comparison, the layer bulk density in operating points 3a, 3b and 3c only varies by 28 % despite the mass range of approximately 1:3 (ρ rises monotonously with m, though). This suggests that the bulk density more sensitive to the suction flow rate than the primary layer mass, but both parameters are significant.

Due to the specific experimental setup (i.e. stationary accumulation grid) it is important to note that the primary layer formation is a transient process. The layer mass (or equally, fiber deposition time) is analogous to the combination of the fiberization mass flow and the accumulation grid velocity in a typical mineral wool manufacturing process.

3.2 Multiple Regression Models

Based on the results presented in the previous subsection, we suspect a strong correlation between the characteristic properties of the primary layer (ρ and $\sigma_{\mu n}$, Table 1) and the process input parameters (f_c, Q_p, Q_s, m). This hypothesis will be confirmed by the following power law multiple regression models:

$$\rho = a_0 \cdot f_c^{a_1} \cdot Q_p^{a_2} \cdot Q_s^{a_3} \cdot m^{a_4}, \quad (8)$$

$$\sigma_{\mu n} = a_0 \cdot f_c^{b_1} \cdot Q_p^{b_2} \cdot Q_s^{b_3} \cdot m^{b_4}. \quad (9)$$

The exponents a_0 to a_4 and b_0 to b_4 were determined by fitting of the power law models in Eqs. (8) and (9) to data in Table 1 (data was inserted in units given in the Nomenclatures section). Operating points with Q_p=0 or Q_s=0 were excluded from the model to avoid singularities. These points were only intended to demonstrate the most extreme operating conditions unsuitable for an industrial manufacturing process.

For Eq. (8) we obtain a_0=112, a_1=–0.141, a_2=0.225, a_3=0.389, a_4=0.498 and a relatively high coefficient of determination (R^2 = 0.88). This indicates a good correlation between modeled and input parameters.

For Eq. (9), the following values were calculated: b_0=14.2, b_1=–0.842, b_2=0.262, b_3=0.116, b_4=–0.589 and a R^2=0.78. The R^2 value is sufficiently high to conclude that the $\sigma_{\mu n}$ statistical parameter is representative of the process quality and can be modeled from selected input parameters.

Regression models can now be rewritten in a final form:

$$\rho = 112 \cdot f_c^{-0.141} \cdot Q_p^{0.225} \cdot Q_s^{0.389} \cdot m^{0.498}, \quad (10)$$

$$\sigma_{\mu n} = 14.2 \cdot f_c^{-0.842} \cdot Q_p^{0.262} \cdot Q_s^{0.116} \cdot m^{-0.589}. \quad (11)$$

The goodness of fit of these regression models can also be shown graphically, Figs. 7 and 8. It is evident that most of the measurements are in a good agreement with the model.

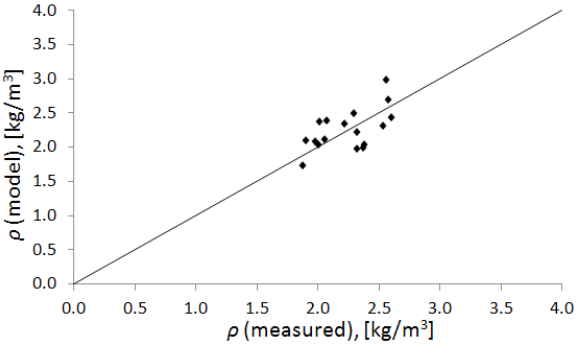

Fig. 7. *Correlation between measured and modeled values of ρ*

The model in Eq. (10) indicates that the bulk density of the primary layer increases with the flow

rate of the blow-away and suction air as well as with the layer mass. As said, this can be explained by layer compression due to increased pressure drop over the accumulation grid. On the other hand, ρ falls with rotational speed of the spinner rotor as fiber centrifugal forces are increased, scattering fibers to a larger area. Consequently, the layer thickness is reduced, leading to a reduction of the pressure drop across the accumulation grid.

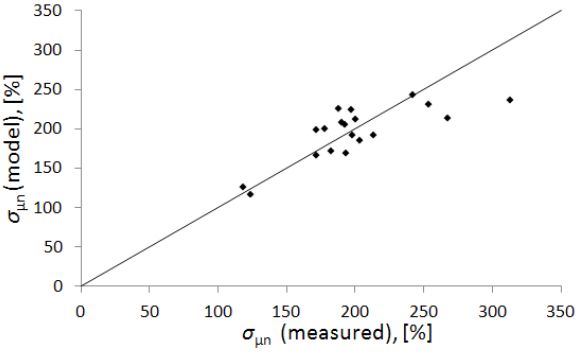

Fig. 8. *Correlation between measured and modeled values of* $\sigma_{\mu n}$

In comparison with Eq. (10), the exponent values in the model for $\sigma_{\mu n}$ (Eq. (11)) are very different. $\sigma_{\mu n}$ decreases with the spinner rotational speed, which can again be explained by the scattering of the fibers over a larger area, resulting in a primary layer of a more uniform thickness. However, $\sigma_{\mu n}$ also decreases with the primary layer mass as the layer structure becomes more and more homogenous when it grows in thickness. On the other hand, $\sigma_{\mu n}$ seems to slightly rise with both blow-away and suction flow rate. This is most likely due to the fact that an increase in Q_p and Q_s results in a more axissymmetric primary layer formation. This may (under certain conditions) contribute to formation of piles on the accumulating grid, and $\sigma_{\mu n}$ increases due to variations in the primary layer height rather than structural inhomogeneities.

4 CONCLUSIONS

The process of the mineral wool primary layer formation was studied experimentally on a model spinning machine with sucrose as a working medium. The bulk and area density of the layer were determined by a light absorption method which provided a good measure for the layer structure and thickness. The bulk density, which should ideally be as low as possible, was found to depend on the spinner rotational speed, flow rates of the blow-away and suction air as well as well as the mass of accumulated fibers. The bulk density of the primary layer was shown to increase with its own permeability until a new equilibrium is reached. Another important measure for the primary layer is the homogeneity of its structure which was quantified by the normalized standard deviation of the layer area density, $\sigma_{\mu n}$. A low value of $\sigma_{\mu n}$ is desired as it implies a good uniformity of the primary layer thickness and structure.

An important step in optimization of investigated process is to determine an envelope of the operating parameters which yields a good quality primary layer. The spinner rotational speed was shown to control the layer width and height profile while the size and spatial distribution of inhomogeneities is mostly determined by the pressure and flow rate of the blow-away airflow. On the other hand, the primary layer bulk density is most significantly affected by the suction flow rate and layer mass. Further research should include the modeling of an actual mineral wool manufacturing process with a moving accumulating grid where primary layer formation is continuous. New experimental and numerical models will improve the understanding of the fiber transport and primary layer formation process and introduce new possibilities for automatization of the process control.

5 NOMENCLATURES

A	[m²]	accumulation grid surface
f_c	[Hz]	spinner rotor rotational speed
f_s	[Hz]	suction fan rotational speed
h	[m]	primary layer height
I	[Wm⁻²]	light intensity after absorption
I_0	[Wm⁻²]	incoming light intensity
m	[kg]	primary layer mass
Q_p	[m³s⁻¹]	blow-away flow rate
Q_s	[m³s⁻¹]	suction flow rate
V	[m³]	primary layer volume
x	[m]	distance from left image edge
y	[m]	distance from top image edge
α	[m⁻¹]	attenuation coefficient
α_m	[m²kg⁻¹]	mass attenuation coefficient
Δp	[Pa]	blow-away air overpressure
μ	[kgm⁻²]	prim. layer mean area density
$\bar{\mu}$	[kgm⁻²]	prim. layer local area density
ρ	[kgm⁻³]	primary layer bulk density
σ_μ	[kgm⁻²]	standard deviation of μ
$\sigma_{\mu n}$	[–]	normalized st. deviation of μ

6 REFERENCES

[1] Širok, B., Blagojević, B., Bullen, P. (2008). *Mineral Wool: Production and Properties. Woodhead Publishing,* Cambridge, **DOI:10.1533/9781845694456**.

[2] Czygany, T., Vad, J., Kornel, P. (2005). Basalt fiber as a reinforcement of polymer composites. *Periodica Polytechnica Mechanical Engineering*, vol. 49, no. 1, p. 3-14.

[3] Vad, J., Morlin, B. (2007). Fluid mechanical model for formation of mineral wool fibers applied in polymer composites. *Materials Science Forum*, vol. 537-538, p. 269-276, **DOI:10.4028/www.scientific.net/MSF.537-538.269**.

[4] Zhao, D., Zhang, Z., Liu, L., Wang, X. (2015). A novel kinematic model for molten slag fiberization: Prediction of slag fiber properties. *Metallurgical and Materials Transactions B*, vol. 46, no. 2, p. 993-1001, **DOI:10.1007/s11663-014-0259-9**.

[5] Panda, S., Marheineke, N., Wegener, R. (2008). Systematic derivation of an asymptotic model for the dynamics of curved viscous fibers. *Mathematical Methods in Applied Sciences*, vol. 31, no. 10, p. 1153-1173, **DOI:10.1002/mma.962**.

[6] Mukundan, D.V., Panda, S. (2013). Temperature effects on curved stationary viscous thermal fiber jets. *Australian Journal of Basic and Applied Sciences*, vol. 7, no. 7, p. 613-622.

[7] Marheineke, N., Wegener, R. (2009). Asymptotic model for the dynamics of curved viscous fibres with surface tension. *Journal of Fluid Mechanics*, vol. 622, p. 345-369, **DOI:10.1017/S0022112008005259**.

[8] Marheineke, N., Liljo, J., Mohring, J., Schnebele, J., Wegener, R. (2012). Multiphysics and multimethods problem of rotational glass fiber melt-spinning. *International Journal of Numerical Analysis and Modeling, Series B*, vol. 3, no. 3, p. 330-344.

[9] Qin, Y., Lv, X., Bai, C., Chen, P., Qiu, G. (2013). Dry granulation of molten slag using a rotating multi-nozzle cup atomizer and characterization of slag particles. *Steel Research International*, vol. 84, no. 9, p. 852-862, **DOI:10.1002/srin.201200325**.

[10] Qin, Y., Lv, X., Bai, C., Chen, P., Qiu, G., Jie, Z. (2014). Mechanism of dry molten slag granulation using a rotating multi-nozzle cup atomizer. *Steel Research International*, vol. 85, no. 1, p. 44-52, **DOI:10.1002/srin.201300007**.

[11] Kraševec, B., Širok, B., Bizjan, B., Hočevar, M. (2015). Fibre density distribution in a layer of glass wool. *Glass Technology - European Journal of Glass Science and Technology, Part A*, vol. 56, no. 5, p. 145-152, **DOI:10.13036/17533546.56.5.145**.

[12] Lin, J.Z., Liang, X.I., Zhang, S.L. (2012). Numerical simulation of fiber orientation distribution in round turbulent jet of fiber suspension. *Chemical Engineering Research and Design*, vol. 90, no. 6, p. 766-775, **DOI:10.1016/j.cherd.2011.09.016**.

[13] Capone, A., Romano, G.P., Soldati, A. (2015). Experimental investigation on interactions among fluid and rod-like particles in a turbulent pipe jet by means of particle image velocimetry. *Experiments in Fluids*, vol. 56, no. 1, **DOI:10.1007/s00348-014-1876-4**.

[14] Qi, G., Nathan, J.G., Lau, C.W.T. (2015). Velocity and orientation distributions of fibrous particles in the near-field of a turbulent jet. *Powder Technology*, vol. 276, p. 10-17, **DOI:10.1016/j.powtec.2015.02.003**.

[15] Blagojević, B., Širok, B., Hočevar, M. (2003). Monitoring and control of quality of the primary layer of mineral wool on a disc spinning machine. *Instrumentation Science & Technology*, vol. 31, no. 1, p. 67-80, **DOI:10.1081/CI-120018408**.

[16] Bajcar, T., Blagojević, B., Širok, B., Dular, M. (2007). Influence of flow properties on a structure of a mineral wool primary layer. *Experimental Thermal and Fluid Science*, vol. 32, no. 2, p. 440-449, **DOI:10.1016/j.expthermflusci.2007.05.007**.

[17] Badel, E., Letang, J.-M., Peix, G., Babot, D. (2003). Quantitative microtomography: measurement of density distribution in glass wool and local evolution during a one-dimensional compressive load. *Measurement Science and Technology*, vol. 14, no. 4, 410-420, **DOI:10.1088/0957-0233/14/4/302**.

[18] The Breeze Instruction Manual: Models 3030, 3030SR, 3030EX, 3040, 3040SR (2015). From *https://www.gmpopcorn.com/products/manuals/42147.pdf*, accessed on 2015-08-25.

Strojniški vestnik - Journal of Mechanical Engineering 62(2016)3, 187-196
© 2016 Journal of Mechanical Engineering. All rights reserved.
DOI:10.5545/sv-jme.2015.2964 Original Scientific Paper
Received for review: 2015-08-21
Received revised form: 2016-01-18
Accepted for publication: 2016-01-25

Nonlinear Response of Cantilever Beams Due to Large Geometric Deformations: Experimental Validation

Claudia Aide Gonzalez-Cruz* – Juan Carlos Jauregui-Correa – Gilberto Herrera-Ruíz
Autonomous University of Querétaro, Faculty of Engineering, Mexico

Many structural elements, such as gas turbine fans, wind turbine blades, springboards among others are designed as slender elements. Since their dynamic behaviour can be modeled as cantilever beams, it is important to understand their nonlinear behaviour due to large deformations. In this way, this work presents the experimental validation of a simplified model of a cantilever beam. The model is formulated considering large geometric deformations and assuming a Galerkin approach. The model is validated experimentally, and it is found that there is a characteristic frequency related to the nonlinear terms. The data is analysed using time-frequency maps produced with the continuous wavelet transform.

Keywords: phase diagram, harmonic distortion, continuous wavelet transform, large geometric deformations

Highlights

- *Large geometric deformations in cantilever beams produce nonlinear behaviour.*
- *The dynamic response of a cantilever beam is highly dominated by the structural damping.*
- *Cantilever beam is modeled with a nonlinear restoring force.*
- *Nonlinear frequencies only can be found numerically or experimentally.*

0 INTRODUCTION

This paper presents an experimental validation of the nonlinear behaviour of cantilever beams. It is postulated that the nonlinear behaviour of a cantilever beam is due to large deformations. In order to validate this assumption, it is necessary to derive the nonlinear equations and compare them numerically with experimental results. From the experimental data, it is found that the dynamic response is highly dominated by the structural damping. This parameter diminishes the amplitude and, as a consequence, the nonlinear effect.

The subject has been studied for many years, and several researchers have proposed dynamic models and experimental procedures. Nevertheless, unanswered questions remain, and the validation has not been fulfilled. The bending of beams has been analysed especially for elastic problems. Halilovič and Štok **[1]** presented a deflection analysis of rectangular closed section beams with no hardening; assuming elastoplastic behavior, they derived analytical solutions considering small strains and small displacements. Yu et al. **[2]** modelled a naturally curved and twisted rectangular beam; their analysis considered a closed thin-walled section. The model was based on the principle of minimum potential energy. Although their model can be extended to solid cross-section beams, it is based on the small displacement theory. Regarding a large deformation model, Gerstmayr and Irschik **[3]** represented the large deformation using the elastic line approach. They used a cubic polynomial to represent the displacement; a similar approach is also applied in the present work. They used the weak form of the equation of motion using Lagrange's equation and D'Alembert's principle. Their results showed the vertical displacement of a beam as a function of time, and they never presented frequency or phase diagram analysis. Ashour and Nayfeh **[4]** presented a research on the nonlinear behaviour of an absorber to control vibrations in plates. The absorber is based on the saturation phenomenon associated with a quadratic nonlinear term and internal resonances. They identified two main problems regarding the application of auto-parametric absorbers: coupling two mechanical systems together and maintaining two-to-one internal resonances. For solving this problem, they applied a piezoelectric ceramic actuator; in their solution, they applied their method to a cantilever beam. Their beam model is only linear; the nonlinearity is in the actuator function. They found the solution applying Nayfeh's perturbation method.

The conventional method for the experimental study of nonlinear mechanical systems is parameter sweeping, in which the parameter is ramped smoothly up and down while the system response is recorded. This method is frequently used to demonstrate the bifurcation condition. Using a path-following algorithm, Bureau et al. **[5]** developed a stabilizing control scheme for an experimental bifurcation analysis. In order to produce bifurcation, they proposed the application of a nonlinear

*Corr. Author's Address: Autonomous University of Querétaro, Faculty of Engineering, Cerro de las Campanas s/n, Ciudad Universitaria, Querétaro, Qro. 76010, Mexico, cgonzalez@uaq.mx

electromagnetic actuator and a proportional-derivative (PD) controller. With this method, it was possible to trace the bifurcation path. In their results, the phase diagram lacked representation of the two attracting poles of a typical bifurcation solution. Malatkar and Nayfeh [6] described a procedure for determining the nonlinear parameters of a cantilever beam excited at the supported end. The bifurcation plot was constructed using the sweep technique. They found that the large deformation component was neglected in their experiments. Therefore, it is confirmed that damping suppresses the large deformation effect. Paak et al. [7] analysed the nonlinear vibrations of a cantilevered cylinder. In their model, they considered the large displacement terms in the strain formula and they approximated the displacements as sinusoidal series. Their results are similar to the phase diagrams presented in the following sections. In a similar work, Stoykov and Ribeiro [8] presented a nonlinear forced vibration model for beams. They found similar phase diagrams with high amplitudes in the excitation force. Li and Zhang [9] used the B-spline function to derive a dynamic model of a tapered beam. They approximated the deformation variables as a cubic B-spline function. Several researchers described different approaches for determining the nonlinear term. Stangl et al. [10] modelled a cantilevered pipe as a Euler elastic; they considered large deflections without order-of-magnitude assumptions. Equations of motion were obtained using an extended version of the Lagrange equations in combination with a Ritz method. Wang and Liew [11] modelled elastodynamic problems using an improved complex variable moving least-square approximation and the Galerkin procedure. Furthermore, they enhanced the computing efficiency using an improved complex variable element-free method. Wang et al. [12] proposed a nonlinear model for a Euler-Bernoulli microscale beam. The governing equations are developed from the Hamilton principle following the modified couple stress theory and the Von Kármán geometrically nonlinear theory. The governing equations are reduced the partial differential governing equations to a nonlinear two-point boundary value problem in a spatial variable by means of the Kantorovich time-averaging method. Zhang et al. [13] modelled a deploying-and-retreating wing as a cantilever laminated composite beam. They derived the governing equations of motions from the Hamilton's principle and Reddy's third-order theory and von Karman type equations of large deformation. By means of the Galerkin method, the dimensionless partial differential equation is transformed into a set of the ordinary differential equations. Noor et al. [14] developed simple mixed finite element models for curved thin-walled beams, the models include the effects of flexural-torsional coupling, the additional effects of transverse shear deformation, and rotary inertia. In general, it is assumed that large deflections are related to a nonlinear stiffness, whereas the damping term is always linear. Machado and Cortínez [15] developed a nonlinear model for beams. Their formulation only considered the elastic deformation, and they neglected the dynamic effects. Ramezani [16] derived a beam model based on the strain gradient elasticity theory. He assumed large deformations but proposed a dynamic equation with a stiffness function with a cubic coefficient. Kang and Li [17] presented a model of a cantilever beam with nonlinearities. They approximated the large deformations as a function of the stress-strain exponent. Fotouhi [18] presented a dynamic analysis of flexible beams. He considered only the free vibration case. He solved the problem using ANSYS. The results are presented in a way that is difficult to compare them with further analysis. He showed that large deformation analysis can be conducted with commercial software. Shad et al. [19] used a similar approach to the analysis of rotor dynamics using higher order deformations in bending. Although their model considers a simple supported beam, their analysis is similar to the analysis of cantilever beams. They showed bifurcations in the frequency spectrum.

The purpose of this paper is to demonstrate that the nonlinear behaviour of a cantilever beam is due to the large deformation term. Although the structural damping of the beam is a dominant parameter that diminishes large deformations, it is possible to reveal the nonlinear behaviour with the sweep method. Thus, in order to deploy the nonlinear terms, it is necessary to produce large deformations. Do so, in practice, is difficult to achieve.

The remainder of this paper is organized as follows. Section 1 presents the derivation of a simplified model using the beam deflection. Section 2 provides the analysis techniques used for data processing. Section 3 presents the numerical solution of the model for free vibration and forced vibration tests. Section 4 presents the experimental validation of the model. Finally, Section 5 gives the conclusions.

1 DYNAMIC MODEL

According to Gonzalez and Jauregui [20], nonlinear dynamic behaviour can be modelled using the beam deflection model. Since the purpose of this work is to demonstrate the effect of large deformations, the

following development is based on the simplest beam model. As described by them, it is assumed that the material is homogeneous, orthotropic, and linear. The strain is found from the deformation of the beam, assuming that the perpendicular displacement is greater than the beam thickness, as shown in Fig. 1.

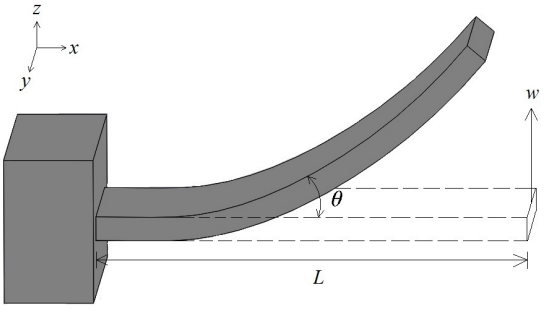

Fig. 1. *Geometry of the cantilever beam*

If the beam is represented as a one-dimensional element, and the strain only occurs along the x direction; then, the strain field as a function of the bending curvature can be expressed as:

$$\varepsilon = \frac{z\left(\frac{\partial^2 w}{\partial x^2}\right)}{\sqrt{\left(1+\left(\frac{\partial w}{\partial x}\right)^2\right)^3}}, \tag{1}$$

where z is the local coordinate perpendicular to the beam dimension, x is the coordinate along the beam dimension and w is the displacement along z. The sub-index indicates partial derivatives with respect to x. Expanding the rational term as a convergent series:

$$\frac{1}{\sqrt[2]{(1+m)^3}} = 1-\frac{3}{2}m+\frac{15}{8}m^2-\frac{105}{48}m^3+\ldots. \tag{2}$$

Then, the strain function can be rearranged as:

$$\varepsilon = z\left(\frac{\partial^2 w}{\partial x^2}\right)\left(1-\frac{3}{2}\left(\frac{\partial w}{\partial x}\right)^2\right). \tag{3}$$

Using the Galerkin method, the displacement field can be approximated by a polynomial of the form:

$$w = \sum_{i=1}^{N} a_i x^{i-1}, \tag{4}$$

where N is the number of degrees of freedom in the element and the coefficients a_i are determined from the generalized coordinates. If the beam is represented as a one-dimension element with two nodes, $j=1,2$, then, there are four generalized coordinates:

$$\mathbf{u} = \{w_1, \theta_1, w_2, \theta_2\}, \tag{5}$$

where $\mathbf{u}$ is the generalized coordinates vector, w_j is the displacement and θ_j are the bending angle of the corresponding nodes. Therefore, for this particular case, the polynomial in Eq. (4) has four coefficients.

The equation of motion is found using Lagrange's equation. The potential energy V is determined from the strain energy function. Since it is a unidimensional element, it can be simplified as:

$$V = \frac{1}{2}\int_v \sigma\varepsilon\, dv. \tag{6}$$

Considering only elements with linear material properties, the constitutive equation can be expressed as:

$$\sigma = E\varepsilon. \tag{7}$$

Substituting Eq. (7) into Eq. (6), the potential energy is given as follow:

$$V = \frac{1}{2}\int_v E\varepsilon^2 dv. \tag{8}$$

In contrast, the kinetic energy is determined as:

$$T = \frac{1}{2}\int_v \rho\left(\frac{d\mathbf{u}}{dt}\right)^T\left(\frac{d\mathbf{u}}{dt}\right)dv. \tag{9}$$

Considering that the beam is homogeneous, and the cross section is constant, Eqs. (8) and (9) are included into Lagrange's equation. Then, four equations are derived, one for each generalized coordinate:

$$m_i\frac{d^2u_i}{dt^2}+\sum_{k=1}^{4}\frac{\partial V}{\partial a_k}\frac{\partial a_k}{\partial u_i}=0, \tag{10}$$

where m_i is the associated mass to each node. Considering that the beam element is fixed at one end $w_1=0$, $\theta_1=0$ and redefining the other two generalized coordinates as $w_2=0$, $\theta_2=0$, Eq. (10) is reduced to two nonlinear equations:

$$\begin{aligned} &m\frac{d^2w}{dt^2}+\xi\frac{dw}{dt}+\frac{17496}{385}\frac{EIw^5}{L^7}-\frac{486}{11}\frac{EI\theta w^4}{L^6}+\\ &+\left(\frac{1620}{11}\theta^2-\frac{1296}{5}\right)\frac{EIw^3}{7L^5}-\left(\frac{729}{22}\theta^3-162\right)\frac{EIw^2}{7L^4}+\\ &+\left(\frac{54}{77}\theta^4-\frac{216}{35}\theta^2+12\right)\frac{EIw}{L^3}-\\ &-\left(\frac{522}{385}\theta^4-\frac{24}{7}\theta^2+6\right)\frac{EI\theta}{L^2}=F(t), \end{aligned} \tag{11}$$

$$J\frac{d^2\theta}{dt^2}+\xi\frac{d\theta}{dt}-\frac{486}{55}\frac{EIw^5}{L^6}-\frac{810}{77}\frac{EI\theta w^4}{L^5}+$$
$$+\left(-\frac{729}{22}\theta^2+54\right)\frac{EIw^3}{7L^4}+\left(\frac{108}{11}\theta^2-\frac{216}{5}\right)\frac{EIw^2}{7L^3}+$$
$$+\left(-\frac{522}{77}\theta^4+\frac{72}{7}\theta^2-6\right)\frac{EIw}{L^2}+$$
$$+\left(\frac{1944}{385}\theta^4-\frac{256}{35}\theta^2+4\right)\frac{EI\theta}{L}=0, \quad (12)$$

where $F(t)$ is the excitation force and the polynomial terms included in the stiffness are related to the restoring force generated by the potential energy. Therefore, the restoring force is modelled as a fifth-degree polynomial. In order to demonstrate the effectiveness of the model, experimental tests are also carried out. Then, both numerical and experimental data are analysed using different techniques.

2 ANALYSIS TECHNIQUES

Three different techniques are used to analyse numerical and experimental data: the frequency spectrum, the time-frequency map, and the phase diagram or phase plane [21].

The frequency spectrum is one of the most commonly used techniques for vibration analysis and machine-health monitoring. It is generated via the fast Fourier transform, and it provided the frequency content of the time-domain signal, showing up the harmonics frequency content. However, by itself, the frequency spectrum does not enable the analysis of the system evolution over time. The time-frequency map (spectrogram) is constructed using the continuous wavelet transform (CWT). The definition of the CWT is out of the scope of this work; readers are referred to [22]. The advantage of the CWT is that it can decompose a signal into a set of vectors within a set of frequencies. This set of frequencies displays the behaviour of each frequency as a function of time. If the system is linear, each frequency remains constant at any time; otherwise, it varies and, in the time-frequency map, it shows changes in the amplitude. The phase diagram, or phase plane, represents the instantaneous energy space. The vertical axis corresponds to the kinetic energy and the horizontal axis to the potential energy. If the dynamic response is stable, the trajectory described by the energy space will be a smooth function. Otherwise, the trajectory will display jumps or changes in direction, as well as many internal loops. Combining both analyses, phase diagram and time-frequency map, it is possible to determine the nonlinear behaviour of the cantilever beam.

3 NUMERICAL SIMULATION

Eqs. (11) and (12) were solved numerically. The solution was found using the Runge-Kutta method, assuming a sinusoidal excitation. Table 1 lists the beam parameters used in the model.

Table 1. *Dimensions and properties of the modelling beam*

Property	Value
Width, W	0.025 [m]
Thickness, T	0.003 [m]
Length, L	1. 000 [m]
Young's module, E	210 [GPa]
Natural frequency, ω_n	1.460 [Hz]
Mass, m	2.750 [kg]
Damping coefficient, ξ	0.269 [kg/s]

The numerical solution of the model was done considering different conditions: free vibration and forced vibration. The results and discussion of the numerical analysis are presented in the following subsections.

3.1 Results of the Free Vibration Response

First, the model was solved considering a small displacement in the free end of the beam as an initial condition. The results are shown in Fig. 2. The frequency spectrum shows two peaks at 1.49 Hz and 5.49 Hz, which correspond to the first and second vibration modes, respectively. The linear behaviour of the beam can be seen more clearly in the time-frequency map, since the amplitude of each frequency remains constant at any time. Moreover, there are not vertical stripes connecting the frequencies content in the map. The phase diagram (Fig. 2) shows closed loops forming an annular shape; it verifies the stable response of the beam when a small displacement value is given.

In a second case, the model was solved given a large displacement on the free end of the beam as an initial condition. The results are shown in Fig. 3. The frequency spectrum displays two main peaks at 1.3 Hz and 5.4 Hz. The first mode is shifted due to the nonlinear behavior, and both modes show sidebands at 2.4 Hz and 6.7 Hz, respectively. The nonlinear behaviour is evident in the time-frequency map as the amplitudes vary over time. The phase diagram shows closed loops with two attracting poles, and they

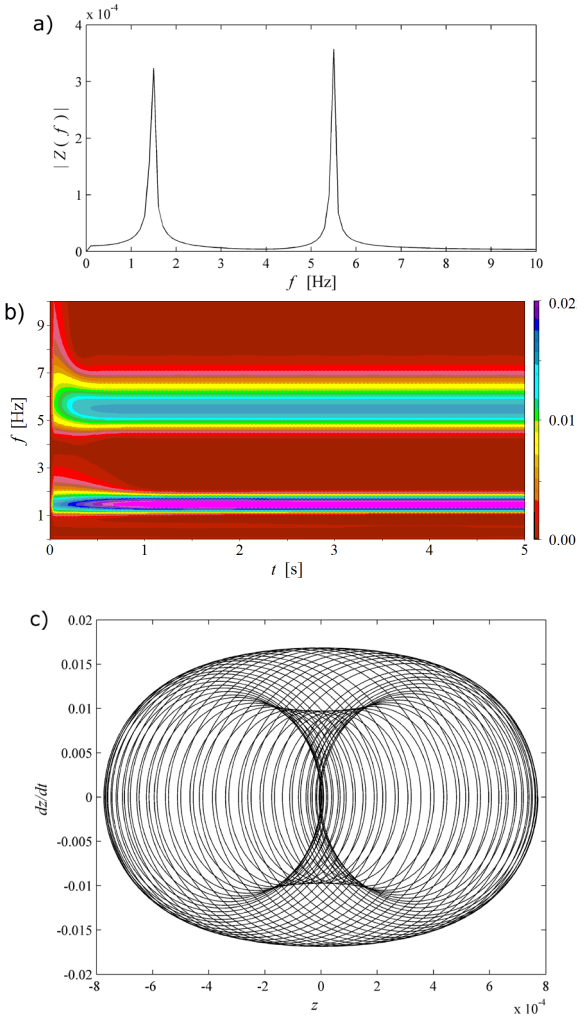

Fig. 2. *Numerical response, free vibration response for small deformations; a) frequency spectrum; b) time-frequency map; c) phase diagram**

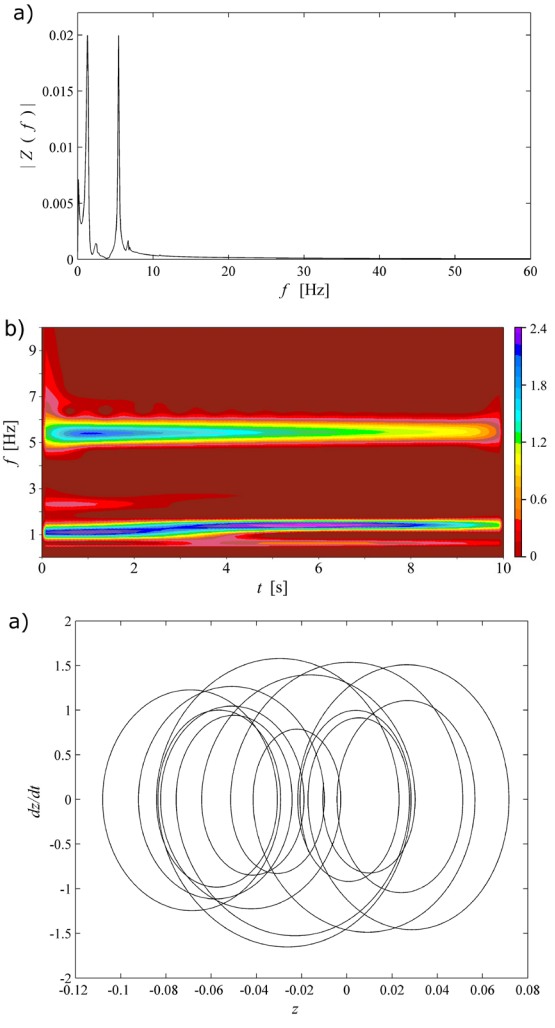

Fig. 3. *Numerical response, free vibration response at large deformations; a) frequency spectrum; b) time-frequency map; c) phase diagram**

remain at the same location at any time. Comparing this diagram with the linear solution, the nonlinear effect is noted.

3.2 Results of the Forced Vibration Response

A forced vibration solution was made at the nonlinear frequencies found in the experimental test for free vibration analysis. Fig. 4 shows the results when the system is excited at 2.9 Hz. The frequency spectrum shows a dominant peak at 2 Hz and a second and third ones at 5.9 Hz and 4.2 Hz, respectively. In the time-frequency map, it can be seen that the frequencies have a nonlinear behaviour since they vary in time. The phase diagram shows two attracting poles in the loops, also indicating the nonlinear behaviour.

Fig. 5 shows the results for the forced vibration at 18.1 Hz. The frequency spectrum shows two main peaks: the dominant peak at the excitation frequency and the second one at 1.8 Hz. The time-frequency map shows nonlinear behaviour at the excitation frequency. The phase diagram shows closed loops and unstable behaviour of the system.

Fig. 6 presents the results for the forced vibration at 51 Hz. The frequency spectrum shows the dominant peak at the excitation frequency and the second peak at 1.4 Hz. The time-frequency map displays the nonlinear behaviour near the 1.4 Hz frequency, since

*For interpretation of the references to color in figures 2 to 6 and 10 to 14, the reader is referred to the web version of the article.

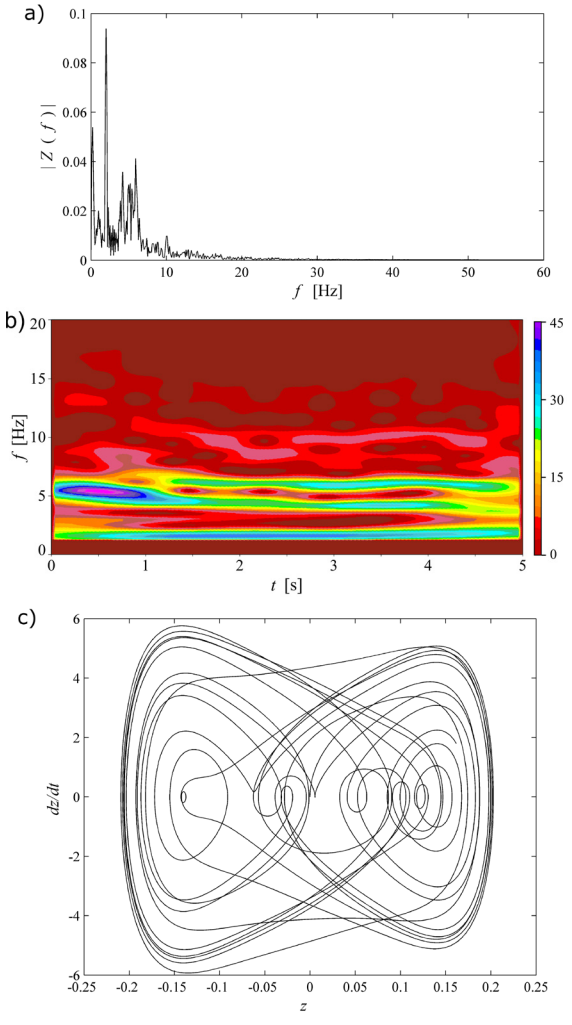

Fig. 4. *Numerical response at 2.9 Hz excitation frequency; a) frequency spectrum; b) time-frequency map; c) phase diagram**

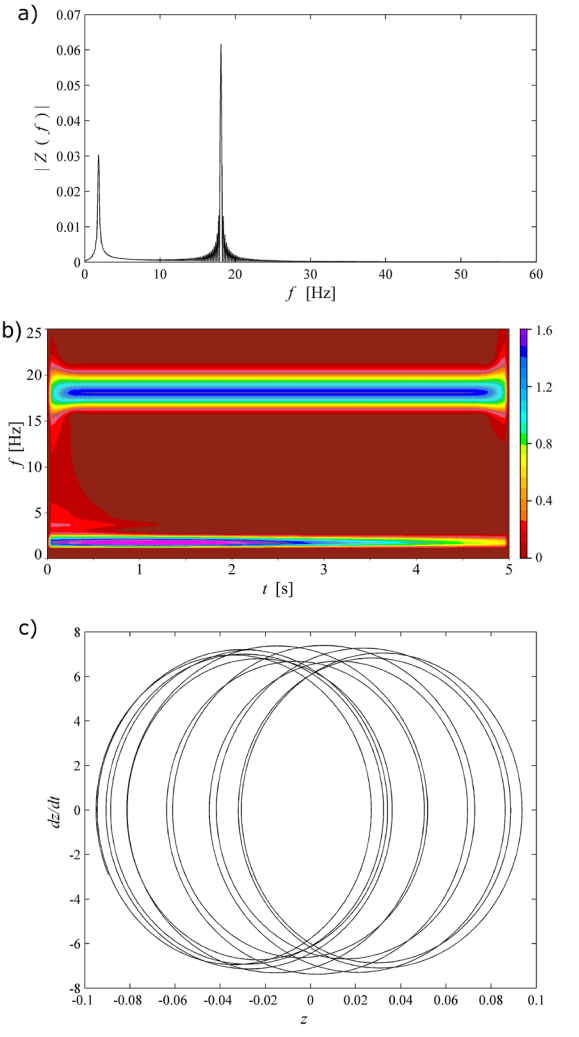

Fig. 5. *Numerical response at 18.1 Hz excitation frequency; a) frequency spectrum; b) time-frequency map; c) phase diagram**

it diminishes in time. The phase diagram shows closed loops, which are shifted along the *x*-axis.

In order to validate the simplified model, a set of tests was conducted.

4 EXPERIMENTAL VALIDATION

Two kinds of tests were done on a slender cantilever beam: free vibration and forced vibration. The experimental test rig is shown in Fig. 7. Essentially, it consists of a cantilever beam (1), whose parameters are listed in Table 1; an ADX-321J accelerometer (2) placed at the free end of the beam to measure the vibration on the axis *z* (see Fig. 1) (because the accelerometer mass is relatively small compared to the beam mass, it has not influence on the dynamic response of the beam); a data acquisition system NI USB-6366 (3); and a PC (4). The data acquisition was executed from a graphical interface developed in LabView®. During the forced vibration test, the cantilever beam was excited by the TIRA® TV 51144-IN inertial shaker (5). For this purpose, a frequency sweep of a sine vibration profile was generated by the Tektronix AFG 3102 signal generator (6); and then, the signal was amplified by the TIRA® BAA 1000 power amplifier (7) and then it was sent to the shaker to generate a sine oscillation. A schematic diagram of the test rig is shown in Fig. 8.

In order to produce the phase diagram, the displacement and velocity data were calculated numerically from the acceleration measurements.

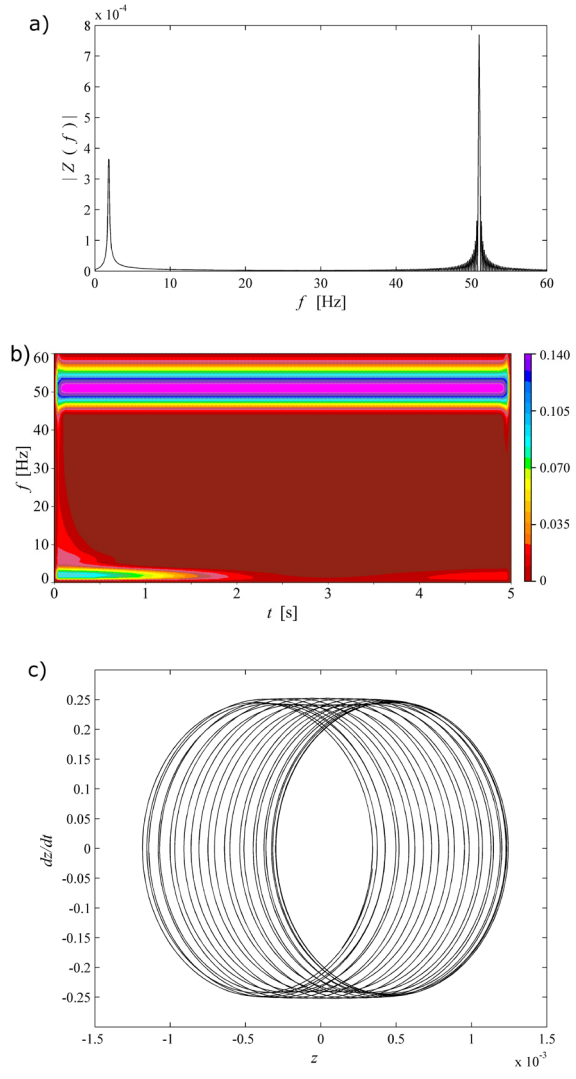

Fig. 6. *Numerical response at 51 Hz excitation frequency; a) frequency spectrum; b) time-frequency map; c) phase diagram**

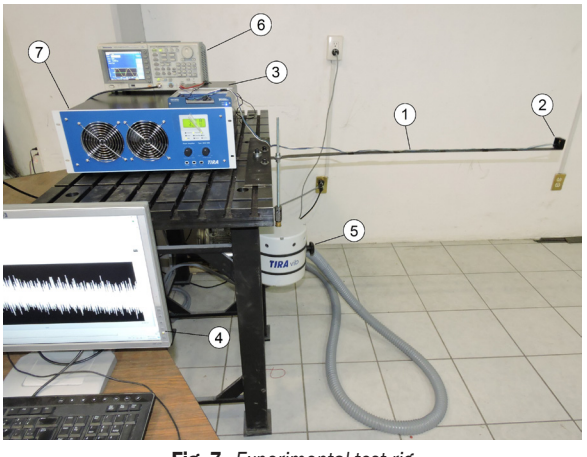

Fig. 7. *Experimental test rig*

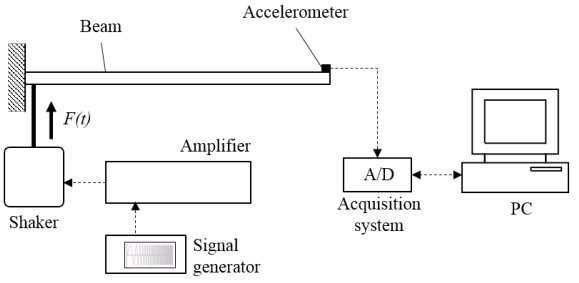

Fig. 8. *Schematic diagram of the experimental test rig*

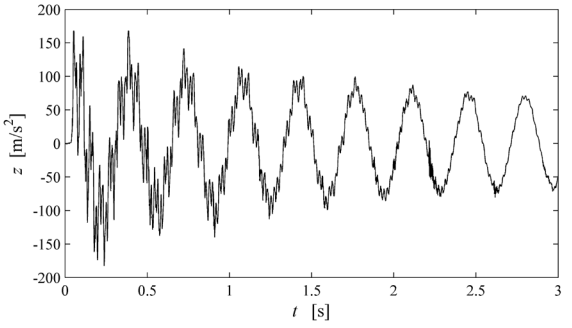

Fig. 9. *Time response of the system for the free vibration test*

4.1 Results of the Free Vibration Response

The time response for the free vibration test is shown in Fig. 9. In this figure, it is possible to see the nonlinear effect from the higher frequencies in the signal when the oscillations amplitude is higher; as the oscillations amplitude decreases, the system response is more linear.

The analysis of the free vibration response is presented in Fig. 10. The frequency spectrum shows a dominant peak at 2.9 Hz, a second one around 18.01 Hz, and a third one at 50.96 Hz. The time-frequency map shows the damping effect, but the nonlinear behaviour is clearly identified around the 18.01 Hz and 50.96 Hz frequencies, as the frequency amplitude varies over time. The phase diagram shows a shape with a squared form at the outsides, caused by the nonlinear behaviour. The attracting poles diminished because the numerical integration filters the high nonlinear frequencies. Although the overall shape keeps a polygonal shape, the time-frequency map reveals the nonlinear behaviour at the second and third frequencies.

4.2 Results of the Frequency Sweep Response

A frequency sweep ramped up and down was applied to the beam while the vibration response was recorded.

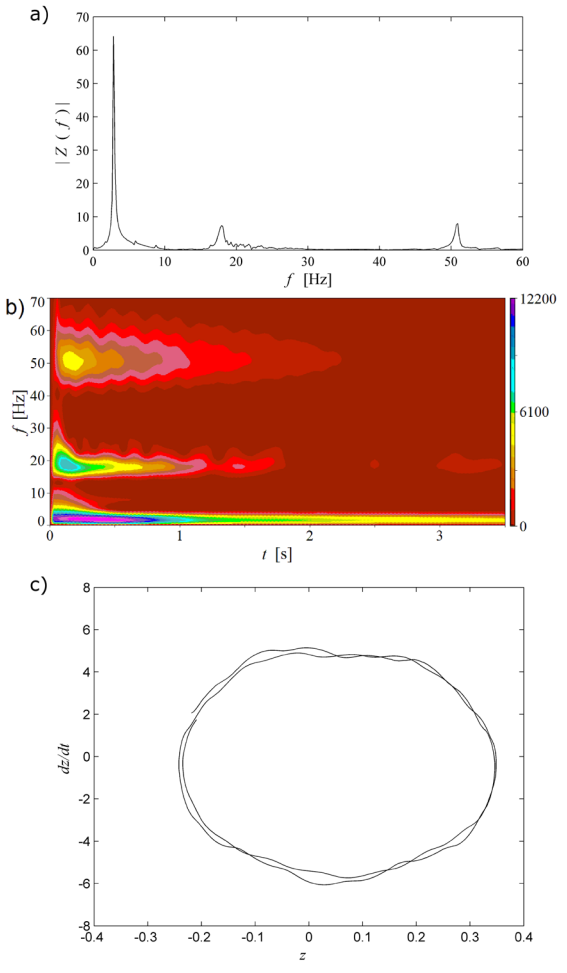

Fig. 10. *Experimental results, free vibration; a) time response; b) frequency spectrum; c) time-frequency map; d) phase diagram**

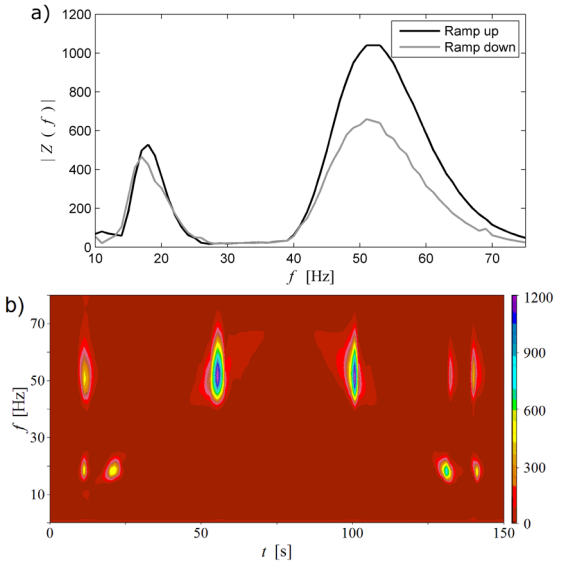

Fig. 11. *Experimental frequency response obtained by frequency sweep; a) response amplitude; b) time-frequency map**

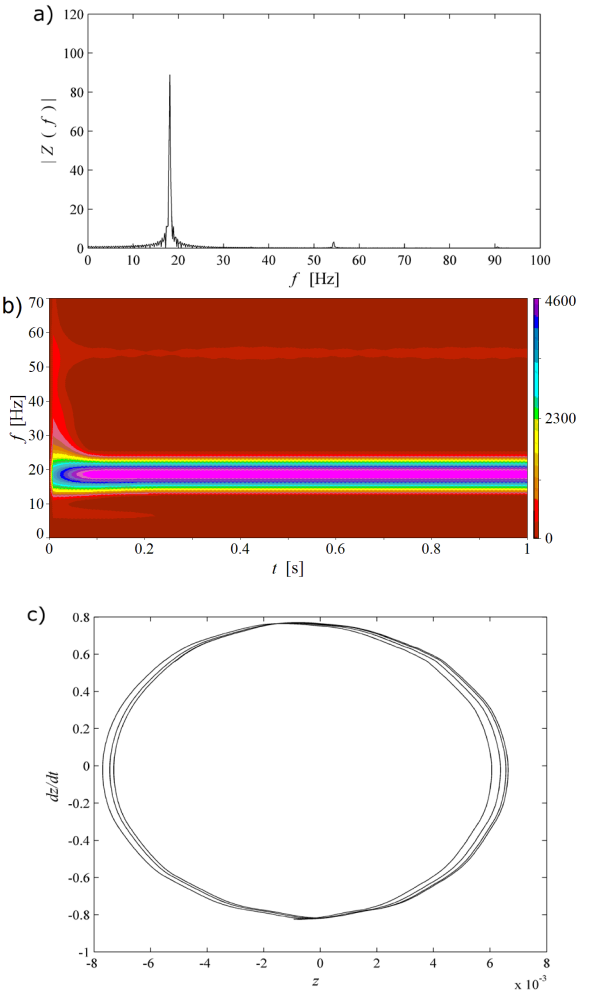

Fig. 12. *Experimental results, Forced vibration at 18.1 Hz; a) frequency spectrum; b) time-frequency map; c) phase diagram**

The response amplitude is presented in Fig. 11a. It is clear that there is a jump phenomenon associated with the nonlinearities of the beam at the 18.1 Hz and 51 Hz frequencies. In the case of the excitation frequency at 51 Hz, the beam shows relatively larger amplitudes. Therefore, the nonlinear behaviour is more noticeable at this frequency. The evolution in time of the system response is presented in Fig. 11b. It can be seen that the 51 Hz frequency is also excited when low frequencies are applied to the system.

Two forced vibration tests were conducted at the critical frequencies found in the jump diagram. The first measurement was recorded at an excitation frequency of 18.1 Hz. The analysis results are presented in Fig. 12. The frequency spectrum shows a dominant peak at the excitation frequency and a second small peak at 54 Hz. In the time-frequency

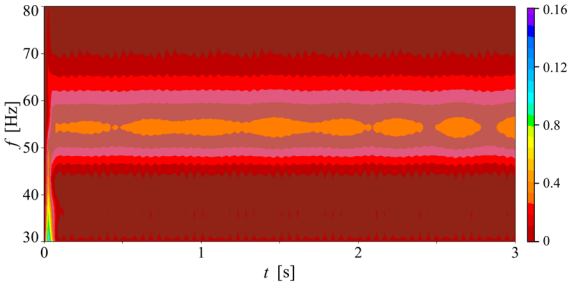

Fig. 13. *Nonlinear response of the 54 Hz frequency when the beam is excited at 18.1 Hz**

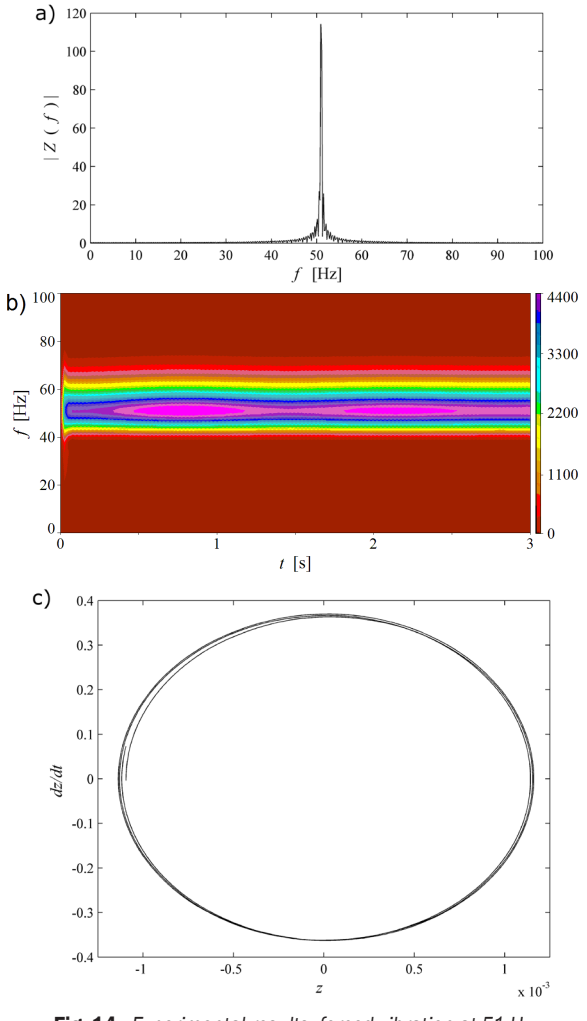

Fig. 14. *Experimental results, forced vibration at 51 Hz; a) frequency spectrum; b) time-frequency map; c) phase diagram**

map, it can be seen that the excitation frequency affects the system response. Measurements are dominated by the excitation frequency shadowing the beam response except at the other frequencies. Therefore, large amplitudes produced by the excitation frequency excites the nonlinear behaviour of the beam around 54 Hz. Fig. 13 shows a close view of the nonlinear behaviour around 54 Hz. The phase diagram shows closed loops with a balloon shape.

The second forced test was recorded at 51 Hz. The analysis results at this condition are shown in Fig. 14. The frequency spectrum shows only a dominant peak around the excitation frequency, whereas the time-frequency map exhibits the nonlinear behavior at the excitation frequency. The phase diagram exhibits shifting closed loops. It is important to notice that the beam has a characteristic behaviour due to the large deformation effect. This behaviour occurs at a particular frequency that cannot be determined with the linear theory.

Large deformations are a source of nonlinearity in cantilever beams. The effect produces a dynamic response that occurs at a different frequency. This frequency has no relation to those associated with the linear modes of vibration. Additionally, the nonlinear effect due to large deformations only occurs when the displacement is significantly large. In such cases, it is necessary to displace the tip of beam several times its thickness or excite the beam with a frequency near the nonlinear frequency. However, in engineering problems these conditions are not easily found.

5 CONCLUSIONS

Cantilever beams can have a nonlinear dynamic response due to large deformations. This behaviour has been identified experimentally, and it can be simulated assuming the dynamic model has polynomial terms. The numerical solution shows a typical harmonic distortion pattern due to polynomial terms in the model. When the excitation frequency is below the natural frequency, the phase diagram has two attracting poles. Experimental results show two particular frequencies around 18 Hz and 51 Hz, which are related to the nonlinear terms of the beam. Thus, these frequencies are associated with the large deformations effect. In the case of the excitation frequency at 51 Hz, the beam shows highly different amplitudes. From the frequency sweep test, it is found that the amplitudes were higher in the ramp-up process than in the ramp down procedure. Therefore, the nonlinear behaviour is more noticeable at this frequency. Nevertheless, these frequencies can only be found numerically or experimentally. The nonlinear behaviour due to large deformations occurs only at certain frequencies or when the beam is deflected a large amount. Otherwise, the large deformation effects

can be neglected. The simplified approximation presented in this work is sufficient for determining those frequencies that are due to the nonlinear terms. Any other method can produce these values only if the relative displacement between two points is significantly large.

6 ACKNOWLEDGEMENTS

The first author is grateful for the financial support from the Research Grants of the National Council for Science and Technology (CONACYT) in Mexico (No. Grant 238141).

7 REFERENCES

[1] Halilovič, M., Štok, B. (2007). Analytical tracing of the evolution of the elasto-plastic state during the bending of beams with a rectangular cross-section. *Strojniški vestnik - Journal of Mechanical Engineering*, vol. 53, no. 12, p. 806-818.

[2] Yu, A., Yang, R., Hao, Y. (2009). Theory and application of naturally curved and twisted beams with closed thin-walled cross sections. *Strojniški vestnik - Journal of Mechanical engineering*, vol. 55, no. 12, p. 733-741.

[3] Gerstmayr, J., Irschik, H. (2008). On the correct representation of bending and axial deformation in the absolute nodal coordinate formulation with an elastic line approach. *Journal of Sound and Vibration*, vol. 318, no. 3, p. 461-487, **DOI:10.1016/j.jsv.2008.04.019**.

[4] Ashour, O.N., Nayfeh, A.H. (2003). Experimental and numerical analysis of a nonlinear vibration absorber for the control of plate vibrations. *Journal of Vibration and Control*, vol. 9, no. 1-2, p. 209-234, **DOI:10.1177/107754603030748**.

[5] Bureau, E., Schilder, F., Santos, I.F., Thomsen, J.J., Starke, J. (2013). Experimental bifurcation analysis of an impact oscillator–tuning a non-invasive control scheme. *Journal of Sound and Vibration*, vol. 332, no. 22, p. 5883-5897, **DOI:10.1016/j.jsv.2013.05.033**.

[6] Malatkar, P., Nayfeh, A.H. (2003). A parametric identification technique for single-degree-of-freedom weakly nonlinear systems with cubic nonlinearities. *Journal of Vibration and Control*, vol. 9, no. 3-4, p. 317-336, **DOI:10.1177/107754603030754**.

[7] Paak, M., Païdoussis, M.P., Misra, A.K. (2013). Nonlinear dynamics and stability of cantilevered circular cylindrical shells conveying fluid. *Journal of Sound and Vibration*, vol. 332, no. 14, p. 3474-3498, **DOI:10.1016/j.jsv.2013.01.030**.

[8] Stoykov, S., Ribeiro, P. (2010). Nonlinear forced vibrations and static deformations of 3D beams with rectangular cross section: the influence of warping, shear deformation and longitudinal displacements. *International Journal of Mechanical Sciences*, vol. 52, no. 11, p. 1505-1521, **DOI:10.1016/j.ijmecsci.2010.06.011**.

[9] Li, L., Zhang, D. (2015). Dynamic analysis of rotating axially FG tapered beams based on a new rigid–flexible coupled dynamic model using the B-spline method. *Composite Structures*, vol. 124, p. 357-367, **DOI:10.1016/j.compstruct.2015.01.018**.

[10] Stangl, M., Gerstmayr, J., Irschik, H. (2008). An alternative approach for the analysis of nonlinear vibrations of pipes conveying fluid. *Journal of Sound and Vibration*, vol. 310, no. 3, p. 493-511, **DOI:10.1016/j.jsv.2007.06.020**.

[11] Wang, J.F., Liew, K.M. (2015). An accurate improved complex variable element-free method for numerical solutions of elastodynamic problems. *Engineering Analysis with Boundary Elements*, vol. 50, p. 304-312, **DOI:10.1016/j.enganabound.2014.09.005**.

[12] Wang, Y.-G., Lin, W.-H., Liu, N. (2013). Nonlinear free vibration of a microscale beam based on modified couple stress theory. *Physica E: Low-dimensional Systems and Nanostructures*, vol. 47, p. 80-85, **DOI:10.1016/j.physe.2012.10.020**.

[13] Zhang, W., Sun, L., Yang, X.D., Jia, P. (2013). Nonlinear dynamic behaviors of a deploying-and-retreating wing with varying velocity. *Journal of Sound and Vibration*, vol. 332, no. 25, p. 6785-6797, **DOI:10.1016/j.physe.2012.10.020**.

[14] Noor, A.K., Peters, J.M., Min, B.-J. (1989). Mixed finite element models for free vibrations of thin-walled beams. *Finite Elements in Analysis and Design*, vol. 5, no. 4, p. 291-305, **DOI:10.1016/0168-874X(89)90009-7**.

[15] Machado, S.P., Cortínez, V.H. (2004). Nonlinear geometric analysis of composite thin-walled beams. *Mecánica Computacional*, vol. 23, no. 5, p. 391-410.

[16] Ramezani, S. (2012). A micro scale geometrically non-linear Timoshenko beam model based on strain gradient elasticity theory. *International Journal of Non-Linear Mechanics*, vol. 47, no. 8, p. 863-873, **DOI:10.1016/j.ijnonlinmec.2012.05.003**.

[17] Kang, Y.-A., Li, X.-F. (2009). Bending of functionally graded cantilever beam with power-law non-linearity subjected to an end force. *International Journal of Non-Linear Mechanics*, vol. 44, no. 6, p. 696-703, **DOI:10.1016/j.ijnonlinmec.2009.02.016**.

[18] Fotouhi, R. (2007). Dynamic analysis of very flexible beams. *Journal of Sound and Vibration*, vol. 305, no. 3, p. 521-533, **DOI:10.1016/j.jsv.2007.01.032**.

[19] Shad, M.R., Michon, G., Berlioz, A. (2011). Modeling and analysis of nonlinear rotordynamics due to higher order deformations in bending. *Applied Mathematical Modelling*, vol. 35, no. 5, p. 2145-2159, **DOI:10.1016/j.apm.2010.11.043**.

[20] Jauregui-Correa, J.C., Gonzalez Brambila, O.M. (2009). *Mechanical Vibrations of Discontinuous Systems*. Nova Science Publishers, New York.

[21] Jauregui, J.C. (2014). *Parameter Identification and Monitoring of Mechanical Systems under Nonlinear Vibration*. Elsevier, Cambridge.

[22] Gao, R.X., Yan, R. (2011). *Wavelets, Theory and Applications for Manufacturing. Springer*, New York.

Strojniški vestnik - Journal of Mechanical Engineering 62(2016)3, 197-204
DOI:10.5545/sv-jme.2015.3109
Original Scientific Paper
Received for review: 2015-10-11
Received revised form: 2015-11-25
Accepted for publication: 2015-12-01
© 2016 Journal of Mechanical Engineering. All rights reserved.

Influence of Non-Productive Operations on Product Quality

Peter Eniko[1] – Mirko Soković[2] – Davorin Kramar[2]
[1] Difa d.o.o., Slovenia
[2] University of Ljubljana, Faculty of Mechanical Engineering, Slovenia

This paper addresses the study of piston bore machining. Within the framework of an experimental investigation single and combined effects and related reproducibility of such parameters on bore geometry and surface finish were investigated. Experiment planning and process modelling were performed by design of experiments (DOE) methodology. The experimental part was carried out in a regular production which is affected by non-productive operations that influence product quality. Based on the reaming process state of the art review and previous industrial experiences feed rate and spindle speed were identified as key productive operation factors in achieving bore cylindricity and surface roughness. Non-productive operations, such as clamping, washing and degreasing of the workpiece that negatively impacted results, were identified during experimental work with scanning electron microscope (SEM) analysis and pattern recognition in statistical process control (SPC) control chart. Negative impacts of non-productive operations were minimized with corrective actions. Regression analyses give models for both responses under consideration, namely bore cylindricity and surface roughness, and are at adequate confidence level. Experiments conducting, analysis and corrective actions are included in optimization strategy model which is schematically shown and interpreted in discussion.

Keywords: DOE, cylindricity, surface roughness, washing, degreasing

Highlights

- *For case study machining of piston bore in regular production which is affected by non-productive operations is analyzed.*
- *Surface cleanliness effect on measurement reproducibility is defined and minimized with corrective actions.*
- *Clamping device weakness is identified with pattern recognition in SPC control chart.*
- *Results show influence of non-productive operations on product quality and are schematically summarized in optimization strategy model.*

0 INTRODUCTION

Small batch production is mainly, due to the competitiveness of the market, oriented to achieve the required specifications with minimal manufacturing processes using standard cutting tools. Costume-made hydraulic valves are one of the unique cases of small batch production in combination with high tolerances requirements **[1]**. Honing represents the manufacturing process which enables achieving final geometric requirements for valve's cylinder bore and requires pre-processing on computer numerical control (CNC) machining centre with successive cutting processes drilling, milling and reaming. Specifications of the piston bore of the hydraulic valve housing prescribe cylindricity $/\circ/\leq 12$ µm and surface roughness $Ra \leq 1.6$ µm after reaming and cylindricity $/\circ/\leq 3$ µm and surface roughness $Ra \leq 0.4$ µm after honing.

This paper deals with reaming process quality improvement. Experiment planning and process modelling were performed by design of experiments (DOE) methodology **[2]**. Measuring method for bore cylindricity was defined as suggested in **[3]** and **[4]** and surface topology with mean roughness parameter *Ra* **[5]**. Within the framework of an experimental investigation single and combined effects, as well as related reproducibility, of such parameters on bore geometry and surface finish were investigated.

Factors that have been identified as key to achieve specifications (bolded factors in Fig. 1) have been studied within the experimental work. Authors in other reaming processes optimization studies investigated spindle speed *n* and feed rate *f* as numeric control factor **[6]** to **[9]**. In this study feed rate and spindle speed were recognized as the key productive operation factors as well.

Studies on CNC machining centres clamping devices field **[10]** and **[11]** present weaknesses and strengths of clamping devices to achieve the desired results of experimental work. Studies as Theodoris and Koutroumbas **[12]** and Hassan and Basksh **[13]** are focused on pattern recognition in Statistical Process Control (SPC) control charts.

The key non-productive operation factors that were analysed in this study were clamping device lack of rigidity and effect of surface cleanliness on measurements reproducibility. Clamping device weakness was minimized with focusing on only one (of three) clamping nest. Surface cleanliness impact was analysed with SEM analysis and was minimized with additional washing and degreasing.

*Corr. Author's Address: Difa d.o.o., Kidričeva cesta 91, 4220, Škofja Loka, Slovenia, peter.eniko@difa.si

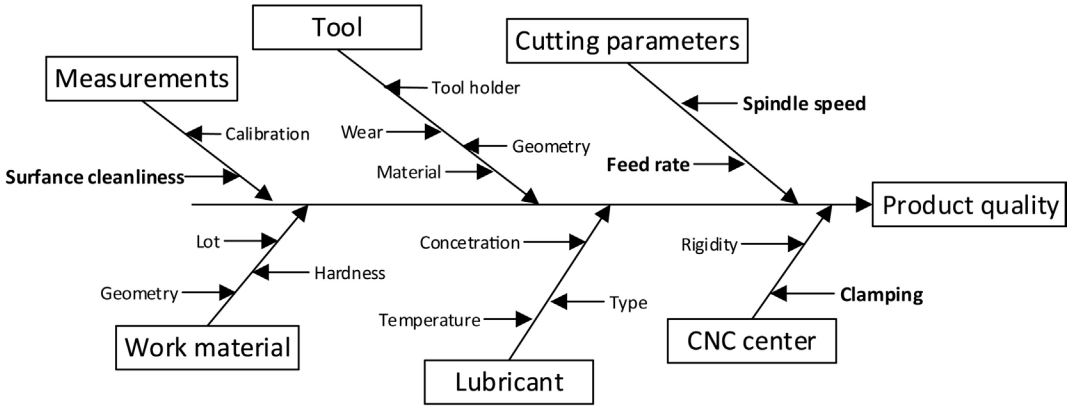

Fig. 1. *Key factors for achieving required product specification*

Impacts of the drill bit and the milling cutter tool life, the material of the cutting tool, the workpiece material, cutting tool holder, the geometry of the workpiece, and the characteristics of lubricant were neglected during research. They were neglected because the experiments were carried out on the same type of product, i.e. material and batch were the same and the same cutting tool was used. Drilling and milling parameters settings were not changed during experimental work.

Experiments conducting, analysis and corrective actions were included in optimization strategy model in discussion.

1 APPROACH AND METHOD

Experimental part includes a clear identification of the problem statement, selection of control factors and their respective levels and ranges. To improve production quality systematic approach with the use of DOE methodology has been selected. First with pre-experiments the region of operability for reaming i.e. reamer's technological window was determined using regular procedure [14]. After pre-experimental runs effect of clamping device weakness and inadequate surface cleanliness is presented. With exclusion of these noise factors, using DOE controlled factors significance on product quality was defined.

1.1 Technological Window Determining

Region of operability for reaming was determined with pre-experiments using regular procedure. Reamer with in-operation time (tool life) $t = 250$ min was utilised. Experiments were started from the existing production parameters settings (bold point in Fig. 2; spindle speed $n = 350$ rev/min, feed rate $f = 100$ mm/rev) and carried out in a diagonal direction of the n/f diagram. Extreme values of technological window (rectangle in Fig. 2) were determined with a point where machining conditions were still acceptable. The criterion for determining the technological window was set on values 30 % lower than prescribed with reaming process specifications. Cylindricity tolerance was set on $/\circ/ < 8\,\mu$m and surface roughness was set on $Ra < 1.1\,\mu$m. The goal of using such criteria was determination of more robust region of operability that would also be used for optimization experiments for further researches. Resulted technological window limits shown in Fig. 2 are listed in Table 1, as first (–1) and second (1) level of the reaming parameters.

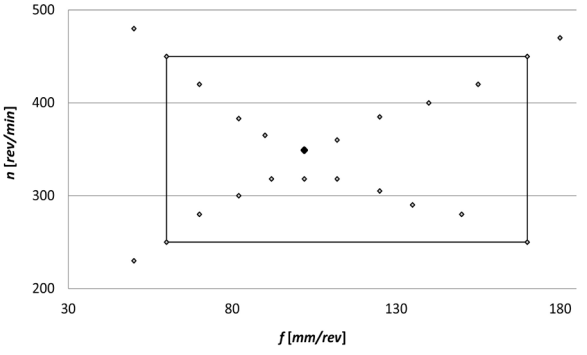

Fig. 2. *Determination of technological window for reaming process*

1.2 Experimental Set Up

The experimental part was carried out in regular production and thus includes real production noise factors, which are difficult to simulate in laboratory testing. Control factors and their levels were chosen on a base of pre-experiments and review of the

Table 1. *DOE and experimental results*

			Actual setting values		After CNC		After washing		After degreasing	
Exp. No.	Coded level		f [mm/rev]	n [rev/min]	Cylindricity [μm]	Ra [μm]	Cylindricity [μm]	Ra [μm]	Cylindricity [μm]	Ra [μm]
1	–1	–1	60	250	9.37	0.8	6.18	0.6	4.6	0.4
2	–1	–1	60	250	6.16	1.3	7.99	1.3	4.80	1.2
3	–1	–1	60	250	12.06	0.9	8.52	1.5	6.39	0.8
4	–1	1	60	450	6.04	0.9	8.26	0.6	5.3	0.6
5	–1	1	60	450	12.73	1.3	6.43	1.3	6.04	1.3
6	–1	1	60	450	14.53	1.9	8.83	1.7	8.53	1.4
7	1	–1	170	250	9.06	1.2	7.44	1.1	5.5	0.9
8	1	–1	170	250	6.75	0.8	8.02	1.1	5.30	0.7
9	1	–1	170	250	9.81	1.3	7.33	1.1	6.18	0.9
10	1	1	170	450	14.08	1.3	7.09	1.3	6.1	1.1
11	1	1	170	450	13.94	1.7	8.72	1.8	6.10	1.6
12	1	1	170	450	7.27	1.9	9.02	1.9	7.22	1.7

reaming process studies. Experiments were carried out using L_{12} orthogonal array and analysed with ANOVA. In the experimental work the effects of reamer's tool life, cutting parameters and the part position in the clamping device on the cylindricity and surface roughness of the piston bore were studied. Experiments were carried out at ambient temperature $T = 23\,°C$ with standard reamer DIN 8094B with diameter of 11.9 mm. Control factors – parameters and their values (Table 1) were determined by pre-experiments for technological window determining and constitute an adequate range of parameters, which allow achieving the required specifications.

Experiments were carried out on Mori Seiki machine tool equipped with the option of tool life monitoring, which allows measurements of tool in-operation time in minutes. The workpiece material was C45E with dimensions of 70 mm × 100 mm × 100 mm. Reamer tool operation time was $t = 250$ min. The goal of using such tool was to get some conclusions that would present a base for further optimization researches that would not include only a new tool.

1.3 Bore Cylindricity and Roughness Measuring

Piston bore cylindricity measurements were carried out using Tayloround measuring device. For each specimen four roundnesses that define cylindricity at different bore positions together were recorded. To characterize surface roughness surface topology parameter *Ra* was used. Measurements were carried out using MarSurf roughness tester. For each specimen four profiles at four different piston bore positions were recorded.

2 EXPERIMENTAL RESULTS

Bore cylindricity and average surface roughness *Ra* resulted during machining of piston bore was measured after the experiments. The experimental results are given in Table 1. The correlation between the control factors and results of piston bore machining were obtained with multiple regressions. A multiple analysis of variance (ANOVA) was used for identifying the factors significantly affecting the preference measures, cylindricity and surface roughness after machining. f

2.1 Measurement Reproducibility

Experiments were carried out using L_{12} orthogonal array and analysed with ANOVA. Bore cylindricity and average surface roughness *Ra* resulted during machining of piston bore was measured after the experiments. The experimental results are given in Table 1. In order to define source of measurements deviation SEM analysis of surface cleanliness was performed. Impact of surface cleanliness was minimized with additional washing and degreasing.

2.1.1 Measurements after CNC Machining

A multiple analysis of variance (ANOVA) was used for identifying the factors significantly affecting the preference measures: cylindricity and surface roughness after machining on CNC centre. At this stage none of the controlled factors was recognized as significant and no regression model could be defined. Due to relative large measurements dispersion

(Table 1) investigation on factors that affect bore quality, and was at very beginning neglected, was repeated. With deeply cause and effect (Fig. 1) investigation surface cleanliness was recognized as the key non-productive operation factor that impacts measurements reproducibility. SEM analysis was chosen as an appropriate method to study the surface cleanliness. During investigation with SEM analysis cleanliness of the bore surface was recognized as inadequate (Fig. 3a). SEM analysis shows presence of relatively big particles on the surface that impact measurement reproducibility. Regarding on these conclusion washing, with industrial washing machine, of all samples was performed.

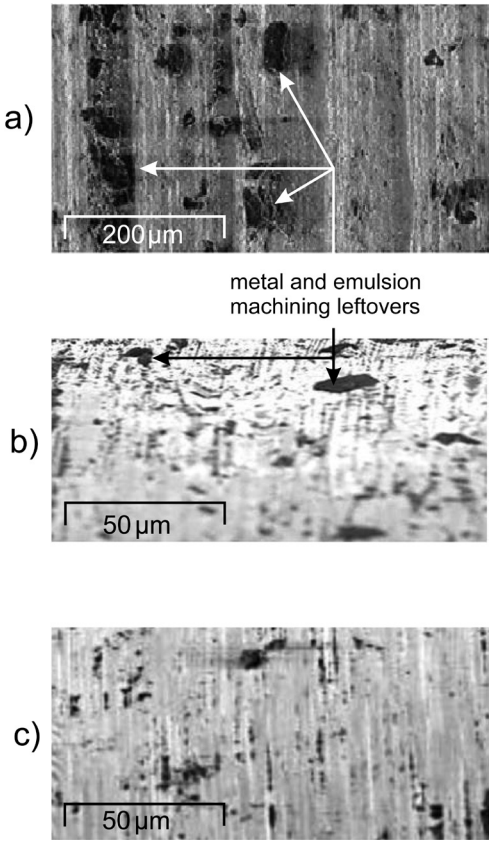

Fig. 3. *Results of bore surface SEM analysis; a) after CNC; b) after washing; c) after degreasing*

2.1.2 Measurements after Washing

After washing of all samples measurements and ANOVA were repeated (Table 1). Measurements after washing significantly differ from measurements after CNC machining (Table 2) which identify cleanliness of bore surface as the main impact on measurement reproducibility. ANOVA of measurements after washing did not recognize any factor as significant as well and consequently none regression model could be defined. SEM analysis of bore surface was repeated in order to confirm if there is still some noise effect on measurements (Fig. 3b). SEM analysis confirmed that there are still some smaller particles and lubricant leftovers that could have a negative impact on measurements reproducibility.

Table 2. Derogations proportion

Exp. No.	Difference [%]			
	After CNC / after washing		After washing / after degreasing	
	Cylindricity	*Ra*	Cylindricity	*Ra*
1	34	19	26	38
2	23	4	40	11
3	29	40	25	47
4	27	32	36	8
5	49	4	6	4
6	39	8	3	20
7	18	12	26	18
8	16	23	34	36
9	25	15	16	18
10	50	4	14	15
11	37	8	20	11
12	19	0	20	13

2.1.3 Measurements after Degreasing

All samples were degreased at this stage and measurements were repeated. Investigation of cleanliness of the bore surface was performed with SEM analysis and results confirm that adequate surface cleanliness was reached (Fig. 3c).

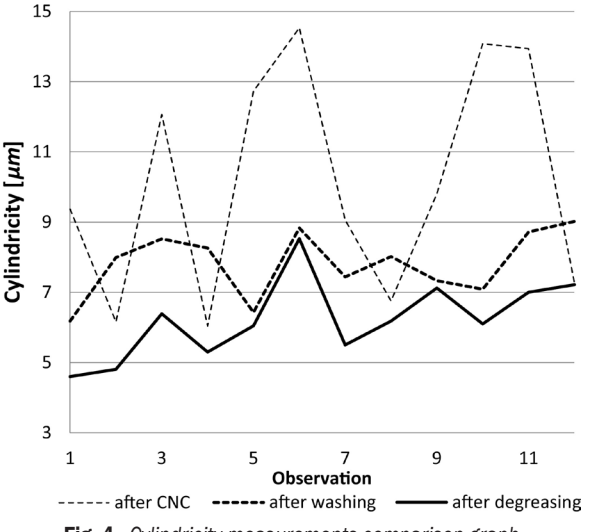

Fig. 4. *Cylindricity measurements comparison graph*

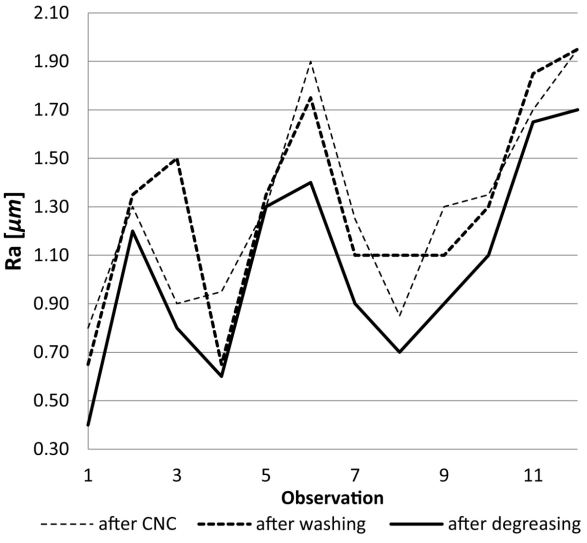

Fig. 5. *Surface roughness measurements comparison graph*

Figs. 4 and 5 show comparison between all measurements, it is obvious that measurements after CNC machining, after washing and after degreasing deviate drastically on the same sample (Table 2). Deviations within bore cylindricity measurements (Table 3) are greater than surface roughness which confirms large effect of surface cleanliness on cylindricity measurements reproducibility. Measurements after degreasing give best results and represent results that are reliable for research. ANOVA of measurements after washing still could not recognize any factor as significant and no regression model could be defined. Before making conclusions on controlled factors significance, additional researches on reliable data are needed.

2.2 Clamping Device Weakness

The existing clamping device allows mounting of three pieces, as shown in Fig. 6. Cylindricity /○/ graph (after degreasing) in Fig. 4 demonstrates the shortcoming of the clamping device. Shortcomings are evident as trend deviations of measurements of three consecutive samples. The results show that only the first nest ensures an adequate rigidity, allows the desired results and ensures reproducibility of the measurement (nest no. 1 in Fig. 6). Nests no. 2 and 3, due to poor rigidity, do not allow adequate reproducibility.

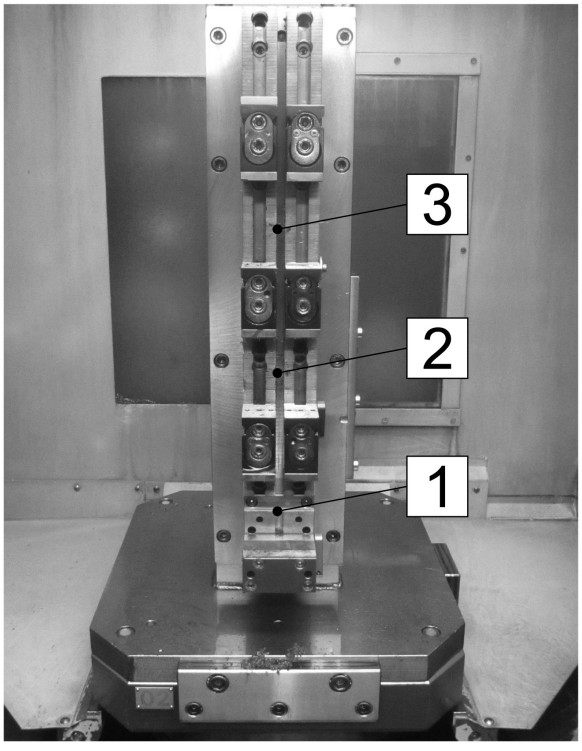

Fig. 6. *Clamping device with three nests*

2.3 Final Results Interpretation

Investigations on measurements reproducibility and clamping device weakness were performed and conclusion is that only measurements of samples that were clamped in nest no. 1 and those whose surface was degreased are adequate for further researches.

One of significant advantages of L_{12} orthogonal array is that it could be interpreted in three blocks of L_4 orthogonal arrays as shown in Table 4. $L_{4\text{-}1}$ represents experiments that include samples that were machined in nest no. 1. ANOVA for $L_{4\text{-}1}$ results (after degreasing) was performed and both controlled

Table 3. *Deviations within measurements*

After CNC		After washing		After degreasing	
Cylindricity (max – min) [μm]	*Ra* (max – min) [μm]	Cylindricity (max – min) [μm]	*Ra* (max – min) [μm]	Cylindricity (max – min) [μm]	*Ra* (max – min) [μm]
8.49	1.15	2.84	1.3	3.928	1.3

factors were recognized as significant in machining bore cylindricity and surface roughness.

Table 4. *L_{12}: block interpretation*

Array	Exp. No.	Array	Exp. No.
L_{12}	1	$L_{4\text{-}1}$	1
	2		4
	3		7
	4		10
	5	$L_{4\text{-}2}$	2
	6		5
	7		8
	8		11
	9	$L_{4\text{-}3}$	3
	10		6
	11		9
	12		12

2.3.1 Regression Model for Cylindricity

The cylindricity formed in reaming piston bore is evaluated in Table 5. Both control factors were recognized as significant. Regression model for cylindricity is defined with Eq. (1):

$$Cylindricity = 5.37 + 0.43 \cdot f + 0.33 \cdot n \,. \qquad (1)$$

Cylindricity regression model shows that cylindricity increases with the increase of feed rate f and spindle speed n. The feed rate has the most dominant effect on machining piston bore cylindricity, while spindle speed influence is lower. The Model F-value of 229 implies the model is significant. There is only a 4.67% chance that value this large could occur due to the noise.

Table 5. *ANOVA for cylindricity regression model*

Source	Sum of Squares	*df*	Mean square	*F*-value	*p*-value Prob > *F*
Model	1.15	2	0.57	229	0.05
A - f	0.72	1	0.72	289	0.04
B - n	0.42	1	0.42	169	0.05
R-Squared	= 0.99				

2.3.2 Regression Model for Surface Roughness

The quality of machined surface generated in reaming piston bore is evaluated in terms of mean surface roughness (*Ra*) values in Table 6. Regression model for surface roughness *Ra* is defined with the Eq. (2):

$$Ra_{average} = 0.75 + 0.25 \cdot f + 0.1 \cdot n \,. \qquad (2)$$

Feed rate has the main role in achieving surface roughness. The model F-value of $6.36 \cdot 10^7$ implies the model is significant. There is only a 0.01 % chance that value this large could occur deue to the noise.

Table 6. *ANOVA for roughness regression model*

Source	Sum of Squares	*df*	Mean square	*F*-value	*p*-value Prob > *F*
Model	0.29	2	0.15	6.36·107	0.05
A - f	0.27	1	0.25	6.36·107	0.04
B - n	0.04	1	0.04	6.36·107	0.05
R-Squared	= 1				

3 DISCUSSION

This paper addresses the study of piston bore machining. Experimental planning and process modeling was performed by DOE methodology. Influence of productive and non-productive operations on product quality was performed in parallel, but they could be treated individually.

Process pre-analyses were performed with cause and effect methodology. It represents the first step in determination of productive and non-productive operations influence on product quality. Conclusions on productive operations influence analysis lead to technological window determination, design of experiments and their execution. Experimental results were given as cylindricity and roughness of machined bore. ANOVA of measurements gave information if results could lead in multi-objective optimization strategy or not.

If ANOVA does not confirm significance of process parameters, additional cause and effect analyses are needed, corrective actions must be taken and ANOVA must be repeated. In this study this step was repeated three times, i.e. the loop of non-productive operations influence, namely washing, degreasing and clamping device were observed.

Results of industrial case study show that this methodology can support clear problem statement and lead to suitable corrective actions.

Conclusions that have been made during investigation are facts that must be obtained in further researches. Precise results of regression models for bore cylindricity and surface roughness are needed; these will lead to optimization strategy of piston bore machining (Fig. 7).

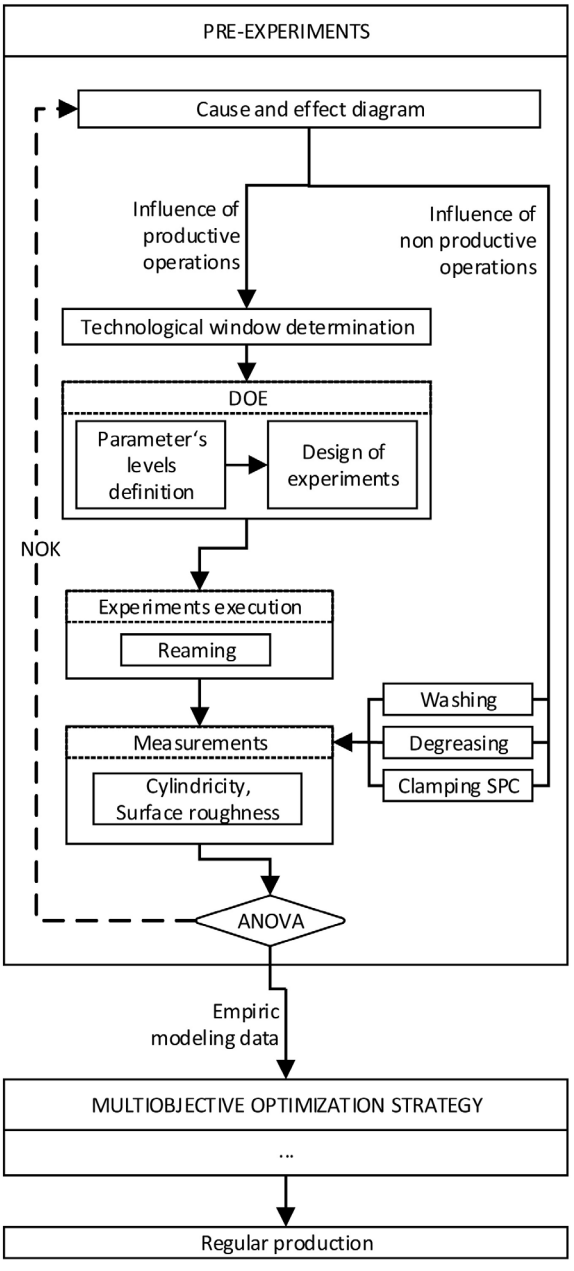

Fig.7. *Optimization strategy model*

4 CONCLUSIONS

Reaming process quality improvement was performed and the following conclusions can be made:

- Surface cleanliness and clamping device rigidity were identified as key non-productive operation factors.
- Surface cleanliness impact was analysed with SEM analysis and was minimized with additional washing and degreasing.
- Surface cleanliness has greater negative effect on bore cylindricity measurements than on surface roughness measurements.
- Clamping device lack of rigidity was minimized with focusing on only one (of three) clamping nest.
- Experimental results of L_{12} orthogonal array were interpreted with three blocks of L_4 orthogonal arrays.
- Regression analyses give models for both productive operations responses (feed rate and spindle speed) under consideration, namely bore cylindricity and surface roughness, and are adequate at 99 % and 100 % confidence level respectively.
- Results show grat feed rate influences on both responses while spindle speed has a smaller effect on bore cylindricity only.

5 REFERENCES

[1] Majdič, F., Pezdirnik, J., Kalin, M. (2011). Experimental validation of the lifetime performance of a proportional 4/3 hydraulic valve operating in water. *Tribology International*, vol. 44, no. 12, p. 2013-2021, **DOI:10.1016/j.triboint.2011.08.020**.

[2] Montgomery, D., C. (2005). *Design and Analysis of Experiments* (6th ed.). John Wiley and Sons, Hoboken.

[3] Wen, X., Zhao, Y., Wang, D., Pan, J. (2013). Advanced Monte Carlo and GUM methods for the evaluation of measurement uncertainty of cylindricity error. *Precision Engineering*, vol. 37, no. 4, p. 856-864, **DOI:10.1016/j.precisioneng.2013.05.002**.

[4] Stepien, K. (2014). In situ measurement of cylindricity - Problems and solutions. *Precision Engineering*, vol. 38, no. 3, p. 697-701. **DOI:10.1016/j.precisioneng.2014.02.007**.

[5] Raykar, S.J., D'Addona, D.M., Kramar, D. (2014). Analysis of surface topology in dry machining of EN-8 steel. *Procedia Materials Science*, vol. 6, p. 931-938, **DOI:10.1016/j.mspro.2014.07.163**.

[6] Müller, P., Genta, G., Barbato, G., De Chiffre, L., Levi, R. (2012). Reaming process improvement and control: An application of statistical engineering. *CIRP Journal of Manufacturing Science and Technology*, vol. 5, no. 3, p. 196-201, **DOI:10.1016/j.cirpj.2012.07.005**.

[7] De Chiffre, L., Tesello, G., Piška, M., Müller, P. (2009). Investigation on capability of the reaming process using minimal quantity lubrication. *CIRP Journal of Manufacturing Science and Technology*, vol. 2, no. 1, p. 47-54, **DOI:10.1016/j.cirpj.2009.08.004**.

[8] Korkut, I., Kucuk, Y. (2010). Experimental analysis of the deviation from circularity of bored hole based on the Taguchi method. *Strojniški vestnik - Journal of Mechanical Engineering*, vol. 6, no. 5, p. 340-346.

[9] Xiao, W., Zi, Y., Chen, B., Li, B., He, Z. (2014). A novel approach to machining condition monitoring of deep hole boring. *International Journal of Machine Tools and Manufacture*, vol. 77, p. 27-33, **DOI:10.1016/j.ijmachtools.2013.10.009**.

[10] Tadic, B., Vukelic, D., Miljanic, D., Bogdanovic, B., Macuzic, I., Budak, I., Todorovic, P. (2014). Model testing of fixture-workpiece interface compliance in dynamic conditions. *Journal of Manufacturing Systems*, vol. 33, no. 1, p. 76-83, **DOI:10.1016/j.jmsy.2013.05.004**.

[11] Jose, V., Nebot, A., Liu, J., Subiron, FR. (2014). Quality prediction and compensation in multi-station machining processes using sensor-based fixtures. *Robotics and Computer-Integrated Manufacturing*, vol. 28, no. 2, p. 208-219, **DOI:10.1016/j.rcim.2011.09.001**.

[12] Theodoris, S., Koutroumbas, K. (1998). *Pattern recognition system*. Academic Press, San Diego.

[13] Hassan, A., Basksh, M.S.N., Shaharoun, A.M., Jamaluddin, H. (2006). Feature selection for SPC chart pattern recognition using fractional factorial experimental design. *Intelligent Production machines and Systems, 2nd I*PROMS Virtual International Conference*, p. 442–447, **DOI:10.1016/B978-008045157-2/50079-1**.

[14] NFE 66-520, (1994). *Couple outil-matiere: Domaine de fonctionnement des outils coupants*, vol. 1-6. Anfor, Pariz.

Vsebina

Strojniški vestnik - Journal of Mechanical Engineering
letnik 62, (2016), številka 3
Ljubljana, marec 2016
ISSN 0039-2480

Izhaja mesečno

Razširjeni povzetki (extended abstracts)

Strojniški vestnik - Journal of Mechanical Engineering 62(2016)3, SI 23
© 2016 Strojniški vestnik. Vse pravice pridržane.
Prejeto v recenzijo: 2015-08-31
Prejeto popravljeno: 2015-11-06
Odobreno za objavo: 2016-01-08

Impulzno-odbojne ultrazvočne preiskave lepljenih spojev steklenih fasad

Bor Mojškerc – Tomaž Kek – Janez Grum*
Univerza v Ljubljani, Fakulteta za strojništvo, Slovenija

Namen raziskav je razviti možen način ocenjevanja kakovosti lepljenih spojev v steklenih fasadah. Izbrana metoda preiskav naj bo neporušna, enostavna za uporabo in cenovno ugodna.

Z razvojem gradbeništva in industrije so se povečale možnosti uporabe steklenih panelov v fasadah različnih stavb. Za zagotavljanje kakovosti lepljenih spojev steklenih panelov je treba le te testirati v proizvodnji in tudi med uporabo, saj lahko slabo lepljeni spoji predstavljajo nevarnost za ljudi in okolico. Lepljene spoje lahko pregledujemo vizualno, vendar nam to običajno ne nudi celovite slike o kakovosti spoja, še posebej pri neprozornih materialih. Za preiskavo te vrste materialov lahko uporabimo ultrazvočne preiskave.

Metodologija raziskav je osnovana na načelih zvočnih in ultrazvočnih valovanj. Vsaka snov ima svojo akustično impedanco. Koeficienta odboja in prehoda ultrazvočnih valov, R in T, sta povezana z akustično impedanco danih materialov, ki tvorita lepljeni spoj. Amplitudna vrednost odbitega valovanja je odvisna od prisotnosti različnih snovi v lepljenem spoju. To namiguje na možnost ocenjevanja kakovosti lepljenih spojev.

Preiskave so izvedene z neporušno impulzno-odbojno ultrazvočno metodo. Kakovost lepljenih spojev v steklenih fasadah je ocenjena s parametri ultrazvočnih preiskav, ki so izbrani na podlagi enofaktorske analize variance (ANOVA). Za oceno kakovosti stika mejne ploskve med steklom in lepilom je uporabljena amplitudna vrednost tretjega odboja, A_3. Za oceno kakovosti stika mejne ploskve med lepilom in polimernim profilom je uporabljena amplitudna vrednost prvega odboja, A_1, saj je edina prisotna v primerih spoja z lepilom, brez lepila ali ob prisotnosti nečistoč.

Rezultati eksperimentov kažejo, da je impulzno-odbojna ultrazvočna metoda uporabna za ocenjevanje lepljenih spojev v steklenih fasadah. Zaznavanje napak je uspešno, saj izrazito zaznamo področja brez lepila in tudi majhne zračne mehurčke na mejni ploskvi lepljenega spoja. Zaznavanje nečistoč na mejni ploskvi med steklom in lepilom je le delno uspešno, saj zaznamo nečistoče, kot sta mast in lepilni trak, zelo tanki nanosi masti pa niso zaznani. Na mejni ploskvi med lepilom in polimerno letvijo zaznamo vse omenjene napake in nečistoče, z večjimi razlikami v amplitudni vrednosti izbranih odbojev.

Najbolj izrazita omejitev te vrste ultrazvočnih preiskav je v vrsti in velikosti izbranega ultrazvočnega pretvornika. Z uporabo normalne ultrazvočne glave s premerom 6 mm lahko naenkrat preiskujemo le omejeno področje celotne širine lepljenega spoja. V kolikor želimo preiskati celoten spoj, bi potrebovali veliko vloženega časa. Možna rešitev je uporaba ultrazvočnih glav z matrično razporeditvijo piezoelektričnih elementov, vendar je cena opreme v tem primeru relativno visoka.

Ocenjevanje kakovosti lepljenih spojev z ultrazvočnimi neporušnimi preiskavami je bilo do sedaj izvedeno večinoma v avtomobilski industriji, z uporabo drugih metod in ocenjevalnih parametrov. Izbrana impulzno-odbojna ultrazvočna metoda testiranja lepljenih spojev nudi enostaven način testiranja z relativno visoko uspešnostjo zaznave napak in nečistoč. Preiskave se lahko izvedejo ročno ali avtomatizirano, v laboratoriju ali na terenu.

Ključne besede: neporušne preiskave, ultrazvočne preiskave, nadzor kakovosti, impulzno-odbojna metoda, akustična impedanca, lepljeni spoji, steklene fasade

*Naslov avtorja za dopisovanje: Univerza v Ljubljani, Fakulteta za strojništvo, Aškerčeva 6, 1000 Ljubljana, Slovenija, janez.grum@fs.uni-lj.si

Strojniški vestnik - Journal of Mechanical Engineering 62(2016)3, SI 24
© 2016 Strojniški vestnik. Vse pravice pridržane.
Prejeto v recenzijo: 2015-05-07
Prejeto popravljeno: 2015-09-16
Odobreno za objavo: 2015-12-01

Eksperimentalna študija kavitacijske in korozijske odpornosti prevlek iz Stellita 6 in samotaljivih pretaljenih prevlek Ni-Cr-B-Si-Mo

Costel-Relu Ciubotariu[1,*] – Evelina Secosan[1] – Gabriela Marginean[2] – Doina Frunzaverde[1] – Viorel Campian[1]

[1] Univerza Eftimie-Murgu v Resiti, Romunija
[2] Vestfalska visoka šola v Gelsenkirchnu, Nemčija

Kakovost vodne energije je odvisna od vzdržljivosti in zanesljivosti hidravličnih strojev. Površinske poškodbe zaradi utrujanja, korozije in obrabe, še posebej pa zaradi kavitacijske erozije, so glavni vzrok odpovedi komponent v hidroelektrarnah.

Kavitaciji pri vodnih turbinah se je le težko popolnoma izogniti, mogoče pa jo je omejiti na ekonomsko sprejemljivo raven s pravilno zasnovo turbinskih komponent ter z uporabo visokokakovostnih nerjavnih jekel ali zaščitnih prevlek. Jamičenje zaradi kavitacije v nekaterih primerih spremljajo tudi korozijske poškodbe. V objavljeni literaturi je mogoče najti poročila o raziskavah vedenja prevlek za zaščito pred kavitacijo v okoljih, ki so obremenjena z zmesjo žveplove kisline ter raznih nečistoč, kot so kloridi, ki delujejo kot oksidanti ali reducenti. Komponente turbin zahtevajo kombinirano zaščito pred kavitacijo in korozijo, zato so avtorji tega članka izvedli eksperimente za karakterizacijo odpornosti analiziranih zaščitnih prevlek proti obema pojavoma.

Znano je, da kobaltove zlitine zagotavljajo odlično zaščito pred obrabo, tudi kavitacijsko, medtem ko samotalilne zlitine zagotavljajo korozijsko odpornost. Članek podaja primerjavo prevlek iz Stellita 6 in NiCrBSiMo glede na njihovo odpornost proti kavitacijski eroziji in koroziji, pri čemer so bile za referenco uporabljene vrednosti, ki so jih avtorji pridobili za mehko martenzitno nerjavno jeklo tipa 13-4. To jeklo se namreč pogosto uporablja kot osnovni material pri izdelavi komponent vodnih turbin.

Da bi bili rezultati kar se da realistični, sta bili dve vrsti zaščitnih slojev naneseni na podlago iz martenzitnega nerjavnega jekla s postopkom toplotnega nabrizgavanja. Po nanosu je bila za izboljšanje lastnosti slojev in metalurške vezave na podlago prevleka iz Stellita 6 lasersko pretaljena, prevleka NiCrBSiMo pa je bila plamensko obdelana.

Odpornost obeh materialov proti kavitacijski eroziji je bila ovrednotena z merjenjem srednje globine erozije, nastale v 165 minutah preizkusa z 20 kHz ultrazvočnim vibratorjem pri amplitudi od vrha do vrha 50 μm. Korozijska odpornost slojev je bila ocenjena s potenciodinamičnimi korozijskimi preizkusi v raztopini H_2SO_4 + NaCl pri sobni temperaturi. Za referenčno elektrodo je bil uporabljen kalomel. Da bi poudarili razlike v vedenju obeh zaščitnih materialov, so avtorji opravili tudi preiskavo mikrostrukture slojev pred in po izpostavitvi kavitaciji in koroziji s pomočjo vrstične elektronske mikroskopije, analize EDX in rentgenske difrakcije.

Preiskava je razkrila, da obe vrsti zaščitnih prevlek (Stellite 6 in NiCrBSiMo) zagotavljata občutno povečanje odpornosti proti kavitacijski eroziji in koroziji v primerjavi z mehko podlago iz martenzitnega nerjavnega jekla. Zlitina na osnovi kobalta je bila bolj odporna proti kavitacijski eroziji med preizkusom z neposredno ultrazvočno metodo. Čeprav je bila korozijska odpornost te zlitine boljša kot pri martenzitnem substratu, pa jo je treba jemati z rezervo zaradi nezaželenega pojava jamičenja, ki ga je razkrila preiskava korodirane površine z vrstičnim elektronskim mikroskopom. Prevleka NiCrBSiMo ima v primerjavi z martenzitnim substratom odlično odpornost proti koroziji (še posebej zaradi korozijskega mehanizma, ki je povzročil enakomerno korozijo površine), kakor tudi izboljšano odpornost proti kavitaciji.

Avtorji na podlagi opisanih rezultatov sklepajo, da lahko obe vrsti slojev zagotavljata izboljšano zaščito substrata iz martenzitnega nerjavnega jekla pred kavitacijo, prevleka NiCrBSiMo pa poleg tega še občutno povečuje korozijsko odpornost.

Ključne besede: hidravlični stroji, kavitacijska odpornost, korozijska odpornost, samotaljive zlitine, Stellite 6, toplotno nabrizgavanje, lasersko pretaljevanje, plamenska obdelava

*Naslov avtorja za dopisovanje: Univerza Eftimie-Murgu v Resiti, Traian Vuia Square, no. 1-4, Resita, Romunija, r.ciubotariu@uem.ro

Strojniški vestnik - Journal of Mechanical Engineering 62(2016)3, SI 25
© 2016 Strojniški vestnik. Vse pravice pridržane.
Prejeto v recenzijo: 2015-07-31
Prejeto popravljeno: 2015-11-03
Odobreno za objavo: 2016-01-07

Načrtovanje nelinearnega regulatorja pozicije elektrohidravličnega servo sistema na osnovi Lyapunove teorije stabilnosti

Edvard Detiček* -– Mitja Kastrevc
Univerza v Mariboru, Fakulteta za strojništvo, Slovenija

Elektro-hidravlični servo-sistemi zavzemajo pomembno mesto na področju sodobne strojegradnje. Področja uporabe so proizvodne montažne linije, roboti, letalstvo, naprave za preskušanje materialov in konstrukcij itd. Na omenjenih področjih je še posebej izražena zahteva po natančnem vodenju pomika batnice hidravličnega valja. Slednje zagotovimo z natančno izdelavo hidravličnega valja, ob primerni izbiri tesnil na batu. Pomembna je tudi uporaba visoko dinamičnih servo- ventilov in kvalitetnih merilnikov pomika.

Ena najpomembnejših nalog pri tem je zasnova zaprto-zančnega avtomatičnega vodenja oziroma regulacije ter izbira regulacijskega predpisa. V prispevku je osrednja pozornost namenjena ravno izbiri primernega regulacijskega predpisa. Pri tem je upoštevana močno nelinearna dinamika servo-hidravličnega pogona. Postopek temelji na načelu povratno-zančne linearizacije sistema, ki skuša z ustreznim regulacijskim predpisom kompenzirati vse nelinearnosti sistema. Ob tem se izkaže, da nekatere nelinearnosti ugodno vplivajo na dinamično obnašanje sistema, predvsem v smislu povečanja dušenja itd. in jih zato, z regulacijskim predpisom, ni smiselno kompenzirati. Zaradi tega je izbira regulatorja izvedena na osnovi, tako imenovanega, integrator backstepping postopka, ki temelji na stabilnostni teoriji Lyapunova. Sistematično pot za načrtovanje regulatorjev, kjer lahko poljubno izpeljemo regulacijski predpis in ohranimo koristne nelinearnosti je uvedel Krstic s soavtorji v delu »Nonlinear and Adaptive Control Designs« [7]. V pričujočem prispevku je prikazana računalniška simulacija dinamičnega vedenja elektro-hidravličnega servo-sistema, ki temelji na nelinearnem fizikalno matematičnem modelu ter številčnih podatkih realnega pogona v laboratoriju. Na omenjenem matematičnem modelu temelji tudi zasnova nelinearnega regulacijskega predpisa, ki ga predstavljamo v tem prispevku. Podani so tudi rezultati računalniške simulacije dinamičnega obnašanja hidravličnega pogona ob uporabi novega regulacijskega predpisa v primerjavi z obnašanjem običajnega P-regulatorja. Kvaliteta sledenja želeni vrednosti je, v primeru uporabe nelinearnega regulatorja bistveno izboljšana. Pri tem ostaja nerešena možnost prilagajanja regulacijskega predpisa trenutnim spremembam parametrov sistema med delovanjem. Nadaljnje delo je zato usmerjeno v raziskave in razvoj adaptivnega nelinearnega vodenja elektro-hidravličnih servo-sistemov.

Ključne besede: nelinearne regulacije, Lyapunova metoda stabilnosti, integrator backstepping, pozicijska regulacija, elektro-hidravlični servo sistemi, računalniška simulacija

*Naslov avtorja za dopisovanje: Univerza v Mariboru, Fakulteta za strojništvo, Slovenija, Smetanova 17, 2000 Maribor, Slovenija, edvard.deticek@um.si

Strojniški vestnik - Journal of Mechanical Engineering 62(2016)3, SI 26
© 2016 Journal of Mechanical Engineering. All rights reserved.
Prejeto v recenzijo: 2015-07-20
Prejeto popravljeno: 2015-10-22
Odobreno za objavo: 2015-12-17

Analiza vpliva procesnih parametrov na variabilnost debeline sten izdelka pri konvencionalnem vrtilnem preoblikovanju avstenitnega nerjavnega jekla Cr-Mn

Peter Šugár[1] – Jana Šugárová[1] – Ján Petrovič[2]
[1] Slovaška tehniška univerza, Fakulteta za materiale in tehnologijo, Slovaška
[2] Eiben, Co. Ltd., Slovaška

Konvencionalno rotacijsko preoblikovanje je tehnologija, pri kateri se krožna pločevina postopoma preoblikuje na trnu z delovanjem valja, ki lokalizirano pritiska na zunanjo površino pločevino in z aksialnim gibanjem ustvari simetričen izdelek. Gre za prilagodljiv postopek preoblikovanja pločevine, ki predstavlja cenovno ugodno alternativo za izdelavo delov z zelo dobrim razmerjem med trdnostjo in maso.

V praksi velja prepričanje, da je debelina stene preoblikovanih delov pri konvencionalnem rotacijskem preoblikovanju praktično konstantna, v resnici pa je debelina stene porazdeljena neenakomerno. Dosedanje eksperimentalne študije so pokazale, da je spremenljivost debeline stene odvisna predvsem od števila prehodov orodja, zamika med posameznimi prehodi, podajanja orodja, oblike izdelka, polmera valja, trenja in trajektorije prvega prehoda orodja.

Čeprav je bilo s sistematičnimi eksperimentalnimi in teoretičnimi preiskavami pridobljeno znanje o mehaniki rotacijskega preoblikovanja, ki pomaga pri razumevanju lastnosti končnih izdelkov, pa vzroki tanjšanja sten izdelka med konvencionalnim rotacijskim preoblikovanjem še vedno niso popolnoma raziskani. Pozornost je bila posvečena predvsem izdelkom iz ogljikovih jekel in aluminijevih zlitin, zato obstaja vrzel med rezultati akademskih raziskav in potrebami industrije na področju konvencionalnega vrtilnega preoblikovanja težko obdelovalnih materialov.

V predstavljeni študiji je bila analizirana variabilnost debeline stene preoblikovanega izdelka (valjast lonček s premerom zaokrožitve 0,2 mm oziroma oblika, ki bi jo bilo težko doseči na tradicionalnih stiskalnicah) iz avstenitnega nerjavnega jekla Cr-Mn. Za eksperimentalno meritev geometrijske natančnosti je bila uporabljena brezkontaktna metoda zajema podatkov. Debelina je bila merjena na sedmih mestih med dnom in odprto stranjo izdelka, in sicer v treh smereh, povezanih s smermi valjanja pločevine: 0°, 45° in 90°. Razlike v debelini stene izdelka v različnih smereh valjanja pločevine so zanemarljive, zato so bile za končno ovrednotenje uporabljene srednje vrednosti debeline, merjene v treh smereh. Vzorci so bili digitalizirani s 3D-optičnim sistemom GOM ATOS II TripleScan SO MV 320 pod nadzorom programske opreme GOM ATOS Professional v7.4. Vpliv hitrosti trna, podajanja in profila orodne poti (konveksen, konkaven oz. linearen) na variabilnost debeline stene je bil preučen s trinivojsko faktorsko zasnovo eksperimenta. Za kvantifikacijo vplivov vhodnih dejavnikov in njihovih interakcij na variabilnost debeline stene je bila opravljena analiza variance (ANOVA) s programsko opremo Minitab v17.

Rezultati kažejo, da se maksimalna variabilnost debeline stene pojavi približno na polovici višine stene izdelka (območje tanjšanja) in na odprtem koncu izdelka (območje debeljenja).

Med vsemi preučenimi procesnimi parametri je bil statistično najbolj signifikanten profil orodne poti, ki mora biti zato natančno krmiljen. Konkaven profil orodne poti povzroči signifikantno zmanjšanje debeline stene v območju tanjšanja in minimalno zadebelitev stene na odprtem koncu izdelka, ki ju spremlja povečana višina dela. Pri konkavni poti valja so bistveno večje natezne radialne napetosti, ki so tudi glavni razlog za intenzivno tanjšanje stene.

Rezultati eksperimenta potrjujejo minimalno variabilnost debeline stene pri uporabi velikega podajanja ter minimalen vpliv hitrosti trna na variabilnost debeline stene v obeh območjih stene dela.

Za najmanjšo variabilnost debeline stene rotacijsko preoblikovanih delov je priporočljiva uporaba konveksne poti orodja v kombinaciji z večjimi vrednostmi podajanja.

Ključne besede: rotacijsko preoblikovanje kovine, nerjavno jeklo, 3D-optično skeniranje, debelina stene, ANOVA

*Naslov avtorja za dopisovanje: Slovaška tehniška univerza, Fakulteta za materiale in tehnologijo, Jana Bottu 25, 917 24 Trnava, Slovaška, peter.sugar@stuba.sk

Strojniški vestnik - Journal of Mechanical Engineering 62(2016)3, SI 27
© 2016 Strojniški vestnik. Vse pravice pridržane.
Prejeto v recenzijo: 2015-09-03
Prejeto popravljeno: 2016-01-11
Odobreno za objavo: 2016-01-21

Nastanek primarne plasti mineralne volne v usedalni komori

Benjamin Bizjan* – Marko Peternelj – Branko Širok
Univerza v Ljubljani, Fakulteta za strojništvo, Slovenija

V proizvodnem procesu mineralne (steklene, kamene) volne je faza tvorbe primarne plasti vlaken izrednega pomena za lastnosti in kakovost končnih proizvodov. Preučevani pojav zajema pnevmatski transport vlaken od koles centrifuge, kjer se je mineralna talina razvlaknila, do rešetke usedalne komore, kjer se kosmi vlaken združujejo v primarno plast mineralne volne. Pojav je zelo kompleksen, saj gre za dvofazni tok zrak-vlakna, za katerega so značilne zapletene prostorske strukture medsebojno prepletenih vlaken, ki so v interakciji s turbulentnim tokom odpiha. Zaradi kompleksnosti procesa in težavnih pogojev za opazovanje je ravno tvorba primarne plasti najslabše raziskan sklop v proizvodni verigi mineralne volne.

Naš namen je bila študija mehanizma tvorbe primarne plasti na modelni centrifugi, s katero bi lahko obratovalne parametre naprave spreminjali lažje in v širšem obsegu kot v industrijskem okolju. Poleg tega smo želeli tudi izboljšati vizualizacijsko merilno metodo za določanje lastnosti primarne plasti. Večina dosedanjih študij je neposredno z optično intenziteto slike okarakterizirala lastnosti primarne plasti. Našo eksperimentalno postajo pa smo zasnovali na način, da je bilo iz posnetih slik mogoče določiti površinsko in volumetrično gostoto plasti. Ti dve veličini sta fizikalno bolj pomenljivi kot sama optična intenziteta slik, kar omogoča lažjo primerjavo rezultatov z realnim industrijskim procesom.

Eksperimentalno študijo smo izvedli na centrifugi z votlim perforiranim rotorjem, v katerem se je s pomočjo grelnika talil kristalni sladkor – saharoza in tvoril množico vlaken, ki jih je koaksialni tok odpiha odnašal v navpično cev. Na vrhu cevi je bil nameščen aksialni ventilator odsesa, ki je v cevi ustvarjal podtlak, pred ventilatorjem pa je bila mreža krožne oblike, na kateri se je nabirala primarna plast vlaken. Po vsakem eksperimentu smo plast od zgoraj presvetlili z difuzno svetlobo, z nasprotne strani pa posneli fotografijo plasti. Na podlagi ugotovljene stopnje absorpcije svetlobe pred in po nastanku plasti smo izračunali polje debeline plasti in nato polje površinske gostote plasti z enoto [kg/m^2]. Kot integralni procesni veličini smo izračunali normirano standardno deviacijo optične intenzitete, in na podlagi tehtanja vzorcev primarne plasti, še volumetrično gostoto z enoto [kg/m^3]. Skupno je bilo izvedenih 26 eksperimentov pri različnih naborih obratovalnih parametrov: vrtilne hitrosti rotorja centrifuge in ventilatorja odsesa, tlaka na koaksialnih šobah odpiha in časa nabiranja vlaken na mreži.

Rezultati kažejo na značilen vpliv vseh spreminjanih obratovalnih parametrov. Na volumetrično gostoto primarne plasti v največji meri vpliva čas oziroma masa nabranih vlaken, saj večja masa vlaken pomeni večji pretočni upor na mreži, kar povzroči stiskanje plasti. Po drugi strani pa večja masa vlaken privede do prostorsko bolj enakomerne strukture, ki se odraža z nižjo normirano standardno deviacijo optične intenzitete. Tako slednja kot tudi povprečna gostota plasti se znatno znižata tudi pri zvišanju vrtilne hitrosti rotorja, ker se zaradi povečanja centrifugalne sile vlakna razporedijo po večjem območju na mreži, to pa je za lastnosti primarne plasti ugodno. Glede toka odpiha in odsesa pa lahko trdimo, da oba povzročita povečanje gostote primarne plasti, medtem ko je vpliv na enakomernost razporeditve le-te bolj zapleten. Za dosego optimalne kakovosti primarne plasti morata biti prisotni obe tokovni komponenti, a v pravilnem razmerju. Obe komponenti izboljšujeta centričnost in radialno simetričnost primarne plasti, vendar pri prekomernem toku odsesa prihaja do pretirane zbitosti (povečanja gostote) plasti, pri prevelikih pretokih in tlakih odpiha pa do zmanjševanja dolžine vlaken zaradi trganja, kar neugodno vpliva na lastnosti končnih izdelkov. Verodostojnost rezultatov potrjujejo regresijski modeli z relativno visokim koeficientom determinacije (R^2).

Predstavljena študija pomeni precejšen napredek glede na dosedanje raziskave na tem področju, saj uporabljena vizualizacijska metoda omogoča boljšo karakterizacijo mehanizma tvorbe primarne plasti. Možnosti nadaljnjih raziskav v začrtani smeri vidimo predvsem v približevanju modela industrijskim pogojem, torej v uporabi pomičnega usedalnega traku namesto fiksne mreže in pa vpeljavi tangencialne komponente odpiha, ki bo omogočila bolj fino regulacijo procesa.

Ključne besede: mineralna volna, vlakna, primarna plast, centrifuga, zbiralna komora, pnevmatski transport

*Naslov avtorja za dopisovanje: Univerza v Ljubljani, Fakulteta za strojništvo, Aškerčeva 6, 1000 Ljubljana, Slovenija, benjamin.bizjan@fs.uni-lj.si

Strojniški vestnik - Journal of Mechanical Engineering 62(2016)3, SI 28
© 2016 2016 Strojniški vestnik. Vse pravice pridržane.
Prejeto v recenzijo:2015-08-21
Prejeto popravljeno:2016-01-18
Odobreno za objavo:2016-01-25

Nelinearen odziv konzolnih nosilcev zaradi velikih geometrijskih deformacij: Eksperimentalna validacija

Claudia Aide Gonzalez-Cruz* – Juan Carlos Jauregui-Correa – Gilberto Herrera-Ruíz
Avtonomna univerza Querétaro, Fakulteta za strojništvo, Mehika

Mnogi konstrukcijski elementi, kot so lopatice plinskih in vetrnih turbin ter odskočne deske, so oblikovani kot vitki elementi. Ker je takšne elemente pri preučevanju njihovega dinamičnega vedenja mogoče modelirati kot konzolne nosilce, je pomembno razumevanje njihovega nelinearnega vedenja zaradi velikih deformacij. Članek predstavlja eksperimentalno validacijo poenostavljenega modela konzolnega nosilca. Nelinearno vedenje konzolnih nosilcev je predmet raziskav že vrsto let in mnogi raziskovalci so predlagali svoje dinamične modele in eksperimentalne postopke. Kljub temu pa ostajajo nekatera odprta vprašanja in validacija še ni bila opravljena. Namen članka je numerična in eksperimentalna demonstracija dejstva, da je nelinearno vedenje konzolnega nosilca posledica velikih deformacij.

Domneva je bila validirana s poenostavljenim modelom, ki je bil oblikovan na podlagi velikih geometrijskih deformacij in Galerkinovega pristopa. Pri modeliranju so bile privzete homogene, ortotropne in linearne lastnosti materiala. Dinamični model je bil izpeljan z Lagrangeovo enačbo. V končnih enačbah so vključeni tudi polinomski členi, povezani z vračalno silo. Vračalna sila je bila modelirana kot polinom petega reda.

Za validacijo poenostavljenega modela so bili opravljeni eksperimentalni preizkusi na vitkem konzolnem nosilcu. Izmerjene so bile vertikalne vibracije in pospešek na prostem koncu nosilca. Numerični in eksperimentalni podatki so bili analizirani s pomočjo frekvenčnega spektra, zvezne valčne transformacije in faznega diagrama ali fazne ravnine. S kombinacijo teh analiz je bilo mogoče določiti nelinearno vedenje.

Numerični in eksperimentalni rezultati so bili pridobljeni za dvojne obremenitvene razmere: s prostimi in z vsiljenimi vibracijami.

Prikazana je občutljivost modela za začetni pogoj majhnega odmika. Rezultati kažejo linearno in stabilno vedenje, saj amplituda vsake frekvence ostaja konstantna. Model je bil nato rešen z začetnim pogojem velikega odmika. V rezultatih so razvidni stranski pasovi frekvenčnega spektra in očitno nelinearno vedenje, saj se je amplituda frekvenc spreminjala v času (na časovno-frekvenčnem diagramu), v faznem diagramu pa so vidne zaprte zanke z dvema privlačnima poloma. Model je bil pozneje rešen tudi za primer vsiljenih vibracij. Nastavljeno je bilo vzbujanje z dominantnimi frekvencami, ki so bile ugotovljeno eksperimentalno (2,9 Hz, 1,8 Hz in 51 Hz). Sistem je v vseh primerih izkazoval nelinearno vedenje, saj je v časovno-frekvenčnih diagramih mogoče opaziti spremenljivost frekvenc, v faznih diagramih pa se kaže nestabilno vedenje.

Iz rezultatov meritev odziva na proste vibracije sledi, da pri dinamičnem odzivu dominira strukturno dušenje. Ta parameter zmanjšuje amplitudo vibracij in v prvih nekaj vzorcih je bil opažen nelinearen vpliv. Nelinearno vedenje je bilo bolj opazno med preizkusom s prehodom skozi frekvenčno območje. Rezultati kažejo skok zaradi nelinearnosti nosilca pri frekvencah 18,1 Hz in 51 Hz. Končno sta bila izvedena dva preizkusa vibracij pri kritičnih frekvencah.

Pomembno je poudariti, da je nelinearno vedenje nosilca posledica velikih deformacij. Do takšnega vedenja pride pri določeni frekvenci, ki se razlikuje od frekvenc, povezanih z linearnimi zvrstmi. Numerična rešitev kaže značilen vzorec harmoničnih popačenj zaradi polinomskih členov v modelu, ko je vzbujalna frekvenca pod lastno frekvenco, pa sta v faznem diagramu dva privlačna pola. Eksperimentalni rezultati kažejo dve konkretni frekvenci, ki sta povezani z nelinearnimi členi. Nosilec je imel v preizkusu prehoda skozi frekvenčno območje različne amplitude pri frekvenci 51 Hz. Amplituda med dviganjem frekvence je večja od amplitude med nižanjem frekvence in nelinearno vedenje je zato opaznejše pri tej frekvenci. Nelinearno vedenje zaradi velikih deformacij se pojavlja samo pri določenih frekvencah ali ko je nosilec bolj odklonjen. Če nosilec ni vzbujan prav v teh pogojih, je torej vpliv velikih deformacij mogoče zanemariti. Poenostavljeni model, ki je predstavljen v članku, opredeljuje nelinearne frekvence z zadostno točnostjo. Z drugimi metodami pa je te frekvence mogoče določiti le če so relativni odmiki razmeroma veliki.

Ključne besede: fazni diagram, harmonično popačenje, zvezna valčna transformacija, velike geometrijske deformacije, nelinearna dinamika, strukturno dušenje

*Corr. Author's Address: Avtonomna univerza Querétaro, Fakulteta za strojništvo, Cerro de las Campanas s/n, Ciudad Universitaria, Querétaro, Qro. 76010, Mehika, cgonzalez@uaq.mx

Strojniški vestnik - Journal of Mechanical Engineering 62(2016)3, SI 29
© 2016 Strojniški vestnik. Vse pravice pridržane.
Prejeto v recenzijo: 2015-10-11
Prejeto popravljeno: 2015-11-25
Odobreno za objavo: 2015-12-01

Vpliv neproduktivnih operacij na kakovost produkta

Peter Eniko[1] – Mirko Soković[2] – Davorin Kramar[2]
[1] Difa d.o.o., Slovenija
[2] Univerza v Ljubljani, Fakulteta za strojništvo, Slovenija

Prispevek obravnava raziskavo tehnologije izdelave batne izvrtine. V okviru raziskovalnega dela so bili raziskani posamezni in kombinirani učinki procesnih parametrov in vplivi na ponovljivost meritev glede na doseženo geometrijo in površinsko hrapavost batne izvrtine. Eksperimentalni del se je izvajal v redni proizvodnji in je bil podvržen neproduktivnim operacijam, ki vplivajo na doseženo kakovost produkta.

Metoda, ki je bila uporabljena za prepoznavanje in vrednotenje vzrokov in posledic vplivnih faktorjev na kakovost produkta, je metoda določanja diagrama vzrokov in posledic oziroma Ishikawa. Določanje tehnoloških oken je temeljilo na standardu Anfor. Z namenom robustnega dizajniranja procesa je bila za načrt izvajanja eksperimentov uporabljena metoda DOE (Design Of Experiments). DOE vključuje Taguchijevo metodo načrtovanja eksperimentov z uporabo ortogonalnih nizov. Meritve doseženih rezultatov so se izvajale po definirani merilni metodi z merilnikom cilindričnosti, merilnikom hrapavosti ter z elektronskim mikroskopom, SEM (Scanning Electron Microscope). Za analizo rezultatov je bila uporabljena analiza variance, ANOVA (Analysis of Variance).

Na podlagi pregleda literature in predhodnih izkušenj na področju procesa povrtavanja sta bila podajanje (*f*) povrtala in število vrtljajev vretena na minuto (*n*) prepoznana kot ključna faktorja produktivnih operacij pri doseganju predpisanih konstrukterskih specifikacij cilindričnosti in hrapavosti površine batne izvrtine. Neproduktivne operacije, kot so vpliv prisotnosti nečistoč na površini batne izvrtine in vpliv pomanjkljivosti vpenjalne naprave ter vpenjal, so bile med raziskavo ugotovljene s SEM analizo in s prepoznavanjem vzorcev v SPC kontrolnih kartah. Negativni vplivi neproduktivnih operacij so bili minimalizirani s korekturnimi ukrepi. Regresijska analiza poda modele kontrolnih faktorjev. Rezultati obravnavane raziskave (rezultati analiz in korektivnih ukrepov) predstavljajo vhodne podatke empiričnega modeliranja večkriterijske strategije optimiranja znotraj modela za optimiranje tehnologije izdelave.

V sklopu raziskave lahko podamo ugotovitve:

- Čistoča površine, pomanjkljivost vpenjalne naprave in pomanjkljivost vpenjal so bili ugotovljeni kot ključni faktorji neproduktivnih operacij.
- Vpliv čistoče površine je bil analiziran s SEM analizo in je bil minimaliziran z dodatnim pranjem in razmaščevanjem vzorcev.
- Prisotnost nečistoč na površini batne izvrtine ima večji negativni vpliv na meritve cilindričnosti kot na meritve hrapavosti.
- Pomanjkljivost vpenjalne naprave je bila minimalizirana s fokusiranjem na eno (od treh) vpenjalnih gnezd.
- Eksperimentalni rezultati L_{12} ortogonalne matrike so bili interpretirani s tremi bloki po L_4 ortogonalnimi matrikami.
- Regresijska analiza poda modele za produktivne operacije podajanja povrtala in število vrtljajev vretena na minuto. Pri tem sta cilindričnost in hrapavost površine batne izvrtine na ustreznem nivoju zaupanja 99 % in 100 %.
- Rezultati prikazujejo velik vpliv podajanja tako na doseženo cilindričnost kot na doseženo hrapavost površine batne izvrtine, med tem ko ima število vrtljajev vretena na minuto manjši vpliv le na doseženo cilindričnost batne izvrtine.

Ključne besede: DOE, cilindričnost, hrapavost površine, pranje, razmaščevanje

*Naslov avtorja za dopisovanje: Difa d.o.o., Kidričeva cesta 91, 4220, Škofja Loka, SLovenija, peter.eniko@difa.si

Na Fakulteti za strojništvo Univerze v Mariboru je obranil svojo doktorsko disertacijo:

● dne *17. februarja 2016* **Aljaž KOVAČIČ** z naslovom: »Računalniško modeliranje poroznih kompozitnih struktur z napredno morfologijo por« (mentor: prof. dr. Zoran Ren);

Strukture z napredno morfologijo por (APM strukture) so kompozitne kovinske pene, sestavljene iz velikega števila majhnih okroglih elementov z celično notranjo zgradbo, ki so spojeni v kompozit s polimernim vezivom. Rezultat takšne zgradbe je širok spekter dosegljivega mehanskega obnašanja v APM strukturah. Za raziskanje njihovega resničnega potenciala potrebujemo učinkovite računske metode, ki omogočajo preprosto variiranje parametrov. Trenutni računalniški modeli žal ne omogočajo učinkovitih simulacij poroznih kompozitnih struktur z napredno morfologijo por, saj temeljijo na kompleksnejših pristopih k diskretizaciji.

V tem delu je predstavljen nov pristop k simulacijam, ki temelji na metodi diskretnih delcev (metodi DPM), v kateri je vsak element APM strukture diskretiziran z enim samim vozliščem. To omogoča učinkovitejše simulacije APM struktur, vendar še zmeraj omogoča preprosto variiranje strukturnih parametrov. DPM metoda je bila razširjena s konstitutivnimi modeli normalnega in tangencialnega kontaktnega obnašanja APM elementov in njihovih povezav, ki so bili oblikovani na osnovi obširne eksperimentalne študije geometrije in mehanskega obnašanja APM struktur. Modeli zato omogočajo simulacije mehanskega obnašanja velikih APM struktur na osnovi modeliranja kontaktnega obnašanja posameznih elementov.

Izvedba novih modelov je bila preverjena na nizu analitično rešljivih primerov, natančnost modelov pa je bila potrjena z zelo dobrim ujemanjem med računskimi in eksperimentalnimi rezultati. Modeli so bili tako potrjeni na širokem nizu primerov, ki so zajemali tudi različne hitrosti deformacije in odsotnost vezi.

Uporabnost novih modelov je bila dokazana v obsežni parametrični študiji, v kateri so bili identificirani vplivni strukturni parametri in lastnosti pri majhnih in velikih hitrostih deformacije. Študija je tudi dokazala možnost prirejanja mehanskega obnašanja s stopnjevanjem lastnosti ter z vpeljavo urejenih, kakor tudi geometrijsko zapletenih sestavov APM elementov. Naslovljena je bila tudi možnost sklopljenih simulacij po metodah diskretnih delcev in končnih elementov.

Novo razviti modeli predstavljajo preboj na področju računalniških raziskav APM struktur ter zagotavljajo enostavnejše in učinkovitejše raziskave APM struktur v prihodnje;

● dne *18. februarja 2016* **Nena VELKOVA** z naslovom: »Uporaba hemiceluloz za funkcionalizacijo površin sintetičnih polimerov« (mentor: prof. dr. Simona Strnad);

Glavni namen doktorske naloge je bil študij uporabe hemiceluloz ksilanov, kot obnovljivih biopolimerov (stranski produkti papirne in prehrambene industrije) za razvoj postopkov in tehnik za izdelavo tankih funkcionalnih slojev na površinah sintetičnih polimerov, kot je npr. polietilentereftalat, ki ga najdemo v najrazličnejših tehničnih in medicinskih aplikacijah. Pri teh aplikacijah so najpogosteje iskani lastnosti sintetičnih površin hidrofilnost in protimikrobnost.

Na področjih, kjer se materiali uporabljajo v stiku s človeškim telesom, je potrebno zadostiti številnim specifičnim zahtevam, od katerih je najpomembnejše fiziološko udobje. Glavni parametri, ki določajo fiziološko udobje so predvsem: prepustnost za vodno paro, hidrofilnost in termična prevodnost. Za medicinske namene je večkrat zelo zaželena odpornost na različne bakterije.

Uporaba sintetičnih polimerov se je v zadnjih desetletjih močno uveljavila predvsem zaradi nizkih cen in dobrih mehanskih lastnosti kot so elastičnost, trdnost, odpornost na drgnjenje. Vendar pa je v glavnem osnovna značilnost teh materialov, da imajo nizko površinsko energijo in visoko inertnost, kar pomeni hidrofobnost in zato slabe fiziološke lastnosti.

V smislu preseganja teh težav se najpogosteje poslužujejo različnih površinskih obdelav, ki ob spreminjanju površinskih lastnosti ohranjajo mehanske lastnosti polimera. Za izboljšanje hidrofilnosti poliestrov se zelo pogosto uporablja alkalna hidroliza ali obdelava s plinsko plazmo, ki ji je bilo v zadnjih desetletjih posvečeno veliko pozornosti. Slabost teh obdelav je predvsem ugašanje učinkov s časom (staranje). Poleg navedenih se za površinsko funkcionalizacijo uporabljajo encimatske obdelave, površinska kopolimerizacija ali adsorpcija polimerov in izdelava tankih slojev.

Nadomeščanje izdelkov, ki temeljijo na petrokemičnih virih s tistimi, ki so izdelani iz obnovljivih materialov je eden od najpomembnejših

inovacijskih in raziskovalnih ciljev zadnjih desetletij. Takšni obnovljivi materiali vključujejo filme, embalažo in celo vrsto drugih materialov, izdelanih iz biopolimerov. Ekonomski potenciali biopolimerov so ogromni, saj je to najpomembnejše področje za razvoj in doseganje vseh komponent obnovljive industrije. Realizacija je v tem trenutku še relativno slaba, saj trenutno le manj kot 1 % vse proizvodnje polimerov temelji na biopolimerih, vendar pa ti, okoljsko neškodljivi polimeri kažejo potencialno visoko rast. Zadnje študije kažejo, da bo globalno povpraševanje po obnovljivih polimerih naraščalo, in sicer od 180 Mio Ton v letu 2007 na 258 Mio Ton v letu 2010, do leta 2020 pa bi naj biopolimeri nadomestili 5 % celotnega povpraševanja po petrokemičnih polimerih. Pomembna pomanjkljivost naštetih obnovljivih polimerov je, da vsi temeljijo na surovinah, katerih pridobivanje zahteva uporabo kmetijskih zemljišč, ki bi lahko sicer bila uporabljena za pridelavo hrane. To dejstvo predstavlja enega glavnih motivov za poglobljene raziskave drugih potencialnih virov, predvsem stranskih produktov industrijskih procesov. Med takšnimi je vsekakor proizvodnja celuloze in papirja kot vir hemiceluloz in lignina.

Information for Authors

All manuscripts must be in English. Pages should be numbered sequentially. The manuscript should be composed in accordance with the Article Template given above. The maximum length of contributions is 10 pages. Longer contributions will only be accepted if authors provide juastification in a cover letter. For full instructions see the Information for Authors section on the journal's website: http://en.sv-jme.eu .

SUBMISSION:

Submission to SV-JME is made with the implicit understanding that neither the manuscript nor the essence of its content has been published previously either in whole or in part and that it is not being considered for publication elsewhere. All the listed authors should have agreed on the content and the corresponding (submitting) author is responsible for having ensured that this agreement has been reached. The acceptance of an article is based entirely on its scientific merit, as judged by peer review. Scientific articles comprising simulations only will not be accepted for publication; simulations must be accompanied by experimental results carried out to confirm or deny the accuracy of the simulation. Every manuscript submitted to the SV-JME undergoes a peer-review process.

The authors are kindly invited to submit the paper through our web site: http://ojs.sv-jme.eu. The Author is able to track the submission through the editorial process - as well as participate in the copyediting and proofreading of submissions accepted for publication - by logging in, and using the username and password provided.

SUBMISSION CONTENT:

The typical submission material consists of:

- A **manuscript** (A PDF file, with title, all authors with affiliations, abstract, keywords, highlights, inserted figures and tables and references),
- Supplementary files:
  - a **manuscript** in a WORD file format
  - a **cover letter** (please see instructions for composing the cover letter)
  - a ZIP file containing **figures** in high resolution in one of the graphical formats (please see instructions for preparing the figure files)
  - possible **appendicies** (optional), cover materials, video materials, etc.

Incomplete or improperly prepared submissions will be rejected with explanatory comments provided. In this case we will kindly ask the authors to carefully read the Information for Authors and to resubmit their manuscripts taking into consideration our comments.

COVER LETTER INSTRUCTIONS:

Please add a **cover letter** stating the following information about the submitted paper:

1. Paper **title**, list of **authors** and their **affiliations**.
2. **Type of paper**: original scientific paper (1.01), review scientific paper (1.02) or short scientific paper (1.03).
3. A **declaration** that neither the manuscript nor the essence of its content has been published in whole or in part previously and that it is not being considered for publication elsewhere.
4. State the **value of the paper** or its practical, theoretical and scientific implications. What is new in the paper with respect to the state-of-the-art in the published papers? Do not repeat the content of your abstract for this purpose.
5. We kindly ask you to suggest at least two **reviewers** for your paper and give us their names, their full affiliation and contact information, and their scientific research interest. The suggested reviewers should have at least two relevant references (with an impact factor) to the scientific field concerned; they should not be from the same country as the authors and should have no close connection with the authors.

FORMAT OF THE MANUSCRIPT:

The manuscript should be composed in accordance with the Article Template. The manuscript should be written in the following format:

- A **Title** that adequately describes the content of the manuscript.
- A list of **Authors** and their **affiliations**.
- An **Abstract** that should not exceed 250 words. The Abstract should state the principal objectives and the scope of the investigation, as well as the methodology employed. It should summarize the results and state the principal conclusions.
- 4 to 6 significant **key words** should follow the abstract to aid indexing.
- 4 to 6 **highlights;** a short collection of bullet points that convey the core findings and provide readers with a quick textual overview of the article. These four to six bullet points should describe the essence of the research (e.g. results or conclusions) and highlight what is distinctive about it.
- An **Introduction** that should provide a review of recent literature and sufficient background information to allow the results of the article to be understood and evaluated.
- A **Methods** section detailing the theoretical or experimental methods used.
- An **Experimental section** that should provide details of the experimental set-up and the methods used to obtain the results.
- A **Results** section that should clearly and concisely present the data, using figures and tables where appropriate.
- A **Discussion** section that should describe the relationships and generalizations shown by the results and discuss the significance of the results, making comparisons with previously published work. (It may be appropriate to combine the Results and Discussion sections into a single section to improve clarity.)
- A **Conclusions** section that should present one or more conclusions drawn from the results and subsequent discussion and should not duplicate the Abstract.
- **Acknowledgement** (optional) of collaboration or preparation assistance may be included. Please note the source of funding for the research.
- **Nomenclature** (optional). Papers with many symbols should have a nomenclature that defines all symbols with units, inserted above the references. If one is used, it must contain all the symbols used in the manuscript and the definitions should not be repeated in the text. In all cases, identify the symbols used if they are not widely recognized in the profession. Define acronyms in the text, not in the nomenclature.
- **References** must be cited consecutively in the text using square brackets [1] and collected together in a reference list at the end of the manuscript.
- **Appendix(-icies)** if any.

SPECIAL NOTES

Units: The SI system of units for nomenclature, symbols and abbreviations should be followed closely. Symbols for physical quantities in the text should be written in italics (e.g. *v*, *T*, *n*, etc.). Symbols for units that consist of letters should be in plain text (e.g. ms^{-1}, K, min, mm, etc.). Please also see: http://physics.nist.gov/cuu/pdf/sp811.pdf .

Abbreviations should be spelt out in full on first appearance followed by the abbreviation in parentheses, e.g. variable time geometry (VTG). The meaning of symbols and units belonging to symbols should be explained in each case or cited in a **nomenclature** section at the end of the manuscript before the References.

Figures (figures, graphs, illustrations digital images, photographs) must be cited in consecutive numerical order in the text and referred to in both the text and the captions as Fig. 1, Fig. 2, etc. Figures should be prepared without borders and on white grounding and should be sent separately in their original formats. If a figure is composed of several parts, please mark each part with a), b), c), etc. and provide an explanation for each part in Figure caption. The caption should be self-explanatory. Letters and numbers should be readable (Arial or Times New Roman, min 6 pt with equal sizes and fonts in all figures). Graphics (submitted as supplementary files) may be exported in resolution good enough for printing (min. 300 dpi) in any common format, e.g. TIFF, BMP or JPG, PDF and should be named Fig1.jpg, Fig2.tif, etc. However, graphs and line drawings should be prepared as vector images, e.g. CDR, AI. Multi-curve graphs should have individual curves marked with a symbol or otherwise provide distinguishing differences using, for example, different thicknesses or dashing.

Tables should carry separate titles and must be numbered in consecutive numerical order in the text and referred to in both the text and the captions as Table 1, Table 2, etc. In addition to the physical quantities, such as *t* (in italics), the units [s] (normal text) should be added in square brackets. Tables should not duplicate data found elsewhere in the manuscript. Tables should be prepared using a table editor and not inserted as a graphic.

REFERENCES:

A reference list must be included using the following information as a guide. Only cited text references are to be included. Each reference is to be referred to in the text by a number enclosed in a square bracket (i.e. [3] or [2] to [4] for more references; do not combine more than 3 references, explain each). No reference to the author is necessary.

References must be numbered and ordered according to where they are first mentioned in the paper, not alphabetically. All references must be complete and accurate. Please add DOI code when available. Examples follow.

Journal Papers:

Surname 1, Initials, Surname 2, Initials (year). Title. Journal, volume, number, pages, DOI code.

[1] Hackenschmidt, R., Alber-Laukant, B., Rieg, F. (2010). Simulating nonlinear materials under centrifugal forces by using intelligent cross-linked simulations. *Strojniški vestnik - Journal of Mechanical Engineering,* vol. 57, no. 7-8, p. 531-538, DOI:10.5545/sv-jme.2011.013.

Journal titles should not be abbreviated. Note that journal title is set in italics.

Books:

Surname 1, Initials, Surname 2, Initials (year). Title. Publisher, place of publication.

[2] Groover, M.P. (2007). *Fundamentals of Modern Manufacturing*. John Wiley & Sons, Hoboken.

Note that the title of the book is italicized.

Chapters in Books:

Surname 1, Initials, Surname 2, Initials (year). Chapter title. Editor(s) of book, book title. Publisher, place of publication, pages.

[3] Carbone, G., Ceccarelli, M. (2005). Legged robotic systems. Kordić, V., Lazinica, A., Merdan, M. (Eds.), Cutting Edge Robotics. Pro literatur Verlag, Mammendorf, p. 553-576.

Proceedings Papers:

Surname 1, Initials, Surname 2, Initials (year). Paper title. Proceedings title, pages.

[4] Štefanić, N., Martinčević-Mikić, S., Tošanović, N. (2009). Applied lean system in process industry. *MOTSP Conference Proceedings*, p. 422-427.

Standards:

Standard-Code (year). Title. Organisation. Place.

[5] ISO/DIS 16000-6.2:2002. *Indoor Air – Part 6: Determination of Volatile Organic Compounds in Indoor and Chamber Air by Active Sampling on TENAX TA Sorbent, Thermal Desorption and Gas Chromatography using MSD/FID.* International Organization for Standardization. Geneva.

WWW pages:

Surname, Initials or Company name. Title, from http://address, date of access.

[6] Rockwell Automation. Arena, from *http://www.arenasimulation.com,* accessed on 2009-09-07.

EXTENDED ABSTRACT:

When the paper is accepted for publishing, the authors will be requested to send an **extended abstract** (approx. one A4 page or 3500 to 4000 characters). The instruction for composing the extended abstract are published on-line: http://www.sv-jme.eu/information-for-authors/ .

COPYRIGHT:

Authors submitting a manuscript do so on the understanding that the work has not been published before, is not being considered for publication elsewhere and has been read and approved by all authors. The submission of the manuscript by the authors means that the authors automatically agree to transfer copyright to SV-JME when the manuscript is accepted for publication. All accepted manuscripts must be accompanied by a Copyright Transfer Agreement, which should be sent to the editor. The work should be original work by the authors and not be published elsewhere in any language without the written consent of the publisher. The proof will be sent to the author showing the final layout of the article. Proof correction must be minimal and executed quickly. Thus it is essential that manuscripts are accurate when submitted. Authors can track the status of their accepted articles on http://en.sv-jme.eu/.

PUBLICATION FEE:

Authors will be asked to pay a publication fee for each article prior to the article appearing in the journal. However, this fee only needs to be paid after the article has been accepted for publishing. The fee is 240.00 EUR (for articles with maximum of 6 pages), 300.00 EUR (for articles with maximum of 10 pages), plus 30.00 EUR for each additional page. The additional cost for a color page is 90.00 EUR. These fees do not include tax.

Strojniški vestnik -Journal of Mechanical Engineering
Aškerčeva 6, 1000 Ljubljana, Slovenia,
e-mail: info@sv-jme.eu

9 770039 248001
ISSN 0039-2480

http://www.sv-jme.eu

Contents

Papers